International Journal of Plasticity 202 (2026) 104711

Contents lists available at ScienceDirect

International Journal of Plasticity

journal homepage: www.elsevier.com/locate/ijplas

Prospect of quantum computing on Enhanced Strain Gradient Crystal Plasticity theory

Amirhossein Lame Jouybari *, Leon Cizelj

Jožef Stefan Institute, Jamova cesta 39, Ljubljana, Sl-1000, Slovenia
University of Ljubljana, Jadranska ulica 19, Ljubljana, Sl-1000, Slovenia

ARTICLE INFO

Keywords:
Quantum computing
Quantum Fourier transform method
Polycrystalline material
Strain localization
Shear band
Mean-grain size effect

ABSTRACT

A new branch of the Enhanced Strain Gradient Crystal Plasticity (ESGCP) theory is introduced, based on a quadratic energetic contribution associated with the gradient of the cumulative shear strain on each slip system, within a thermodynamically consistent framework for the formation of slip and kink bands in crystalline microstructures. Together with the recently proposed Nye-tensor-based ESGCP formulation, a new differential operator is developed for the solution of the corresponding nonlocal field equation (or higher-order balance equation). In both branches of the ESGCP theory, the higher-order modulus is intrinsically coupled to the evolving microstructural state of irradiated crystalline lattices during deformation. The ESGCP framework is employed to investigate the *Hall–Petch* (mean grain size) effect and is systematically compared with classical Strain Gradient Crystal Plasticity (CSGCP) models. The results reveal that, in contrast to CSGCP formulations where the grain-size effect continuously intensifies by the loading, the ESGCP models predict an enhanced grain-size sensitivity at low strain levels followed by a progressive attenuation at higher levels of loading.

In addition, a novel quantum computing algorithm based on the quantum Fourier transform (QFT) is developed to solve the classical linear momentum balance equation within a fixed-point iteration scheme, while nonlocal field equations associated with the ESGCP and CSGCP models are addressed using a quantum finite difference approach. It is demonstrated that the proposed QFT-method achieves a poly-logarithmic computational speedup, offering significant advantages for high-resolution simulations of irradiated materials, where both numerical accuracy and computational efficiency are critical for reliable structural integrity assessments in nuclear power plant applications.

1. Introduction

Quantum computing. Contemporary computational science is undergoing a disruptive transformation driven by the rapid development of quantum computing and its emerging integration with high-performance and supercomputing architectures. Quantum computing constitutes a fundamentally new computational paradigm based on non-classical representations of information and data processing, enabling access to exponentially large solution spaces and the extraction of information from highly complex datasets through inherently parallel quantum operations. By exploiting quantum mechanical principles such as superposition, entanglement, and interference, quantum algorithms can achieve substantial improvements in computational efficiency for specific classes of problems. In classical computing, algorithmic acceleration is typically achieved through increased hardware resources and

* Corresponding author.Corresponding author at: Jožef Stefan Institute, Jamova cesta 39, Ljubljana, Sl-1000, Slovenia.
E-mail address: Amirhossein.Lame@ijs.si (A. Lame Jouybari).

https://doi.org/10.1016/j.ijplas.2026.104711
Received 28 January 2026; Received in revised form 2 April 2026
Available online 29 April 2026

parallelization strategies; however, for many problems, a linear growth in input size leads to exponential increases in computational time and memory requirements. In contrast, quantum algorithms can, for certain problem classes, achieve polynomial scaling where classical algorithms exhibit exponential complexity. Classical computation relies on the manipulation of classical bits, which can exist only in one of two discrete states, denoted as 0 or 1, at any given time. Operations on classical bits deterministically update these states through logical transformations. Quantum computing, by contrast, is based on the quantum bit, or in abbreviation *qubit*, which constitutes the fundamental unit of quantum information. Unlike classical bits, qubits can exist in a superposition of basis states, represented as a linear combination of the orthonormal vectors $|0\rangle$ and $|1\rangle$ in the *Hilbert* space $\mathbb{H}^2$. Upon measurement, the quantum state irreversibly collapses to one of these basis states according to the *Born* rule, introducing probabilistic outcomes that are intrinsic to quantum computation. The motivation for quantum computing dates back to the early 1980s, when *Richard Feynman* (Feynman, 1982) and *Yuri Manin* (Manin, 1980) independently recognized that classical computers are fundamentally inefficient at simulating quantum systems, particularly as the number of interacting particles increases beyond a few. Since then, sustained theoretical and experimental progress has led to the development of several landmark quantum algorithms that demonstrate provable advantages over their classical counterparts. Notable algorithms include Grover's search algorithm (Grover, 1997), Shor's integer factorization algorithm (Shor, 1997), the Harrow–Hassidim–Lloyd (HHL) algorithm for solving systems of linear equations (Harrow et al., 2009), the variational quantum eigensolver (VQE) (McClean et al., 2016), and quantum algorithms for Hamiltonian simulation (Low and Chuang, 2019). Grover's search algorithm enables the retrieval of a target element from an unstructured database of size N using $\mathcal{O}(\sqrt{\mathrm{N}})$ operations via amplitude amplification, whereas an optimal classical algorithm requires $\mathcal{O}(\mathrm{N})$ operations. Consequently, Grover's algorithm provides a quadratic speedup over classical search methods. Shor's algorithm factors an integer N represented with n bits in $\mathcal{O}(n^3 \log \mathrm{n})$ time using $\mathcal{O}(n^2 \log \mathrm{n} \log\log \mathrm{n})$ quantum gates, while the most efficient known classical algorithms exhibit sub-exponential runtime scaling of $\mathcal{O}(\exp(\sqrt[3]{\frac{64}{9}n(\log n)^2}))$. The HHL algorithm solves a system of linear equations with N variables in $\mathcal{O}(\mathrm{poly}(\log \mathrm{N}, \kappa))$ time, where κ denotes the condition number of the coefficient matrix, representing an exponential improvement over classical algorithms with complexity $\mathcal{O}(\mathrm{N}\sqrt{\kappa})$. The HHL algorithm consists of five principal stages: state preparation, quantum phase estimation, controlled ancilla rotation, inverse quantum phase estimation, and measurement. The variational quantum eigensolver adopts a hybrid quantum–classical computing strategy by iteratively preparing a parameterized quantum state $|\psi(\theta_i)\rangle$, evaluating expectation values of the Hamiltonian on quantum hardware, and updating the parameters θ_i using classical optimization algorithms until convergence. This approach is particularly advantageous for condensed matter and materials physics problems, where local interactions allow the Hamiltonian to be decomposed into sums of operators that can be evaluated in parallel. Quantum algorithms for direct Hamiltonian simulation address the numerical solution of Schrödinger's equation by decomposing time evolution into a sequence of sub-intervals over which individual Hamiltonian components are evolved independently. This decomposition enables a runtime scaling of $\mathcal{O}(\mathrm{poly}(\mathrm{n})\frac{t}{\epsilon})$, where n is the number of qubits, t is the evolution time, and ϵ is the desired simulation accuracy. In contrast, direct classical simulation of generic quantum dynamics scales as $\mathcal{O}(\exp(\mathrm{n})\frac{t}{\epsilon})$, highlighting the exponential advantage achievable through quantum simulation techniques.

Quantum Fourier transform. The quantum Fourier transform (QFT) is a fundamental primitive in quantum computing and plays a central role in accelerating key subroutines on quantum hardware (Coppersmith, 2002; Sutor, 2024; Nielsen and Chuang, 2010). The QFT constitutes a critical building block in several cornerstone quantum algorithms, including quantum phase estimation, the HHL algorithm, Shor's factoring algorithm, and quantum algorithms for Hamiltonian simulation. In particular, quantum phase estimation — a core component of the HHL algorithm — is typically organized into three main stages: (i) preparation of a uniform superposition over the clock (control) register using Hadamard gates, (ii) controlled unitary operations that imprint eigenphase information onto the control register, and (iii) application of the inverse quantum Fourier transform (IQFT), which converts the accumulated phases into a binary representation such that the eigenvalues of the coefficient matrix become encoded in the clock qubits. In Shor's algorithm, the QFT is employed to extract the period associated with modular exponentiation, thereby enabling efficient integer factorization. In quantum Hamiltonian simulation, the QFT is used to switch between conjugate representations (e.g., position and momentum), where the transform facilitates evolution in a basis in which the Hamiltonian (or a component thereof) is more easily implemented, followed by the IQFT to return to the real-space (position) representation. A useful comparison arises with the classical fast Fourier transform (FFT). On a classical computer, the FFT applied to $\mathrm{N} = 2^{\mathrm{n}}$ data points requires $\mathcal{O}(\mathrm{N}\log(\mathrm{N}))$ time, surprisingly the QFT on a quantum computer can be implemented in $\mathcal{O}((\log(\mathrm{N}))^2)$ time. This asymptotic improvement indicates that, for large problem sizes, quantum computers can perform Fourier transforms substantially faster than classical computers, provided that data are available in a suitable quantum-encoded form and that state preparation and readout costs do not dominate the overall complexity. Consequently, the QFT provides a natural bridge between Fourier-based classical numerical methods and quantum algorithmic primitives, motivating its use in quantum–classical hybrid workflows.

Quantum computing in solid mechanics. Quantum computing has recently been explored as an enabling technology for numerical methods in solid mechanics, motivated by its potential to reduce computational complexity and accelerate selected classes of calculations beyond what is achievable with purely classical algorithms. In particular, quantum algorithms have been investigated for the solution of partial differential equations, boundary value problems, and the large-scale linear systems that arise routinely in finite difference and finite element discretizations. Although the practical performance of quantum methods depends on state preparation, noise, and readout overheads, the underlying algorithmic scaling motivates continued development of quantum and quantum–classical hybrid approaches for computational mechanics. Several representative contributions illustrate the current landscape. For example, Cao et al. (2013) proposed a quantum algorithm for the Poisson equation, introducing a quantum finite-difference formulation in which the Laplacian operator is embedded into a Hamiltonian and solved via Hamiltonian simulation techniques; subsequent advances in quantum finite-difference methods were reported by Miyamoto and Kubo (2021). In the context of finite

element methods (FEM), Montanaro and Pallister (2016) developed a quantum algorithm for accelerating the solution of linear systems associated with boundary value problems, drawing inspiration from the HHL-algorithm and demonstrating polynomial speedup under standard complexity assumptions. Extending this direction to near-term devices, Arora et al. (2025) developed a Quantum-FEM framework for the steady-state heat equation using linear and quadratic shape functions on noisy quantum hardware by employing a variational quantum linear solver. Beyond direct PDE solvers, quantum optimization paradigms have also been introduced for structural design. In particular, Sukulthanasorn et al. (2025) investigated quantum annealing for topology optimization and the design of truss and continuum structures. Iterative quantum-inspired approaches to FEM linear systems have been explored as well, such as the quantum relaxation algorithm proposed by Raisuddin and De (2024). At the scale-bridging level, Liu et al. (2024) proposed a quantum representative volume element (RVE) solver and demonstrated its application to the Poisson equation. Lastly, Lubasch et al. (2025) reported the use of QFT-based primitives for solving partial differential equations, including incompressible advection, heat conduction, isotropic acoustic wave propagation, and Poisson's equations. Collectively, these studies indicate a growing interest in leveraging quantum algorithmic primitives — particularly those related to linear algebra and Fourier analysis — to accelerate computational workflows relevant to solid mechanics.

Crystal plasticity theory. At the microscopic scale, metallic materials are composed of crystalline lattices whose mechanical response under external loading arises from the combined contributions of elastic and plastic deformation mechanisms (Tang et al., 2023; Dadhich and Alankar, 2022; Ahmadikia et al., 2021; Lindroos et al., 2022a; Agius et al., 2022). While elastic deformation is associated with reversible lattice distortion, plastic deformation in crystalline solids occurs primarily through the glide of dislocations along specific crystallographic directions and planes, commonly referred to as slip systems. The heterogeneity of plastic deformation at the crystal scale and its interaction with crystallographic orientation have been studied extensively within the framework of classical crystal plasticity (CCP) theory, which has provided a robust foundation for modeling anisotropic plastic behavior in crystalline materials (Ryś et al., 2022; You et al., 2023; Lindroos et al., 2022b; Ren et al., 2021; Pai et al., 2022; Cao et al., 2025; White et al., 2025; Li et al., 2025; Wang et al., 2025; Zhang and Sumigawa, 2025; Toursangsaraki et al., 2025; Pai et al., 2025), deformation twin (Sudhalkar et al., 2025), creep (Roy et al., 2025), and hydrogen diffusivity via grain boundaries (Ding et al., 2024). Furthermore, strain localization arises as a consequence of heterogeneous plastic deformation and numerical instabilities in computational implementations. For example, Clayton (2024) investigated shear localization coupled with phase transformation, while dynamic indentation (Clayton et al., 2023) and the dynamic behavior and phase transformation of high-strength steels (Williams et al., 2025) were also investigated. In addition, aspects of strain localization have recently been examined in the context of fatigue, such as slip band formation in single-crystal copper (Yan et al., 2020) and single-crystal nickel (Sumigawa et al., 2024). However, the explicit introduction of dislocation concepts has revealed important limitations of the CCP framework. In particular, the distinction between statistically stored dislocations (SSDs) and geometrically necessary dislocations (GNDs), formalized by Nye (1953), has been shown to be essential for capturing size-dependent plasticity effects, such as the Hall–Petch effect and other scale-sensitive phenomena. These observations motivated the development of strain gradient crystal plasticity (SGCP) theories, in which gradients of plastic deformation are incorporated to account for the additional hardening associated with GNDs. An early and influential contribution in this direction was provided by Gurtin (2002), who proposed an SGCP formulation based on the Nye tensor, establishing a direct connection between lattice curvature and GND density. Subsequent developments have introduced alternative gradient measures to address specific shortcomings of Nye-tensor-based formulations. For example, Wulfinghoff and Böhlke (2012) proposed a strain gradient crystal plasticity model based on the total cumulative shear strain, which offers improved robustness in problems involving strain localization. This approach was later extended by Lame Jouybari et al. (2024) to incorporate cumulative shear strain contributions associated with individual slip systems, thereby enhancing the physical resolution of slip-system-level plasticity. In general, SGCP models introduce an intrinsic material length scale or nonlocal parameter through nonlocal field equations, which governs the influence of strain gradients on the material response. In most existing formulations, this length scale is assumed to be constant throughout the deformation process. Experimental evidence, however, suggests that the intrinsic length scale is closely linked to evolving microstructural features and should not necessarily be treated as a fixed material parameter. Observations from microbending and microtorsion experiments indicate that strain gradient effects are most pronounced during the early stages of deformation and progressively diminish as plastic flow develops, implying that microstructural evolution can reduce size effects at higher deformation levels. This behavior motivates the interpretation of the length scale as an evolving quantity that reflects changes in the underlying dislocation glide. Along these lines, Zbib and Aifantis (1998) developed gradient-dependent constitutive relations for parabolic hardening and softening behaviors, later extending the concept to damage-dependent length scales that control damage localization and two-surface damage-plasticity (Brepols et al., 2020). Furthermore, Dahlberg and Boasen (2019) directly linked the intrinsic length scale to the dislocation density, while Petryk and Stupkiewicz (2016) related it to strain-rate gradients. Additional micromorphic and gradient-enhanced formulations have been proposed to regulate strain localization, including the micromorphic crystal plasticity model based on cumulative shear strain developed by Scherer et al. (2019) and the strain gradient plasticity framework with a saturating internal variable introduced by Abatour and Forest (2024). More recently, Lame Jouybari et al. (2025), Lame Jouybari (2026) proposed an enhanced strain gradient crystal plasticity theory based on the Nye tensor, in which the intrinsic length scale is explicitly coupled to microstructural evolution in irradiated materials during deformation. Collectively, these developments highlight the central role of microstructural evolution in strain gradient plasticity and motivate ongoing efforts to formulate physically informed, adaptive length-scale models within crystal plasticity theory.

Irradiated material. Since the Chicago Pile-1 reactor is achieved critical operation in December 1942, sustained efforts have been devoted in improving both the efficiency and safety of the structural integrity of nuclear reactor components. During reactor operation, fast neutrons emitted from the fission chain reaction interact with structural internals and can generate irradiation-induced lattice defects, here collectively referred to as irradiation defects. These defects alter the microstructure through the creation and evolution of point defects, defect clusters, and related damage features, and they consequently modify the mechanical response and macroscopic behavior of reactor materials. Reported consequences include a reduction of toughness and ductility, an increase in yield strength, and a contraction of the work-hardening regime, all of which can significantly affect component reliability and lifetime. Despite the pronounced loss of ductility observed in many irradiated alloys, fracture surface analyses of irradiated materials, including stainless steels, have shown that the dominant fracture mechanism can remain ductile, albeit characterized by intense microscopic localization of plastic deformation (El Shawish et al., 2016; Hesterberg et al., 2019; Lame Jouybari et al., 2023). This apparent paradox has been rationalized by the emergence of highly localized deformation patterns that promote early failure even when macroscopic plasticity is strongly suppressed. Consistent with this interpretation, transmission electron microscopy (TEM) observations have confirmed the formation of narrow, defect-free channels — often termed clear channels — in which irradiation defects are swept away by gliding dislocations during the plastic part of deformation (Thomas et al., 2019). The development of such channels concentrates plastic slip into a small fraction of the microstructure, thereby enhancing strain localization and accelerating ductile damage accumulation. Accordingly, clear-channel formation is widely regarded as a primary microstructural mechanism underlying premature ductile failure in irradiated alloys.

Fast Fourier transform-method. The fast Fourier transform (FFT)-based method for solving the classical balance (Cauchy equilibrium) equation in heterogeneous media was first introduced in the pioneering work of Moulinec and Suquet (1998). In this approach, the heterogeneous material is reformulated by introducing an auxiliary homogeneous reference elastic medium, which enables the governing equations to be reformulate into the *Lippmann–Schwinger* integral equation. The resulting formulation is particularly well suited to periodic microstructures and benefits from the efficient evaluation of convolution operators in Fourier space. Owing to its computational efficiency and its natural compatibility with voxelized microstructures obtained from imaging, the FFT-based method has become a paradigm in computational micromechanics. In particular, compared with standard finite element implementations whose computational cost can scale as $\mathcal{O}(N^2)$ for large-scale discretizations, FFT-based solvers reduce the dominant cost to $\mathcal{O}(N\log(N))$, where N denotes the number of elements or voxels with the discretized representative domain. It is worth mentioning that several approaches have been proposed to reduce computational cost in finite element simulations of hyperelastic materials. Notably, the so-called corrected cluster cubature (E3C) hyper-reduction method has been developed to significantly reduce CPU time (Wulfinghoff, 2025, 2026). In addition, data-driven computational approaches have been explored in the context of micromorphic continua (Ulloa et al., 2024). The convergence behavior of the original FFT fixed-point scheme, however, was shown to depend strongly on the choice of the auxiliary reference material and on the contrast between phases in the heterogeneous medium. High phase contrast and suboptimal reference selection can lead to slow convergence or even numerical divergence, thereby motivating substantial subsequent efforts to improve robustness and efficiency. A variety of enhanced formulations have therefore been proposed, including polarization-based schemes (Wicht et al., 2021), Krylov-subspace accelerations (Brisard and Dormieux, 2010), collocation-based methods (Zeman et al., 2010), and Fourier–Galerkin schemes (Lucarini and Segurado, 2019). Collectively, these developments have significantly broadened the applicability of FFT-based solvers, particularly for strongly heterogeneous materials and nonlinear constitutive behavior.

Contribution of this study. For the first time, this study introduces a QFT-method into classical crystal plasticity framework and strain gradient crystal plasticity (SGCP) theory in order to accelerate Fourier-based computations that arise in FFT-method solvers. Specifically, the proposed approach targets a reduction of the asymptotic runtime of the Fourier transform step from $\mathcal{O}(N\log(N))$ in the classical FFT-method to $\mathcal{O}((\log(N))^2)$ using QFT primitives, yielding poly-logarithmic complexity according to the domain resolution. This acceleration is particularly advantageous for high-resolution simulations of polycrystalline aggregates, where the number of voxels N can become prohibitively large in three-dimensional analyses. The QFT-method is presented in details, including the complete algorithmic workflow as well as the required intermediate steps and mathematical proofs and justifications. In addition, the study revisits several SGCP models from the recent literature, organized here as the Classical MicroSlip-SGCP (CMSlip) model, the Classical MicroCurl-SGCP (CMCurl) model, and the Enhanced MicroCurl-SGCP (EMCurl) model. Building upon these frameworks, a new branch of ESGCP theory is introduced in the form of an Enhanced MicroSlip-SGCP (EMSlip) model driven by the cumulative shear strain associated with each slip system. Moreover, modified operators are incorporated into the CMCurl and EMCurl models; these models are denoted in this work as the CMCurl-Star and EMCurl-Star models. For each of the considered SGCP models, the corresponding QFT-method formulation within the quantum finite difference method is derived and discussed in detail, ensuring a consistent quantum–classical mapping of the governing operators. Finally, the proposed QFT-method is demonstrated through two-dimensional and three-dimensional simulations of irradiated polycrystalline aggregates subjected to tensile loading, thereby illustrating its applicability to the plastic deformation. It is emphasized that all quantum algorithms in this study are implemented using the quantum computing toolbox[1] in Matlab (2025) and executed on an ideal (noiseless) quantum simulator, providing a baseline assessment of the method prior to hardware development.

[1] The proposed algorithms can be implemented in any software equipped with a quantum computing toolbox.

Outline. The paper is organized as follows. Section 2.1 summarizes the classical crystal plasticity (CCP) framework adopted for irradiated crystals. Section 2.2 reviews the classical strain gradient crystal plasticity (SGCP) formulations considered in this work, namely the CMSlip, CMCurl, and CMCurl-Star models. Section 2.3 first revisits the EMCurl-SGCP model and subsequently introduces the EMCurl-Star and EMSlip extensions. Section 2.5 presents the proposed quantum Fourier transform-method in detail, including its integration into the CCP framework and into each of the SGCP models. Section 3 reports numerical results obtained with the proposed QFT-method for high-resolution two-dimensional and three-dimensional polycrystalline aggregates, with emphasis on the formation of strain localization (e.g., shear bands or clear channels) and on the influence of mean grain size. A complete set of appendices is also provided to support reproducibility and to document implementation details. Appendix A summarizes fundamental concepts in quantum computing, including the quantum bit, quantum gates, and circuit representations. Appendix B presents the state-preparation procedure (amplitude encoding) used to transfer crystal's state variables to quantum states. Appendix C details the QFT circuit and its application within the quantum finite difference method. Appendix D provides validation of the QFT-method implementation against analytical solutions for representative constitutive responses, including linear elasticity, perfect plasticity, linear softening, and nonlinear softening behaviors. Finally, Appendix E presents additional analyses of slip and kink bands formation in two-dimensional single-crystal simulations equipped with SGCP models under tensile loading.

Notation. This study captures the typical notation for the tensor analysis in the crystal plasticity for example, the scalar, first-order (vector), second-order, third-order, and fourth-order tensors represented as A, $\underline{A}$, $\underset{\sim}{A}$, $\underline{\underline{A}}$, and $\underset{\approx}{A}$, respectively. The Levi-Civita third order permutation tensor is represented by $\underline{\underline{\epsilon}}$. Furthermore, the superscripts over the letters such as $^{\mathrm{tot}}$,$^{\mathrm{e}}$,$^{\mathrm{p}}$,$^{\cdot}$, $\hat{}$, *, and - are denoted for the total, elastic, plastic, time derivative, Fourier transform, fluctuation, and spatial mean value part of the tensor, respectively. Also, mathematical symbols such as $\otimes, \times, *, ., :, \nabla, \nabla ., \nabla\times$, and Δ denote the tensor product, cross product, convolution, dot product, double contraction, gradient, divergence, curl and Laplacian operators. For example the curl of the second order tensor is calculated as $\nabla \times \underset{\sim}{X} = \epsilon_{jms} X_{im,s} \underline{e}_i \otimes \underline{e}_j$ in the Cartesian coordinate basis in the real space such as $(\underline{e}_1, \underline{e}_2, \underline{e}_3)$, and the Einstein's summation convention is used in indicial representations. Furthermore, the norm of the second order tensor is calculated as $\|\underset{\sim}{X}\| = \sqrt{\underset{\sim}{X} : \underset{\sim}{X}}$, and the symmetric and skew-symmetric parts of the second order tensor are calculated as $\mathrm{Sym}(\underset{\sim}{X}) = (\underset{\sim}{X} + \underset{\sim}{X}^T)/2$, and $\mathrm{Skew}(\underset{\sim}{X}) = (\underset{\sim}{X} - \underset{\sim}{X}^T)/2$. Lastly, the *Dirac* (bra-ket) notation is used in the quantum computing (see Appendix A).

2. Material and methods

This section presents the theoretical frameworks and the computational methodology employed in this study. First, the classical crystal plasticity (CCP) formulation is recalled in the infinitesimal deformation framework.[2] Due to the irradiation effect on the crystalline lattices such as increasing of yield stress, reduction of ductility and work hardening domain, and strain localization, this framework is promising in the analysis of this crystalline lattices.[3] Furthermore, a summary of the classical strain gradient crystal plasticity (CSGCP) and EMCurl model variants considered herein. Next, a new branch of the enhanced strain gradient crystal plasticity (ESGCP) theory is introduced in the form of the EMSlip model. Finally, the proposed quantum Fourier transform-method and the associated algorithmic workflow are presented, including their integration within the CCP framework and within each of the SGCP models investigated in this work.

2.1. Classical crystal plasticity

In the infinitesimal deformation–rotation framework of CCP, the total displacement gradient tensor is assumed to admit an additive decomposition into elastic and plastic parts, as stated in Eq. (1). The elastic strain tensor is then identified as the symmetric part of the elastic displacement gradient, Eq. (6). The plastic part of the tensor is governed by crystallographic slip and is expressed through the rate of the plastic displacement gradient, which is defined as the sum over all active slip systems, N_α, as given in Eq. (2).

$$(\nabla \underline{u})^{\mathrm{tot}} = (\nabla \underline{u})^{\mathrm{e}} + (\nabla \underline{u})^{\mathrm{p}} \tag{1}$$

$$(\nabla \dot{\underline{u}})^{\mathrm{p}} = \frac{d}{dt}\left((\nabla \underline{u})^{\mathrm{p}}\right) = \sum_{\alpha}^{N_\alpha} \dot{\gamma}^\alpha \underline{m}^\alpha \otimes \underline{n}^\alpha \tag{2}$$

Assuming the absence of body, inertial forces, and quasi-static deformation, the principle of virtual power leads to:

$$\nabla . \underset{\sim}{\sigma} = \underline{0} \quad \forall \underline{x} \in \mathcal{B} \tag{3}$$

$$\underline{t} = \underset{\sim}{\sigma} . \underline{n} \quad \forall \underline{x} \in \partial\mathcal{B} \tag{4}$$

Within a thermodynamically consistent framework, an isothermal specific Helmholtz free-energy density is postulated in the form $\psi = \psi\left(\underset{\sim}{\varepsilon}^{\mathrm{e}}, \gamma^\alpha_{\mathrm{cum}}\right)$, where the potential depends on the elastic strain tensor, Eq. (6), and on the cumulative shear strain $\gamma^\alpha_{\mathrm{cum}}$ for each slip system, Eq. (9). By adopting a quadratic form in the elastic strain and in the cumulative shear strain and enforcing the

[2] This framework is modified to capture the skew-symmetric part of the displacement gradient tensor.

[3] Extending this framework to finite deformations for unirradiated crystalline lattices is also possible; however, it introduces additional computational costs.

Clausius–Duhem inequality, constitutive equations are obtained for the Cauchy stress tensor, the slip evolution (shear strain rate), and the critical resolved shear stress.

$$\underset{\sim}{\sigma} = \underset{\approx}{C} : \underset{\sim}{\varepsilon}^{\mathrm{e}} \tag{5}$$

$$\underset{\sim}{\varepsilon}^{\mathrm{e}} = \frac{1}{2}\left((\nabla \underline{u})^{\mathrm{e}} + (\nabla \underline{u})^{\mathrm{eT}}\right) \tag{6}$$

$$\dot{\gamma}^{\alpha} = \mathrm{sign}\,(\tau^{\alpha})\left\langle \frac{|\tau^{\alpha}| - \tau^{\alpha}_{\mathrm{cr}}}{K} \right\rangle^{n} \tag{7}$$

$$\tau^{\alpha}_{\mathrm{cr}} = \tau^{\alpha}_{0} - \Delta\tau^{\alpha}\left[1 - \exp\left(-\frac{\gamma^{\alpha}_{cum}}{\gamma_0}\right)\right] + H^{\alpha}\gamma^{\alpha}_{cum} \tag{8}$$

$$\gamma^{\alpha}_{cum} = \int_0^{\mathrm{t}} |\dot{\gamma}^{\alpha}|\ d\mathrm{t} \tag{9}$$

Here K, n, τ^{α}_{0}, $\Delta\tau^{\alpha}$, and γ_0 are respectively denoted as the Norton flow coefficient, Norton flow exponent, initial critical resolved shear stress, the maximum softening, and the softening rate parameters. These parameters are correlated with the experimental physics-based models which formulated for the irradiated materials following Lame Jouybari et al. (2024).

2.2. Classical strain gradient crystal plasticity theory

The classical strain gradient crystal plasticity (CSGCP) theory is used here to denote models in which the nonlocal parameter (intrinsic length scale) is prescribed as a fixed material constant, $A = \mathrm{const}$. Within this class, two previously developed SGCP models are recalled, namely the MicroCurl model (Marano et al., 2021) and the MicroSlip-SGCP model (Lame Jouybari et al., 2024). For clarity, the Classical MicroCurl formulation is hereafter referred to as the CMCurl model and employs the Nye tensor as the gradient variable. The MicroSlip-SGCP formulation is hereafter referred to as the CMSlip model and uses the cumulative shear strain associated with each slip system as the gradient variable. In both models, the nonlocal parameter is assumed to remain constant throughout deformation, and serves as the weight to the strain gradient effect. Furthermore, Appendix A of Lame Jouybari et al. (2024) shows that this parameter can be physically interpreted in terms of the dislocation pile-up mechanism, with its magnitude directly related to the initial critical resolved shear stress, τ_0, and the characteristic length of the dislocation pile-up.

2.2.1. Classical MicroCurl strain gradient crystal plasticity model

The classical strict MicroCurl strain gradient crystal plasticity (CMCurl) model is recalled here (Marano et al., 2021; Gurtin, 2002). The formulation is constructed on the basis of the Nye tensor, $\underset{\sim}{\alpha} = -\nabla \times \left(\nabla \underline{u}\right)^{p}$ (Nye, 1953), which captures the lattice curvature within the infinitesimal deformation–rotation framework. In this model, the Nye tensor quantifies the incompatibility of the plastic distortion and provides a kinematically consistent representation of geometrically necessary dislocations (Lame Jouybari et al., 2025). When the Nye tensor is considered as an gradient variable, the principle of virtual power yields, in addition to the classical Cauchy equilibrium equation and its associated boundary condition from the CCP framework, a nonlocal field equation and corresponding higher-order boundary condition, as summarized in Eqs. (3) and (4).

$$\underset{\sim}{s} + \nabla \times \underset{\sim}{M} = \underset{\sim}{0}, \qquad \forall \underline{x} \in \mathcal{B}, \tag{10}$$

$$\underset{\sim}{m} = \underset{\sim}{M} \cdot \underset{\approx}{\epsilon} \cdot \underline{n}, \qquad \forall \underline{x} \in \partial\mathcal{B}. \tag{11}$$

Following a thermodynamically consistent framework, the specific free-energy density is postulated in quadratic form as $\psi = \rho\psi(\underset{\sim}{\varepsilon^{e}}, \nabla \times \left(\nabla \underline{u}\right)^{p}, \gamma^{\alpha}_{cum}, \gamma^{\alpha})$, where the potential depends on the elastic strain, the Nye tensor, cumulative shear strain, and shear strain. By enforcing the *Clausius–Duhem* inequality, constitutive equations are obtained for the double-stress in Eq. (12), the micro-stress tensor in Eqs. (14) and (15), the back-stress in Eq. (16), the shear strain rate in Eq. (17), and the critical resolved shear stress in Eq. (8), respectively, in application to irradiated materials.

$$\underset{\sim}{M} = A\nabla \times \left(\nabla \underline{u}\right)^{p} \tag{12}$$

$$\underset{\sim}{s} = -\nabla \times (\underset{\sim}{M}) = -\nabla \times \left(A\nabla \times \left(\nabla \underline{u}\right)^{p}\right) \tag{13}$$

$$= -A\left\{\nabla \times \nabla \times \left(\nabla \underline{u}\right)^{p}\right\} \tag{14}$$

$$= -A\left\{\nabla \otimes \nabla . \left(\nabla \underline{u}\right)^{p} - \Delta\left(\nabla \underline{u}\right)^{p}\right\} \tag{15}$$

$$\chi^{\alpha} = -\underset{\sim}{s} : \left(\underline{m}^{\alpha} \otimes \underline{n}^{\alpha}\right) \tag{16}$$

$$\dot{\gamma}^{\alpha} = \mathrm{sign}\,(\tau^{\alpha} - \chi^{\alpha})\left\langle \frac{|\tau^{\alpha} - \chi^{\alpha}| - \tau^{\alpha}_{cr}}{K} \right\rangle^{n} \tag{17}$$

It has previously been reported that the frequency-domain representation of Eq. (13) exhibits a small amplitude within the slip band, owing to the modified frequency representation of the Curl operator in Fourier space (Marano et al., 2021). Accordingly, this study considers two different approaches for evaluating the micro-stress tensor. Further details are provided in Appendices C.3 and E. Specifically, Eq. (14) is used in the CMCurl-Star model (the modified frequency corresponds to the Eq. (C.32)), whereas Eq. (15) defines the CMCurl model (the modified frequency corresponds to the Eq. (C.33)). Notably, in both formulations, the higher-order stress (or back-stress) contributes to the shear flow rule through a kinematic hardening term.

2.2.2. Classical MicroSlip strain gradient crystal plasticity model

The classical strict MicroSlip strain gradient crystal plasticity model is hereafter referred to as the CMSlip model (Lame Jouybari et al., 2024). This model is constructed using the cumulative shear strain associated with each slip system, γ^{α}_{cum}. By applying the principle of virtual power, the corresponding nonlocal field equation, Eq. (18), and the associated higher-order boundary condition, Eq. (19), are obtained.

$$\nabla.\underline{M}^{\alpha} - \chi^{\alpha} = 0 \qquad \forall \underline{x} \in \mathcal{B}, \quad \forall \alpha \in N_{\alpha} \tag{18}$$

$$m^{\alpha} = \underline{M}^{\alpha}.\underline{n} \qquad \forall \underline{x} \in \partial\mathcal{B}, \forall \alpha \in N_{\alpha} \tag{19}$$

Following a thermodynamically consistent framework, the specific free-energy density is postulated in quadratic form as $\psi = \rho\psi(\underset{\sim}{\varepsilon}^{e}, \nabla\gamma^{\alpha}_{cum}, \gamma^{\alpha}_{cum}, \gamma^{\alpha})$, where the potential depends on the elastic strain, the gradient of the cumulative shear strain, cumulative sheat strain, and shear strain. By enforcing the *Clausius–Duhem* inequality, constitutive equations are obtained for the double-stress in Eq. (20), the higher-order stress in Eq. (21), the shear strain rate in Eq. (22), and the critical resolved shear stress in Eq. (8), respectively.

$$\underline{M}^{\alpha} = A\nabla\gamma^{\alpha}_{\mathrm{cum}} \tag{20}$$

$$\chi^{\alpha} = A\Delta\gamma^{\alpha}_{\mathrm{cum}} \tag{21}$$

$$\dot{\gamma}^{\alpha} = \mathrm{sign}\left(\tau^{\alpha}\right)\left\langle \frac{|\tau^{\alpha}| - \tau^{\alpha}_{\mathrm{cr}} + \chi^{\alpha}}{K} \right\rangle^{n} \tag{22}$$

Notably, in this formulation the higher-order stress enters the shear flow rule as an isotropic hardening term.

2.3. Enhanced strain gradient crystal plasticity theory

The Enhanced Strain Gradient Crystal Plasticity (ESGCP) theory was recently introduced in Lame Jouybari et al. (2025). In this framework, the nonlocal parameter — referred to therein as the higher-order modulus — is allowed to inherit microstructural evolution during deformation and loading. For irradiated materials, this feature is particularly relevant: as irradiation defects are locally swept away by gliding dislocations, pronounced local softening can form, and the higher-order modulus is correspondingly reduced within these softened regions, which are often associated with shear-band formation. It was shown that this local reduction of the higher-order modulus is essential, as it reduces the magnitude of the higher-order stresses and, as a consequence, promotes sustained strain localization at larger deformation levels. Accordingly, this section first recalls the EMCurl model of Lame Jouybari et al. (2025), which is formulated in terms of the Nye tensor. Subsequently, an EMSlip model is introduced, in which the gradient measure is based on the cumulative shear strain associated with each slip system.

2.3.1. Enhanced MicroCurl strain gradient crystal plasticity model

Similar to the CMCurl model discussed in Section 2.2.1, the EMCurl model is formulated in terms of the Nye tensor (Lame Jouybari et al., 2025). By adopting the same theoretical setting — in which the Nye tensor is treated as gradient variable and the principle of virtual power is applied — the classical balance and nonlocal field equations, Eqs. (3) and (10), together with the corresponding boundary conditions in Eqs. (4) and (11), are obtained in the same manner as for the CMCurl model. The essential difference between the two formulations arises from the thermodynamic aspect of the higher-order modulus. In the enhanced model, the higher-order modulus is no longer assumed to be constant; instead, it is taken to evolve with deformation and is here prescribed as a function of the cumulative shear strain, $A^{\alpha} = A^{\alpha}\left(\gamma^{\alpha}_{\mathrm{cum}}\right)$. Accordingly, the specific Helmholtz free energy is postulated to incorporate contributions associated with both stored (non-dissipative) energy and dissipated energy during deformation, thereby enabling a thermodynamically consistent coupling between microstructural evolution and the higher-order stress response.

$$\begin{aligned}\rho\psi &= \rho\psi(\underset{\sim}{\varepsilon}^{e}, \nabla\times\left(\nabla\underline{u}\right)^{p}, \gamma^{\alpha}_{cum}, \gamma^{\alpha}) \\ &= \tfrac{1}{2}\underset{\sim}{\varepsilon}^{e} : \underset{\approx}{C} : \underset{\sim}{\varepsilon}^{e} + \tfrac{1}{2}A\left(\gamma^{\alpha}_{cum}\right)\nabla\times\left(\nabla\underline{u}\right)^{p} : \nabla\times\left(\nabla\underline{u}\right)^{p} + \rho\psi^{h}\left(\gamma^{\alpha}_{cum}\right)\end{aligned} \tag{23}$$

Applying the *Clasius-Duhem* inequality leads to:

$$\underset{\sim}{M}^{\alpha} = A^{\alpha}\nabla\times\left(\nabla\underline{u}\right)^{p} \tag{24}$$

$$\begin{aligned}\underset{\sim}{s}^{\alpha} &= -\nabla\times\underset{\sim}{M}^{\alpha} = -\nabla\times\left(A^{\alpha}\nabla\times\left(\nabla\underline{u}\right)^{p}\right) \\ &= -\left[\{\nabla A^{\alpha}\}\times\nabla\times\left(\nabla\underline{u}\right)^{p} + A^{\alpha}\left\{\nabla\times\nabla\times\left(\nabla\underline{u}\right)^{p}\right\}\right] \qquad (25) \\ &= -\left(\nabla A^{\alpha}\right)\times\nabla\times\left(\nabla\underline{u}\right)^{p} - A^{\alpha}\left\{\nabla\otimes\nabla.\left(\nabla\underline{u}\right)^{p} - \Delta\left(\nabla\underline{u}\right)^{p}\right\} \qquad (26)\end{aligned}$$

$$\Gamma^{\alpha} = \frac{1}{2}\left[\nabla\times\left(\nabla\underline{u}\right)^{p} : \nabla\times\left(\nabla\underline{u}\right)^{p}\right]\frac{\partial A^{\alpha}}{\partial\gamma^{\alpha}} \tag{27}$$

$$\dot{\gamma}^{\alpha} = \mathrm{sign}\left(\tau^{\alpha} - \chi^{\alpha} - \Gamma^{\alpha}\right)\left\langle \frac{|\tau^{\alpha} - \chi^{\alpha} - \Gamma^{\alpha}| - \tau^{\alpha}_{cr}}{K} \right\rangle^{n} \tag{28}$$

Here, Eq. (25) is employed in the EMCurl-Star model, whereas Eq. (26) corresponds to the EMCurl model. In addition, the generalized back-stress, Γ^{α}, is introduced in Eq. (27) and is incorporated into the shear flow rule as a kinematic hardening contribution,

analogous to the back-stress term in Eq. (16). Furthermore, the higher-order modulus A^α is defined as the second derivative of the hardening part of the free energy, $\rho\psi^h$, with respect to the cumulative shear strain in each slip system. To maintain the dimensional consistency of the micro-stress tensor, the coefficient, $(\Lambda_0/2\pi)^2$, is incorporated within the expression of the higher-order modulus which includes the length scale Λ_0 in the unit of meter.[4]

$$A^\alpha := -\rho\left(\frac{\Lambda_0}{2\pi}\right)^2\frac{d^2\psi^h}{d\gamma_{cum}^{\alpha 2}} = -\left(\frac{\Lambda_0}{2\pi}\right)^2\frac{d\tau_{\mathrm{cr}}^\alpha}{d\gamma_{cum}^\alpha} = \left(\frac{\Lambda_0}{2\pi}\right)^2\frac{\Delta\tau^\alpha}{\gamma_0}\exp\left(-\frac{\gamma_{cum}^\alpha}{\gamma_0}\right) \tag{29}$$

Accordingly, microstructural characteristics associated with softening behavior — specifically the maximum softening parameter $\Delta\tau^\alpha$, the softening rate parameter γ_0, and the cumulative shear strain $\gamma_{\mathrm{cum}}^\alpha$ — are incorporated into the constitutive definition of the higher-order modulus A^α.

2.3.2. Enhanced MicroSlip strain gradient crystal plasticity model

The Enhanced MicroSlip Strain-Gradient Crystal Plasticity (EMSlip) model is constructed on the same kinematic foundation as the CMSlip formulation presented in Section 2.2.2. As in the classical theory, the cumulative shear strain on each slip system, $\gamma_{\mathrm{cum}}^\alpha$, is treated as an internal state variable, and the principle of virtual power is employed to derive the governing balance equation. Consequently, the formulation retains the classical balance and nonlocal field equations, Eqs. (3) and (18), together with the associated boundary conditions in Eqs. (4) and (19). Similar to Section 2.3.1, the higher-order modulus is no longer assumed to be constant but is instead allowed to evolve with deformation. To accommodate this dependence in a thermodynamically consistent manner, the specific Helmholtz free-energy density is postulated as follows.

$$\psi = \psi(\underset{\sim}{\varepsilon}^{\mathrm{e}}, \gamma_{\mathrm{cum}}^\alpha, \nabla\gamma_{\mathrm{cum}}^\alpha) = \tfrac{1}{2\rho}\underset{\sim}{\varepsilon}^{\mathrm{e}} : \underset{\approx}{C} : \underset{\sim}{\varepsilon}^{\mathrm{e}} + \sum_\alpha^{\mathcal{N}}\psi_h^\alpha(\gamma_{\mathrm{cum}}^\alpha) + \sum_\alpha^{\mathcal{N}}\tfrac{1}{2\rho}A\left(\gamma_{cum}^\alpha\right)\ \nabla\gamma_{\mathrm{cum}}^\alpha.\nabla\gamma_{\mathrm{cum}}^\alpha \tag{30}$$

Furthermore, applying the *Clasius-Duhem* inequality leads to:

$$\underline{M}^\alpha = \rho\frac{\partial\psi}{\partial\nabla\gamma_{\mathrm{cum}}^\alpha} = A(\gamma_{\mathrm{cum}}^\alpha)\nabla\gamma_{\mathrm{cum}}^\alpha \tag{31}$$

$$\chi^\alpha = \nabla.\underline{M}^\alpha = \nabla.\left[A(\gamma_{\mathrm{cum}}^\alpha)\nabla\gamma_{\mathrm{cum}}^\alpha\right] = \nabla A(\gamma_{\mathrm{cum}}^\alpha).\nabla\gamma_{\mathrm{cum}}^\alpha + A(\gamma_{\mathrm{cum}}^\alpha)\Delta\gamma_{\mathrm{cum}}^\alpha \tag{32}$$

$$\Gamma^\alpha = \frac{1}{2}\frac{\partial A(\gamma_{\mathrm{cum}}^\alpha)}{\partial\gamma_{\mathrm{cum}}^\alpha}\ \nabla\gamma_{\mathrm{cum}}^\alpha.\nabla\gamma_{\mathrm{cum}}^\alpha \tag{33}$$

$$\dot\gamma^\alpha = \mathrm{sign}\left(\tau^\alpha\right)\left\langle\frac{|\tau^\alpha| - \left(\tau_{\mathrm{cr}}^\alpha - \chi^\alpha + \Gamma^\alpha\right)}{K}\right\rangle^n \tag{34}$$

Here, the second higher-order stress, Γ^α, acts as an isotropic hardening term within the shear flow rule. The higher-order modulus is defined consistently with Eq. (29). Furthermore, the principal similarities and differences between the Classical and Enhanced SGCP theories are summarized in Fig. 1, based on the results reported in Appendix E.

2.4. Periodic Lippmann–Schwinger equation

In the infinitesimal deformation–rotation framework, the periodic *Lippmann–Schwinger* formulation is introduced by decomposing the total displacement gradient tensor field ($\nabla\underline{u}^{\mathrm{tot}}$) into an homogeneous part ($\overline{\nabla\underline{u}}$) and a fluctuating part ($\nabla\underline{u}^\star$). The fluctuation part is assumed to be periodic on the boundary of the body ($\nabla\underline{u}^\star\#\partial\mathcal{B}$), whereas the classical Cauchy traction is generally non-periodic ($\underset{\sim}{\sigma}.\underline{n} - \#\partial\mathcal{B}$). To facilitate the solution of the resulting boundary value problem, an auxiliary homogeneous reference medium is introduced, taken here as an isotropic linear elastic material characterized by the elasticity tensor $\underset{\approx}{C}^0$. Relative to this reference material, a polarization tensor field ($\underset{\sim}{\tau}$) is defined to capture the local deviation of the heterogeneous constitutive response from the reference behavior. By combining the classical Cauchy equilibrium equation with the constitutive relation for the Cauchy stress tensor ($\underset{\sim}{\sigma}$), the periodic *Lippmann–Schwinger* integral equation is obtained, following the original formulation of Lippmann and Schwinger (1950).

$$\begin{cases}\nabla\underline{u}^{\mathrm{tot}}(\underline{x}) = \overline{\nabla\underline{u}} + \nabla\underline{u}^\star(\underline{x}) & \forall\,\underline{x}\in\mathcal{B},\quad \nabla\underline{u}^\star\#\partial\mathcal{B}\\ \underset{\sim}{\sigma}(\underline{x}) = \underset{\approx}{C}(\underline{x}) : \underset{\sim}{\varepsilon}(\underline{x}) & \forall\,\underline{x}\in\mathcal{B},\quad \underset{\sim}{\sigma}.\underline{n} - \#\partial\mathcal{B}\\ \underset{\sim}{\tau}(\underline{x}) = \underset{\sim}{\sigma}(\underline{x}) - \underset{\approx}{C}^0 : \nabla\underline{u}(\underline{x}) & \forall\,\underline{x}\in\mathcal{B}\\ \nabla\cdot\underset{\sim}{\sigma}(\underline{x}) = \underline{0} & \forall\,\underline{x}\in\mathcal{B}\end{cases} \tag{35}$$

Accordingly, the total displacement gradient tensor field, which solves the *Lippmann–Schwinger* equation, can be obtained through two equivalent representations. In real space, the solution is written as a convolution between the Green operator ($\underset{\approx}{\mathrm{G}}$) and the polarization tensor, as given in Eq. (36). Alternatively, in Fourier space, the same solution is expressed through a double contraction of the Green operator with the polarization tensor, as stated in Eq. (37). It is further noted that the Green operator employed here

[4] Analytical calibration in Lame Jouybari et al. (2025) demonstrates that this length scale is exactly equal to the shear band width.

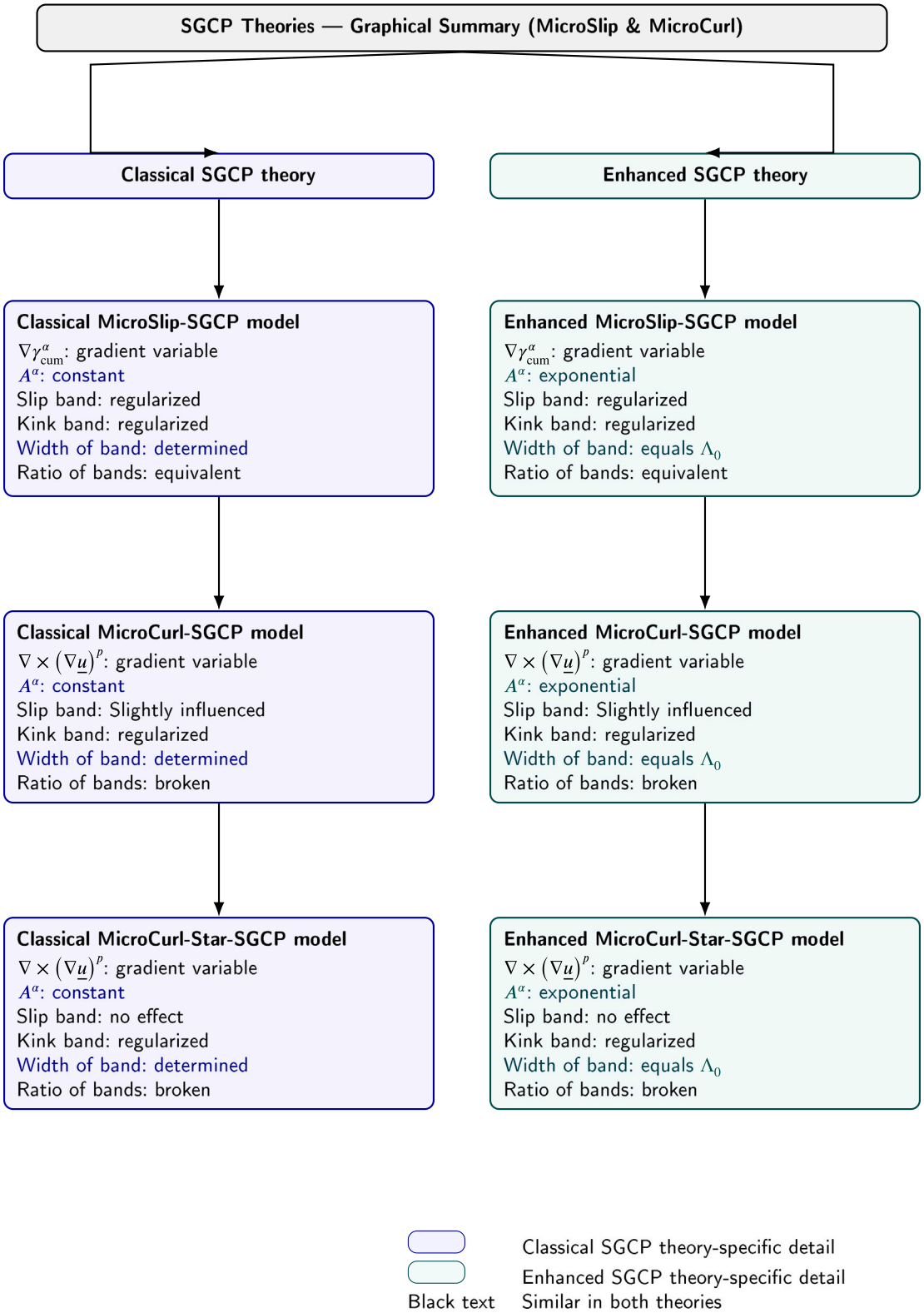

Fig. 1. Schematic comparison of Classical and Enhanced SGCP theories for MicroSlip and MicroCurl models. Color indicates differences; black items are shared.

is general and, in particular, non-symmetric, which is consistent with the use of the non-symmetric displacement gradient tensor field.

$$\text{Real space:} \quad \nabla \underset{\sim}{u}(\underline{x}) = \overline{\nabla \underset{\sim}{u}} - \underset{\approx}{\mathrm{G}} * \underset{\sim}{\tau}(\underline{x}) \tag{36}$$

$$\text{Fourier space:} \quad \nabla \underset{\sim}{u}(\underline{x}) = \overline{\nabla \underset{\sim}{u}} + \mathcal{IDFT}\left(\widehat{\nabla \underset{\sim}{u}}(\underline{\xi})\right) = \overline{\nabla \underset{\sim}{u}} - \mathcal{IDFT}\left(\widehat{\underset{\approx}{\mathrm{G}}}(\underline{\xi}) : \widehat{\underset{\sim}{\tau}}(\underline{\xi})\right) \tag{37}$$

2.5. Quantum Fourier transform-method

Typically, quantum algorithms for solving partial differential equations (PDEs) follow a common workflow that is largely shared across the literature (Tosti Balducci et al., 2022). These steps can be summarized as follows: (1) *Problem setting*: the PDE is specified together with the relevant initial and boundary conditions. (2) *Discretization*: the spatial domain is discretized using an underlying numerical scheme, such as finite differences or finite elements. (3) *Quantum state preparation and superposition*: a quantum register with an appropriate number of qubits is allocated to represent the discretized domain, and the problem variables and parameters are encoded into the qubits. (4) *Quantum primitive*: differential operators associated with the PDE are implemented within the circuit through quantum primitives, thereby modifying the amplitudes and phases of the qubits in accordance with the desired derivatives. (5) *Output and measurements*: the solution on the discretized domain is extracted from the final quantum state via measurement and suitable post-processing. Motivated by this general methodology, the QFT-method is proposed in this study to address the linear momentum balance equation as well as the nonlocal field equations arising in the SGCP models introduced in the previous sections. The direct implementation of the QFT circuit is presented in Appendix C, and its complexity and computational cost are compared with those of the Cooley–Tukey FFT algorithm in Fig. C.3.

2.5.1. Classical crystal plasticity: QFT-method implementation

In the CCP framework, the governing equation to be satisfied at each material point is the *Cauchy* equilibrium equation, i.e., the linear momentum balance equation. Accordingly, within the first step of a quantum-computing workflow, (1) *Problem setting*, Eq. (3) is prescribed as the target equation. As shown in Section 2.4, this balance equation can be reformulated into the periodic *Lippmann–Schwinger* equation, whose solution may be expressed either in real space or in Fourier space. The real-space representation involves a convolution operator, Eq. (36), which becomes computationally expensive for high-resolution discretizations. Therefore, the efficient approach is to evaluate the solution in Fourier space, Eq. (37). In this setting, the polarization tensor field is transformed to Fourier space, double contracted with the Green operator, and subsequently returned back to real space, yielding the total displacement gradient tensor field. To perform this sequence of operations using a quantum algorithm, the following procedure is proposed.

The second step of the quantum-computing workflow corresponds to (2) *Discretization*. Considering a periodic cubic microstructure in three dimensions, with volume $\mathrm{V} = \mathrm{L}^3$, and discretized into uniform cubic voxels such that $\mathrm{N}^{\mathrm{tot}} = \mathrm{N}^3$. A voxel with indices $i, j, k \in \{0, 1, \dots, \mathrm{N}-1\}$ is associated with the Cartesian position $x_{ijk} = \left(x_0 + i \times \Delta x, y_0 + j \times \Delta x, z_0 + k \times \Delta x\right)^{\mathrm{T}} \in \mathbb{R}^3$, where Δx denotes the voxel edge length.

The third step corresponds to (3) *State preparation or superposition*, which is detailed in Appendices A and B. The polarization tensor field, $\underset{\sim}{\tau}$, is defined at all voxels and belongs to $\underset{\sim}{\tau} = \tau_{ij,l} \in \mathbb{R}^{3\times3\times\mathrm{N}^{\mathrm{tot}}}$, where $l \in \left\{1, \dots, \mathrm{N}^{\mathrm{tot}}\right\}$ denotes the voxel index. The tensor field is then rearranged into a normalized vector representation, $\vec{\tau} = \frac{1}{\|\underset{\sim}{\tau}\|}\mathrm{Vec}\left(\underset{\sim}{\tau}\right) \in \mathbb{R}^{9\mathrm{N}^{\mathrm{tot}}}$. A quantum register with $\mathrm{N}^{\text{qb-Pol}} = \left\lceil \log_2\left(9 \times \mathrm{N}^{\mathrm{tot}}\right)\right\rceil$ qubits is subsequently allocated to represent the polarization tensor field. The entries of $\vec{\tau}$ are encoded into the amplitudes of the $\mathrm{N}^{\text{qb-Pol}}$-qubit in the superposition states, with amplitudes τ_q and computational basis states $|q\rangle$, yielding $|\vec{\tau}\rangle = \sum_{q=0}^{2^{\mathrm{N}^{\text{qb-Pol}}}-1} \tau_q |q\rangle$.

With the polarization tensor field prepared, the algorithm proceeds to step (4) *Quantum primitive*. In this step, the quantum circuit implementing the quantum Fourier transform (see Appendix C) is constructed and applied to the quantum state that encodes the polarization field. The number of qubits required to represent the discretized spatial domain is set as $\mathrm{N}^{\text{qb-qft}} = \left\lceil \log_2\left(\mathrm{N}^{\mathrm{tot}}\right)\right\rceil$. The QFT circuit is then applied to transfer the polarization field to Fourier space, $|\widehat{\vec{\tau}}\rangle = \mathcal{QFT}\left(|\vec{\tau}\rangle\right)$. Once the Fourier-space representation is obtained, the transformed state is rearranged into tensor form, $\widehat{\underset{\sim}{\tau}} \in \mathbb{H}^{3\times3\times\mathrm{N}^{\mathrm{tot}}}$. The tensor field is subsequently double-contracted with the Green operator, $\widehat{\underset{\approx}{\mathrm{G}}}$, and assigned to the displacement gradient tensor field in Fourier space, $\widehat{\nabla \underset{\sim}{u}}$, including the treatment of the zero-frequency mode (such as $\underline{\xi} = \underline{0}$).

Finally, step (5) *Output and measurement* consists of applying the IQFT circuit (see Appendix C) to return the displacement gradient tensor field to real space, followed by rescaling with the norm of the polarization tensor field used prior to superposition, such that $\nabla \underset{\sim}{u} = \overline{\nabla \underset{\sim}{u}} + \|\underset{\sim}{\tau}\| \, \mathcal{IQFT}\left(\widehat{\nabla \underset{\sim}{u}}\right)$. The complete QFT-method algorithm for the CCP framework is provided in Algorithm 1.

2.5.2. Classical MicroCurl strain gradient crystal plasticity model: QFT-method implementation

In the CMCurl model, once the Cauchy equilibrium equation has been solved to the prescribed accuracy, an additional balance equation must be satisfied. Accordingly, step (1) *Problem setting* consists of specifying the CMCurl nonlocal field equation, Eq. (15). In step (2) *Discretization*, the discretization is inherited from the solution procedure for the Cauchy equilibrium equation; details are provided in Section 2.5.1. Briefly, the periodic microstructure is discretized on a uniform grid with $\mathrm{N}^{\mathrm{tot}} = \mathrm{N}^3$ voxels.

Step (3) *State preparation* provides a quantum representation (see Appendix B) of the plastic distortion tensor field within the quantum register. The plastic distortion tensor, $\underset{\sim}{\mathrm{H}}^p = \left(\nabla \underset{\sim}{u}\right)^p \in \mathbb{R}^{3\times3\times\mathrm{N}^{\mathrm{tot}}}$, is first rearranged and normalized into a vector form,

Algorithm 1 End-to-End QFT-method workflow in the classical crystal plasticity framework.

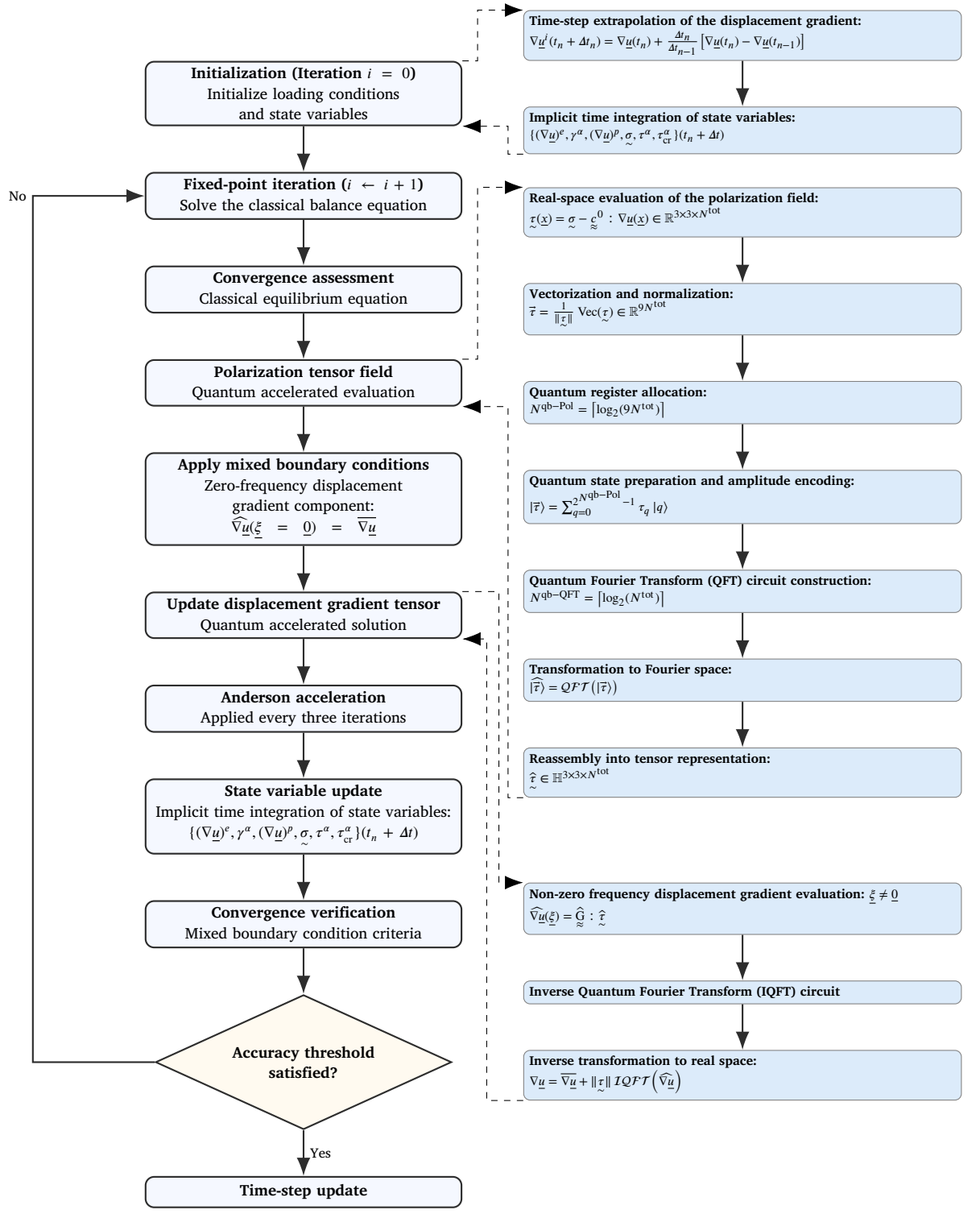

$\overrightarrow{\mathrm{H}^p} = \frac{1}{\|\underset{\sim}{\mathrm{H}^p}\|}\mathrm{Vec}\left(\underset{\sim}{\mathrm{H}^p}\right) \in \mathbb{R}^{9\mathrm{N}^{\mathrm{tot}}}$. A quantum register with $\mathrm{N}^{\mathrm{qb}} = \lceil \log_2(9 \times \mathrm{N}^{\mathrm{tot}}) \rceil$ qubits is then initialized in the zero state, and the normalized plastic distortion vector is encoded into the amplitudes of the corresponding qubits, $|\overrightarrow{\mathrm{H}^p}\rangle = \sum_{q=0}^{2^{\mathrm{N}^{\mathrm{qb}}}-1} \mathrm{H}^p_q |q\rangle$.

The subsequent step (4) *Quantum primitive* applies the QFT circuit (see Appendix C) to transform the encoded field to Fourier space, $|\widehat{\overrightarrow{\mathrm{H}^{p}}}\rangle = \mathcal{QFT}\left(|\overrightarrow{\mathrm{H}^{p}}\rangle\right)$. The resulting amplitudes are then rearranged back into the tensor representation, $\widehat{\underset{\sim}{\mathrm{H}}^{P}} = \mathrm{Ten}\left(|\widehat{\overrightarrow{\mathrm{H}^{p}}}\rangle\right) \in \mathbb{H}^{3\times3\times\mathrm{N}^{\mathrm{tot}}}$. Depending on the selected MicroCurl nonlocal field equation — i.e., Eq. (14) or Eq. (15) — the Fourier-domain representation of the double-curl operator and the associated length-scale parameter are multiplied to obtain the micro-stress in Fourier space, $\widehat{\underset{\sim}{s}} = -\mathrm{A}\ \widehat{\mathrm{DCurl}}\ \widehat{\underset{\sim}{\mathrm{H}}^{P}}$. More details in Appendix C.3.

Finally, step (5) *Output and measurement* consists of applying the IQFT (see Appendix C) to return the micro-stress tensor in real space, $\underset{\sim}{s} = \|\mathrm{H}^{p}\|\ \mathcal{IQFT}\left(\widehat{\underset{\sim}{s}}\right)$. The resulting micro-stress is then used to evaluate the back-stress required in the shear flow rule.

2.5.3. Classical MicroSlip strain gradient crystal plasticity model: QFT-method implementation

In the CMSlip model, the QFT-method workflow is initiated by step (1) *Problem setting*, which consists of specifying the nonlocal field equation, Eq. (21). Step (2) *Discretization* follows the same spatial discretization employed for the solution of the Cauchy equilibrium equation. In the subsequent steps, the procedure is carried out independently for each slip system.

Step (3) *State preparation* provides the quantum representation of the cumulative shear strain associated to each slip system within the quantum register (see Appendix B). For a given slip system α, the cumulative shear strain field satisfies $\gamma^{\alpha}_{\mathrm{cum}} \in \mathbb{R}^{\mathrm{N}^{\mathrm{tot}}}$; therefore, no additional vectorization is required. However, the field is normalized as $\overrightarrow{\gamma^{\alpha}_{\mathrm{cum}}} = \frac{1}{\|\gamma^{\alpha}_{\mathrm{cum}}\|}\gamma^{\alpha}_{\mathrm{cum}}$. A quantum register with $\mathrm{N}^{\mathrm{qb}} = \lceil \log_2(\mathrm{N}^{\mathrm{tot}}) \rceil$ qubits is then initialized in the zero state, and the normalized cumulative shear strain is encoded into the amplitudes of the corresponding superposition state, $|\overrightarrow{\gamma^{\alpha}_{\mathrm{cum}}}\rangle = \sum_{q=0}^{2^{\mathrm{N}^{\mathrm{qb}}}-1} \gamma^{\alpha}_{\mathrm{cum},q}|q\rangle$.

Step (4) *Quantum primitive* applies the QFT circuit (see Appendix B) to transfer the encoded field to Fourier space, $|\widehat{\overrightarrow{\gamma^{\alpha}_{\mathrm{cum}}}}\rangle = \mathcal{QFT}\left(|\overrightarrow{\gamma^{\alpha}_{\mathrm{cum}}}\rangle\right)$. In accordance with the nonlocal field equation, Eq. (21), the Fourier-domain representation of the Laplacian operator (see Appendix C.3) and the associated length-scale factor are then applied multiplicatively to obtain the higher-order stress in Fourier space, $\widehat{\chi^{\alpha}} = A\ \widehat{\mathrm{Lap}}\ |\widehat{\overrightarrow{\gamma^{\alpha}_{\mathrm{cum}}}}\rangle$.

Finally, step (5) *Output and measurement* consists of applying the IQFT (see Appendix B) to return the higher-order stress in real space, $\chi^{\alpha} = \|\gamma^{\alpha}_{\mathrm{cum}}\|\ \mathcal{IQFT}\left(\widehat{\chi^{\alpha}}\right)$.

2.5.4. Enhanced MicroCurl strain gradient crystal plasticity model: QFT-method implementation

In the EMCurl model, the quantum-computing procedure for evaluating the differential operators associated with the state variables closely follows the implementations described in Sections 2.5.2 and 2.5.3. Therefore, only the additional steps specific to the enhanced model are outlined here. In particular, the higher-order modulus is first evaluated in real space according to Eq. (29). The corresponding quantum algorithm is then applied to transfer this field to Fourier space, $\widehat{A^{\alpha}} = \mathcal{QFT}\left(|\overrightarrow{A^{\alpha}}\rangle\right)$, and to compute its gradient via $\nabla A^{\alpha} = \|A^{\alpha}\|\ \ \mathcal{IQFT}\left(\widehat{\mathrm{Grad}}\widehat{A^{\alpha}}\right)$. An analogous procedure is employed to evaluate the curl and double-curl operators acting on the plastic distortion tensor.

Based on these quantities, the micro-stress tensor is subsequently computed using Eqs. (25) and (26), followed by the evaluation of the back-stress according to Eq. (16) and the generalized back-stress associated with each slip system given by Eq. (27). A complete description of the QFT-method algorithm for the EMCurl model is provided in Algorithm 2.

2.5.5. Enhanced MicroSlip strain gradient crystal plasticity model: QFT-method implementation

Similar to Sections 2.5.3 and 2.5.4, the EMSlip formulation requires the solution of a nonlocal field equation. This procedure involves evaluating the gradient of the higher-order modulus as well as the gradient and Laplacian of the cumulative shear strain associated with each slip system. The corresponding differential operators are computed within the proposed QFT-method workflow following the same state-preparation, QFT/IQFT, and Fourier-domain operator-application strategy described previously. A complete QFT-method algorithm for the EMSlip model is provided in Algorithm 3.

Validation of the proposed QFT-method algorithms within the CCP framework and the SGCP models is presented in Appendix D. A range of representative material responses is considered to assess both accuracy and robustness. First, linear elasticity is examined using a two-layer laminate with different elastic properties. The numerical solution obtained with the proposed QFT-method is compared against the corresponding FFT-method solution, showing excellent agreement. Second, a single crystal under simple shear is analyzed for three constitutive material behaviors—linear hardening, perfect plasticity, and linear softening. In these cases, the QFT-method results are validated by direct comparison with the analytical solutions reported in Lame Jouybari et al. (2024). Finally, a nonlinear softening behavior is considered for a single crystal subjected to simple shear, and the QFT-method results are benchmarked against the analytical solution proposed by Lame Jouybari et al. (2025). Collectively, these test cases demonstrate that the proposed QFT approach reproduces established numerical and analytical references across elastic, plastic, and softening behaviors.

3. Results

This section reports numerical results obtained for periodic two- and three-dimensional polycrystalline aggregates generated by Voronoi tessellation with randomly oriented grains (Quey et al., 2011). The microstructures are discretized at high resolution, enabling a detailed assessment of localized deformation and microstructural fields. All simulations are performed under uniaxial tensile loading at a relatively low applied strain rate of 10^{-6} s^{-1} in order to promote quasi-static response and to resolve the

Algorithm 2 End-to-End QFT-method workflow in the Enhanced MicroCurl-SGCP model.

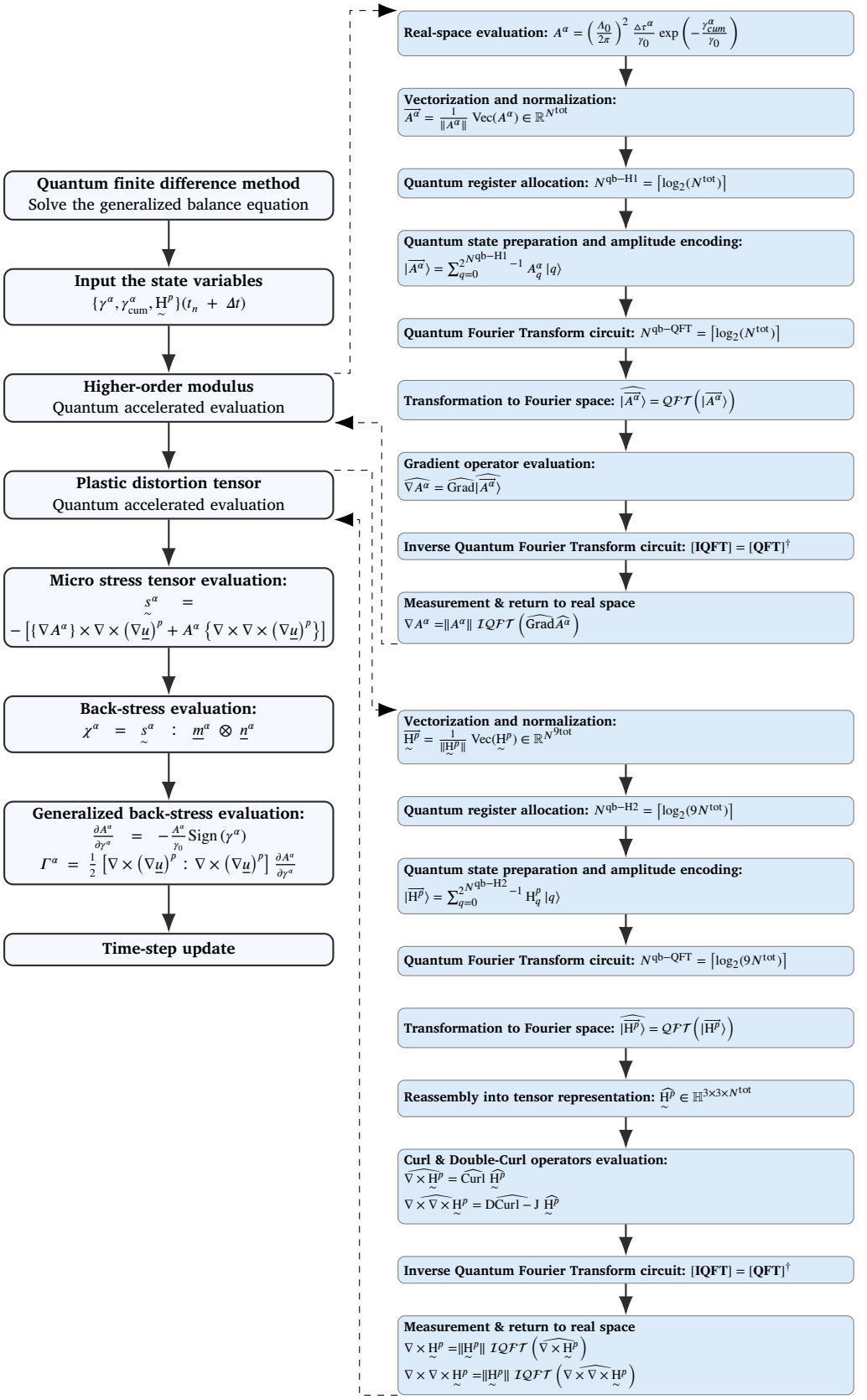

Algorithm 3 End-to-End QFT-method workflow in the Enhanced MicroSlip-SGCP model.

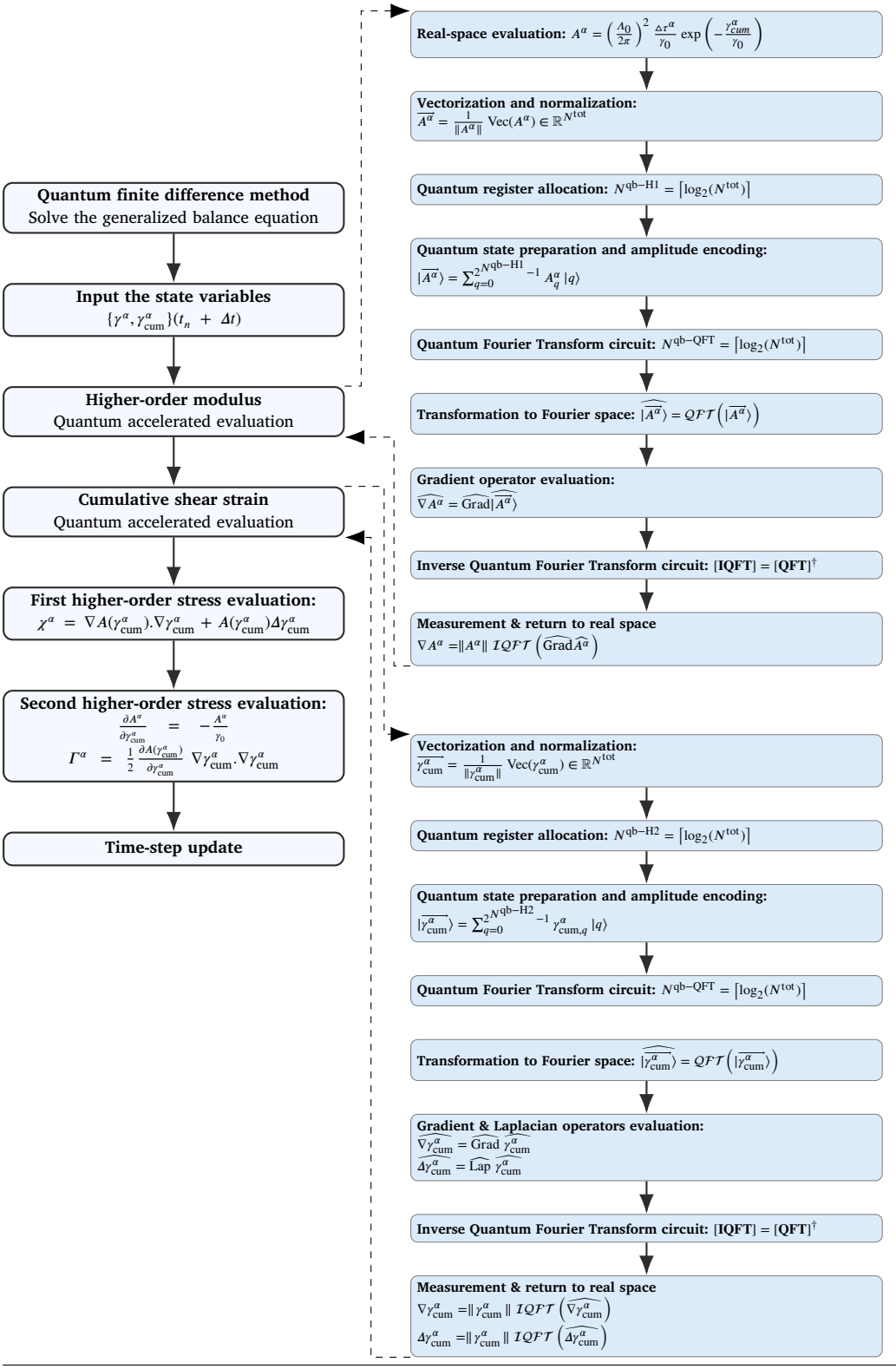

Table 1
Material parameters of the polycrystalline aggregates.

	E	ν	K	n	τ_0	$\Delta\tau$	γ_0	H
Two-dimensional aggregate	100 GPa	0.3	10 MPa s^{-n}	15	100 MPa	50 MPa	0.05	0 MPa
Three-dimensional aggregate	100 GPa	0.3	10 MPa s^{-n}	15	100 MPa	50 MPa	0.10	0 MPa

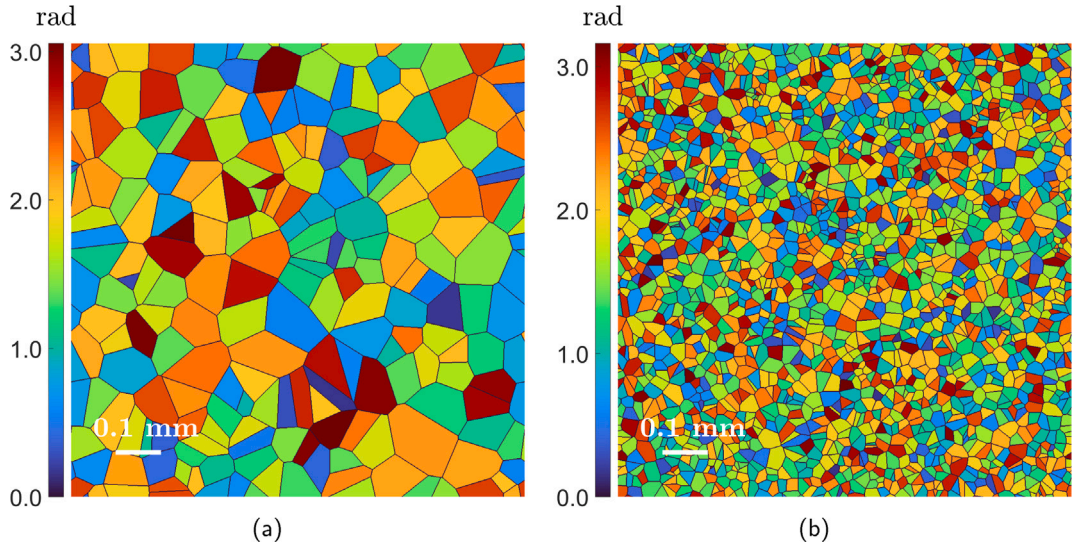

Fig. 2. Microstructures of the two-dimensional polycrystalline aggregate composed of (a) 200 columnar grains (b) 2000 columnar grains. Colors indicate grain orientation relative to the loading direction; black lines are grain boundary voxels.

progressive development of strain localization mechanisms. Furthermore, the MicroContinuity higher-order condition is considered for all polycrystalline aggregate simulations.

The primary aim of this section is to demonstrate the proposed QFT-method as a computational tool for simulating polycrystalline aggregates and for investigating the predictive capabilities of the CSGCP and ESGCP theories within this setting, with particular emphasis on the formation of shear bands (or clear channels) and the evolution of microscopic state variables. In addition, the influence of mean grain size is examined within both the CSGCP and ESGCP frameworks. For the enhanced models, the evolution of the deformation-dependent length scale (higher-order modulus) is analyzed throughout loading. Finally, the evolution of the higher-order stresses associated with each SGCP model is examined in detail during the loading.

3.1. Two-dimensional aggregate

Initially, two-dimensional microstructure is considered to enable a direct comparison of the characteristic responses predicted by different SGCP models and by their corresponding QFT-method implementations introduced in Section 2.5. The microstructure is statistically isotropic polycrystalline aggregate composed of equiaxed grains with random orientations which each grain is assigned a random crystallographic orientation described by Euler angles, resulting in an overall texture-free (isotropic) aggregate. The geometry is then discretized into a regular cubic voxel grid (Quey et al., 2011). Accordingly, the periodic two-dimensional polycrystalline aggregate shown in Fig. 2(a) with total area 1 mm^2 is generated and consists of 200 grains with an approximately mean grain size of GS = 0.07 mm. Each grain is equipped with an in-plane (planar) slip system which is rotated by the grain orientation. The microstructure is discretized on a regular grid of 1024^2 voxels (approximately one million voxels), providing sufficient spatial resolution to capture localization phenomena and microstructural field variations. The aggregate is subjected to uniaxial tensile loading at a low strain rate[5] of 10^{-6} s^{-1}, a final deformation amplitude of $\nabla u_{yy} = 0.02$ is prescribed, and the MicroContinuity higher-order interface condition on the grain boundary is considered.[6] The material parameters are taken to be identical to those in Table 1 which is calibrated for the irradiated stainless steels in Lame Jouybari et al. (2024). Furthermore, the set of SGCP models introduced in Sections 2.2 and 2.3 is employed here. To ensure a meaningful comparison between the CSGCP and

[5] This low strain rate of loading is required in the SGCP models due to the explicit coupling between the classical balance equation and the nonlocal field equation in the proposed algorithm.

[6] The MicroContinuity condition ensures continuity of the higher-order traction tensor in each SGCP models across both sides of the grain boundary. Further details are provided in Lame Jouybari et al. (2024, 2025).

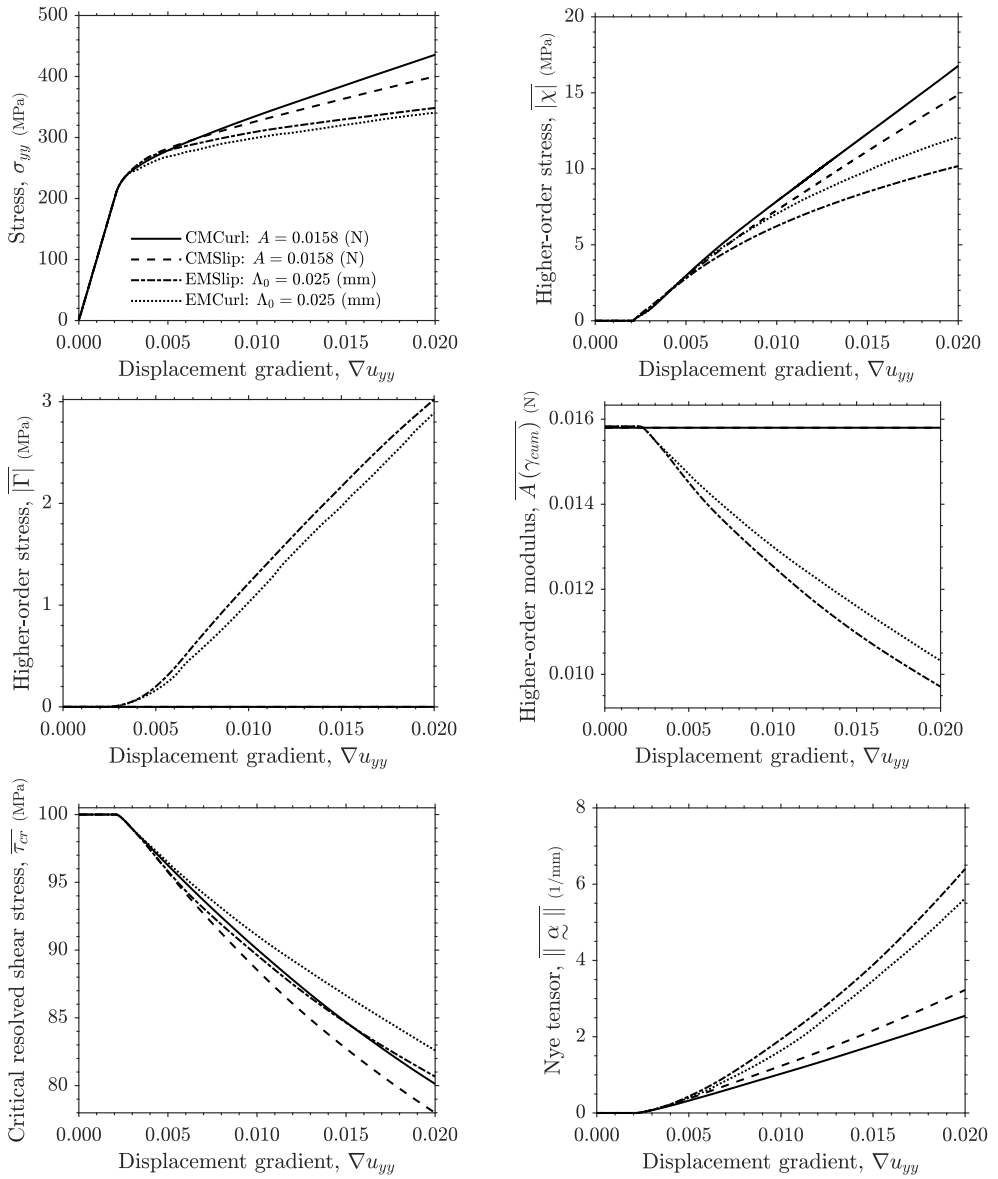

Fig. 3. Evolution of the spatially averaged state variables for the microstructure shown in Fig. 2(a) under applied loading. Results are shown for the CMSlip and CMCurl models with length scale $A = 0.0158\,\mathrm{N}$, and for the EMSlip and EMCurl models with length scale $\Lambda_0 = 0.025\,\mathrm{mm}$.

ESGCP theories, the initial length scale in the ESGCP theory is set to $\Lambda_0 = 0.025$ mm. The corresponding fixed nonlocal parameter for the CSGCP theory is then obtained via Eq. (29), yielding $A = 0.0158$ N.

In all simulations, the proposed QFT-method introduced in Section 2.5 is employed. The classical balance equation is solved following the procedure described in Section 2.5.1. For the amplitude encoding (state preparation) of the polarization tensor field, a quantum register with $N^{qb\text{-}Pol} = 24$ qubits is used. The mapping to Fourier space is performed using a QFT2D circuit acting on a register of $N^{qb\text{-}qft} = 20$ qubits.

For the nonlocal field equation in the CMCurl model, a quantum register with $N^{qb\text{-}H} = 24$ qubits is allocated for the amplitude encoding of the plastic distortion tensor. In the CMSlip model, a register of $N^{qb\text{-}H} = 20$ qubits is used to encode the cumulative shear strain. For the EMCurl model, two quantum registers are employed to evaluate the nonlocal field equation: the first is associated with the higher-order modulus and contains $N^{qb\text{-}H1} = 20$ qubits, while the second encodes the plastic distortion tensor using $N^{qb\text{-}H2} = 24$ qubits. Finally, for the EMSlip model, two quantum registers are likewise assigned, with $N^{qb\text{-}H1} = 20$ qubits representing the higher-order modulus and $N^{qb\text{-}H2} = 20$ qubits representing the cumulative shear strain associated to each slip system.

Fig. 3 illustrates the evolution of representative state variables during loading for different SGCP models. The corresponding macroscopic stress–strain responses indicate that all models initially exhibit linear elastic behavior and, upon reaching the

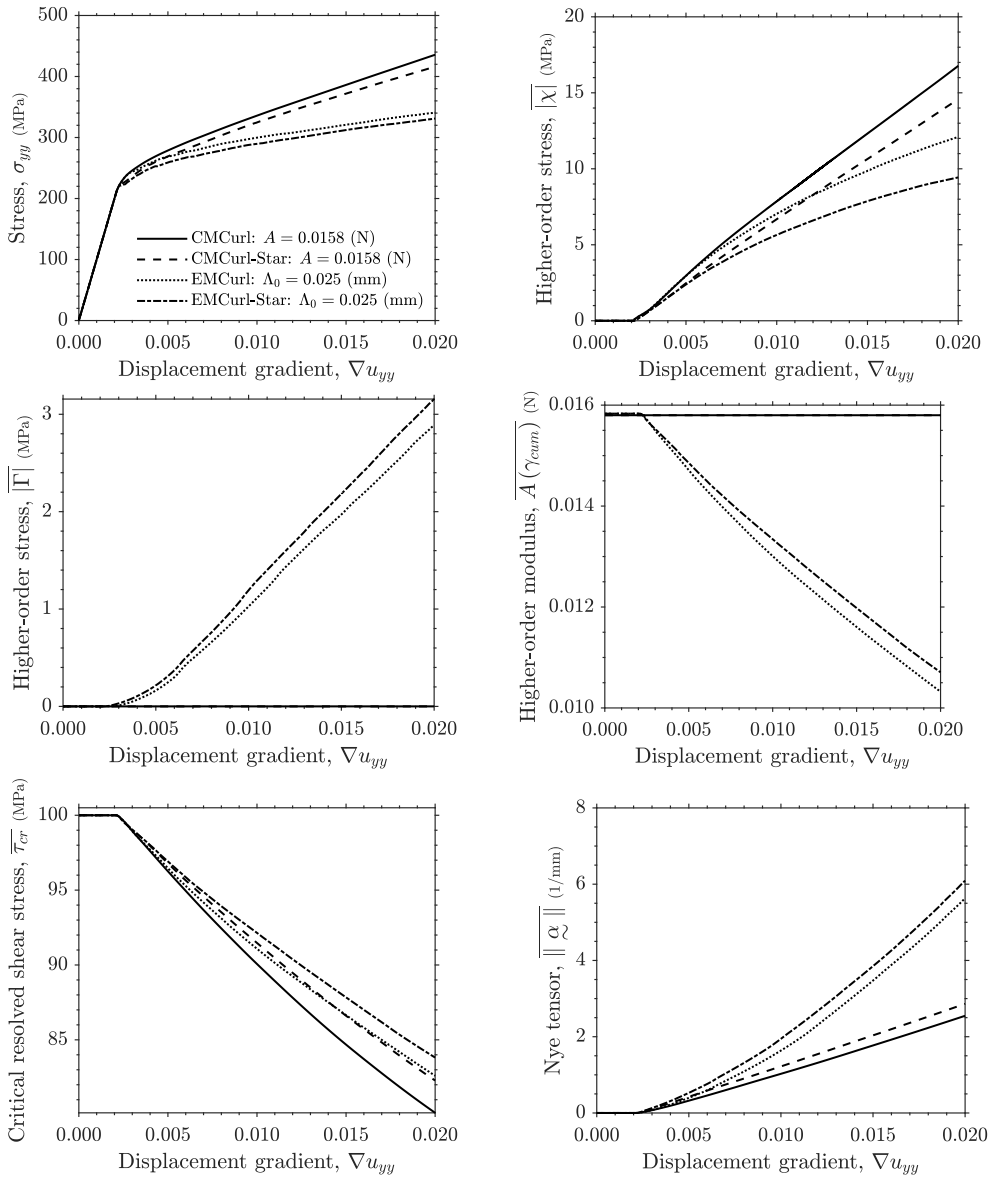

Fig. 4. Evolution of the spatially averaged state variables for the microstructure shown in Fig. 2(a) under applied loading. Results are shown for the CMCurl and CMCurl-Star models with length scale $A = 0.0158, \mathrm{N}$, and for the EMCurl and EMCurl-Star models with length scale $\Lambda_0 = 0.025, \mathrm{mm}$. The model variants differ in the evaluation of the double-curl operator within the micro-stress tensor, Eq. (13), in Fourier space.

macroscopic yield stress, reproduce a subsequent hardening regime. A clear distinction is observed between the classical and enhanced models. In the ESGCP models (MicroCurl and MicroSlip), the macroscopic hardening rate is reduced, whereas in the Classical SGCP models (MicroCurl and MicroSlip) the macroscopic hardening response increases monotonically. This trend is interpreted in terms of the evolution of higher-order stresses (or back-stresses). Specifically, after the onset of plasticity, the rate of increase of the higher-order stresses decreases in the Enhanced SGCP models, while it continues to increase in the Classical SGCP models.

The reduction of the higher-order stress rate in the Enhanced SGCP models is directly associated with the incorporation of local softening mechanisms by the reduction of the critical resolved shear stress and, consequently, the effective strength of the crystal. In the enhanced models, this softening is accompanied by a corresponding reduction of the higher-order modulus, whereas in the classical SGCP formulations the higher-order modulus (nonlocal parameter) remains fixed throughout deformation. As a result, the enhanced models exhibit a progressive attenuation of higher-order modulus in the plastic regime, consistent with the observed macroscopic and microscopic behaviors. Although the critical resolved shear stress decreases in all models, the macroscopic stress–strain curves still exhibit overall hardening. This is attributed to the planar analysis of the two-dimensional microstructure, where

plastic deformation and subsequent localization are formed to the narrow bands, while the remaining regions of the grains remain elastic. As a result, the elastic response dominates in a volume-averaged than the local softening within the bands.

Fig. 4 compares the evolution of state variables when two different mathematical operators, Eqs. (C.32) and (C.33), are employed to solve the nonlocal field equations for the CMCurl and CMCurl-Star models, Eqs. (14) and (15), and for the EMCurl-Star and EMCurl models, Eqs. (25) and (26). The macroscopic responses indicate that the DCurl-S operator produces a lower level of hardening behavior, which is consistent with the reduced magnitude of the resulting back-stresses. As shown in Appendix E, the DCurl-J operator (Eq. (C.33)) slightly affects the slip bands, whereas the DCurl-S operator (Eq. (C.32)) does not influence slip band and instead through kink-band formation. Consequently, the CMCurl and EMCurl models employing the DCurl-J operator exhibit a larger volume fraction of activated plastic deformation than the corresponding CMCurl-Star and EMCurl-Star models using the DCurl-S operator. This broader plastic activation leads to a stronger reduction of both the higher-order modulus and the critical resolved shear stress compared with the DCurl-S-based formulations.

Fig. 5 presents the spatial distributions of the plastic distortion tensor norm and the rotation field[7] at the final loading, $\nabla u_{yy} = 0.02$, for the SGCP models. It is observed that all SGCP formulations reproduce localized deformation in the form of slip and kink bands, with kink bands being consistently accompanied by finite rotation fields. Distinct regularization characteristics are obtained for the different SGCP models. In the CMSlip and EMSlip models, both slip and kink bands are regularized, whereas in the CMCurl and EMCurl models the regularization is expressed primarily through the rotation field within kink bands, and to appear as bundles of closely spaced slip bands. A further qualitative difference is observed between the classical and enhanced theories. In the CSGCP (MicroSlip and MicroCurl) models, the localized bands progressively widen, extend toward grain boundaries, and exhibit reduced localization intensity at the final loading stage. In contrast, in the ESGCP (MicroSlip and MicroCurl) models the band widths remain stable and consistent with the prescribed length scale $\Lambda_0 = 0.025$ mm. For instance, in the EMSlip model both slip and kink bands are regularized to a characteristic width comparable to $\Lambda_0 = 0.025$ mm, while in the EMCurl model, the kink bands are transferred to the bundle of slip bands by the characteristic length approximately equal to the $\Lambda_0 = 0.025$ mm.

Fig. 6 shows the corresponding distributions of the plastic distortion norm and rotation field obtained with the CMCurl-Star and EMCurl-Star models employing the DCurl-S operator which is introduced based on the Eq. (C.32) in Appendix C.3. The results indicate that, similar to the CMCurl and EMCurl models using the DCurl-J operator, the DCurl-S-based operator within the CMCurl-Star and EMCurl-Star models primarily affect kink-band patterns. In these models, slip bands remain totally unregularized and uninfluenced; by contrast, in the CMCurl and EMCurl models the slip bands are weakly affected and exhibit a slightly increased width. Moreover, in the CMCurl-Star model, the transferred slip bands extend to grain boundaries, whereas in the EMCurl-Star model these transformed bands remain under controlled and closely equal the prescribed length scale $\Lambda_0 = 0.025$ mm.

The simulations were also performed using the FFT-based method proposed by Lame Jouybari et al. (2024, 2025). The two methods yield identical results in terms of the macroscopic evolution of the state variables, as well as the distributions of the norm of the plastic distortion tensor and the rotation field.[8] This agreement provides an additional verification of the numerical implementation and confirms the consistency of the proposed QFT-method with established FFT-method.

3.2. Mean-grain size effect

The second polycrystalline aggregate in Fig. 2(b) is analyzed to investigate mean-grain size effect in the CSGCP and ESGCP theories. This microstructure contains 2000 grains within a $1\,\text{mm}^2$ domain, yielding a two–dimensional mean grain size of GS = $0.0223\,\text{mm}$ (see Fig. 2). For comparison, results are also generated for the coarser-grains microstructure illustrated in Fig. 2(a). Material properties, higher-order interface condition on the grain boundaries, spatial resolution, and tensile loading conditions are identical to those adopted in Section 3.1. The internal length-scale parameters are chosen as follows:

- Classical SGCP theory: $A = 0.0101\,\text{N}$,
- Enhanced SGCP theory: $\Lambda_0 = 0.02\,\text{mm}$.

These settings permit a direct comparison of mean-grain size effect between the CSGCP and ESGCP theories under otherwise identical conditions.

Grain–size effect. Both theories reproduce the well-known Hall–Petch trend, Figs. 7 and 8: the finer microstructure is stronger and displays a higher work-hardening rate. The additional hardening is traced to a larger back-stress χ arising in the fine aggregate. Consistently, the Nye-tensor norm $\overline{\|\alpha\|}$ grows more rapidly for the smaller grains, indicating a higher density of GNDs. The associated decrease in the average critical resolved shear stress $\overline{\tau_{\text{cr}}}$ reveals that softening over volume is more pronounced in the fine microstructure.

[7] The rotation field is the norm of the axial vector of the skew-symmetric part of the elastic part of the displacement gradient tensor, $\underline{\omega} = \frac{1}{2}\underline{\underline{e}} : \text{Skew}(\nabla \underline{u}^e)$. More details in the Appendix B of Lame Jouybari et al. (2025).

[8] The differences between the distributions obtained using the FFT and QFT methods are negligible and do not affect the overall localization patterns within the microstructure or the typical effects of the different SGCP models.

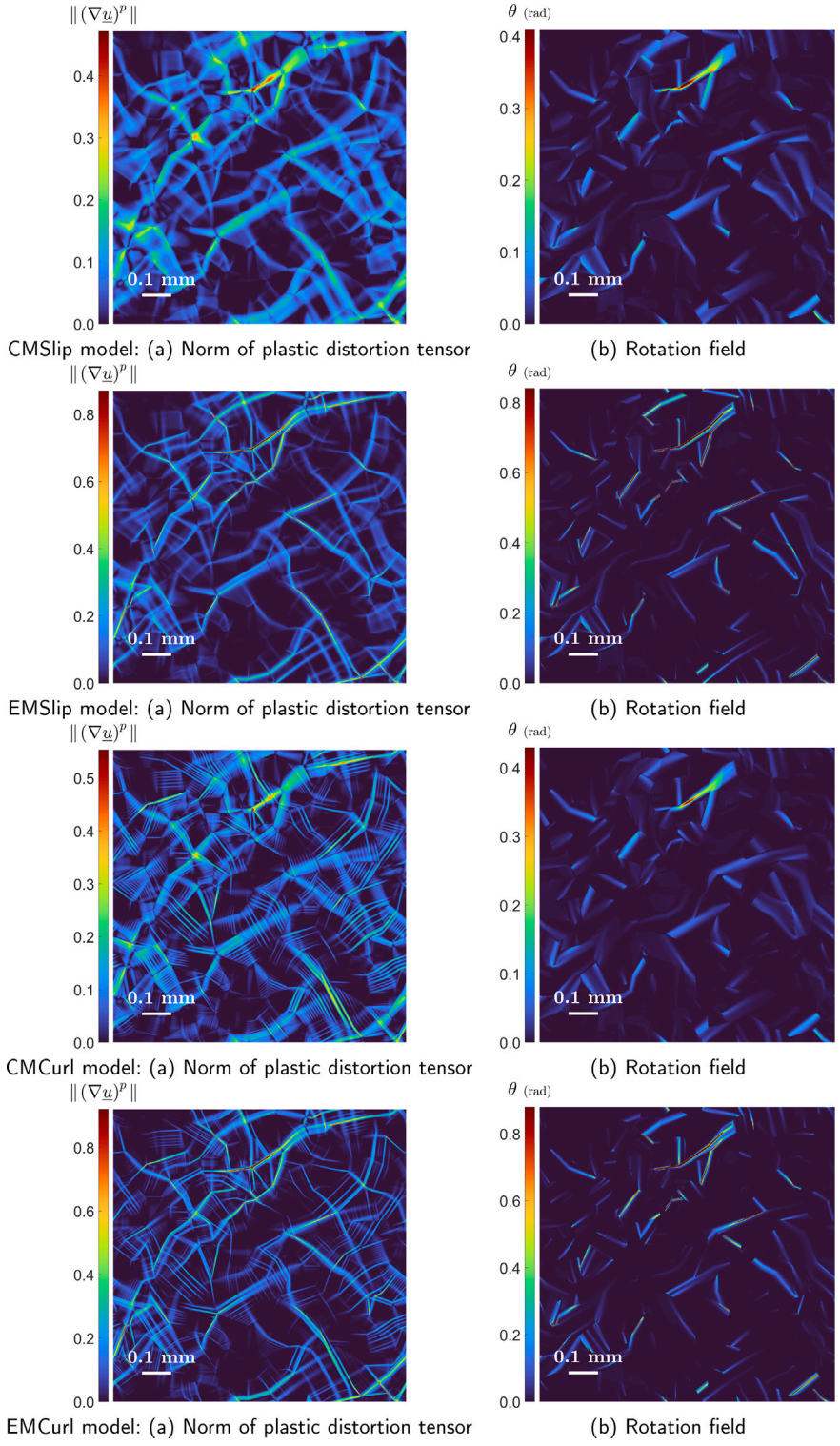

Fig. 5. Distributions of the norm of the plastic distortion tensor, $\| (\nabla \underline{u})^p \|$, and the rotation field, θ, in the two-dimensional microstructure shown in Fig. 2(a), at final stage of the deformation $\nabla u_{yy} = 0.02$, obtained from the CMSlip and CMCurl models with the $A = 0.0158\ N$ and EMSlip and EMCurl models with the $\Lambda_0 = 0.025$ mm.

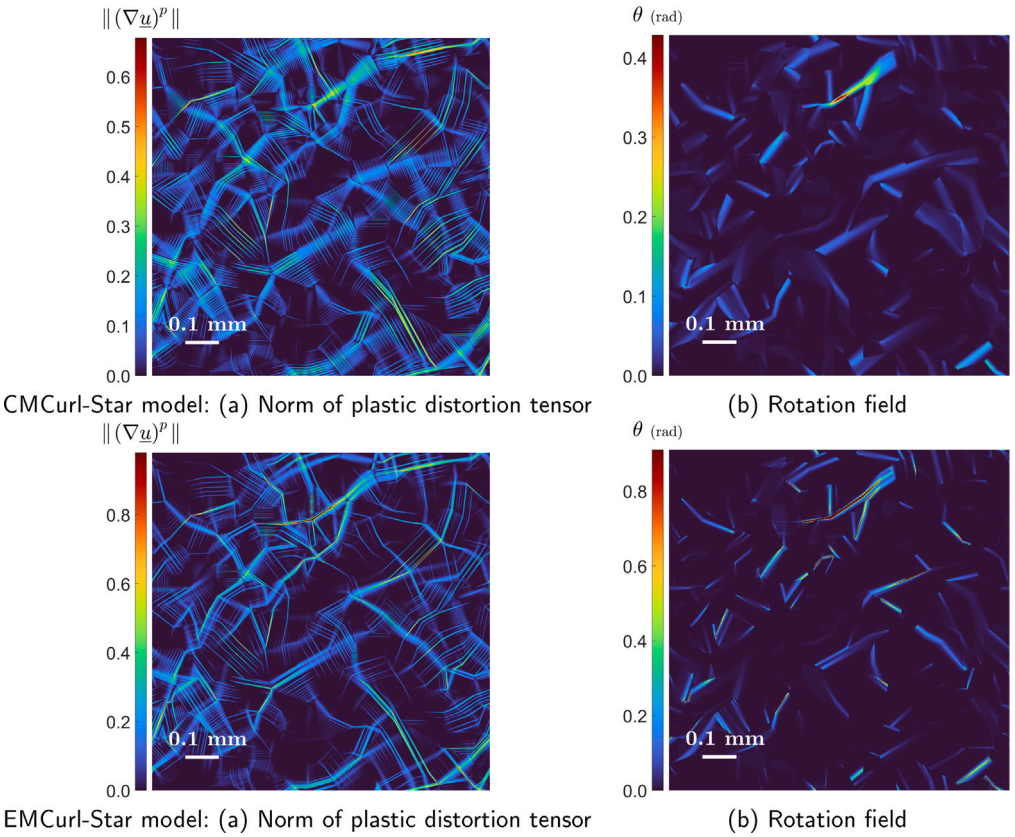

Fig. 6. Distributions of the norm of the plastic distortion tensor, $\| (\nabla \underline{u})^p \|$, and the rotation field, θ, in the two-dimensional microstructure shown in Fig. 2(a), at final stage of the deformation $\nabla u_{yy} = 0.02$, obtained from the CMCurl-Star model with the $A = 0.0158\ N$ and EMCurl-Star model with the $\Lambda_0 = 0.025$ mm.

Classical versus enhanced SGCP models. In the classical models, Figs. 7 and 8, the stress–strain curves for the two microstructures diverge progressively with applied loading, because the constant length scale A enforces a persistent increase in back-stress that suppresses GND multiplication. By contrast, the EMCurl and EMSlip models introduce a deformation-dependent higher-order modulus $A(\gamma_{\text{cum}})$. As plastic deformation proceeds, $A(\gamma_{\text{cum}})$ reduces faster in the fine aggregate than in the coarse one. This accelerates early hardening but soon saturates the back-stress, allowing GND accumulation to resume. Consequently, the initial separation between the two stress–strain curves is large, yet the curves converge at higher deformations—an effect absent from the classical models. The ESGCP theory therefore captures a realistic transition from Hall–Petch-dominated hardening to saturation at larger level of loading, reflecting the evolving microstructural state.

3.3. Three-dimensional aggregate

In this section, a three-dimensional periodic Voronoi tessellation is used to generate a polycrystalline aggregate with a total volume of 1 mm^3, consisting of 125 randomly oriented FCC grains, and totally texture-free (isotropic) aggregate. Each grain has up to 12 crystallographic slip systems for dislocation glide, defined by $\{111\}\langle 110\rangle$. The slip systems are specified in the reference configuration and rotated according to the crystallographic orientation of each grain. The aggregate has a mean grain size on the order of GS = 0.2 mm and is discretized on a regular 256^3 voxel grid, corresponding to approximately 1.68×10^7 voxels. The aggregate is subjected to uniaxial tensile loading along the z-direction, with a prescribed final strain component $\nabla u_{zz} = 0.01$ applied at a low strain rate of 10^{-6} s^{-1}. This loading configuration, together with periodic boundary conditions, enables a direct assessment of the heterogeneous intragranular and intergranular responses under quasi-static tension. Furthermore, the MicroContinuity higher-order interface condition is considered on the grain boundaries.

The numerical analysis includes the CCP framework ($\Lambda_0 = 0$ mm) as well as the EMSlip and EMCurl-Star models, for which the initial length scale of $\Lambda_0 = 0.075$ mm is chosen. The material parameters are identical to those[9] in Table 1.

[9] In three-dimensional simulations, γ_0 is doubled and the loading is half relative to the two-dimensional simulations to mitigate numerical instabilities from macroscopic softening in the CCP framework.

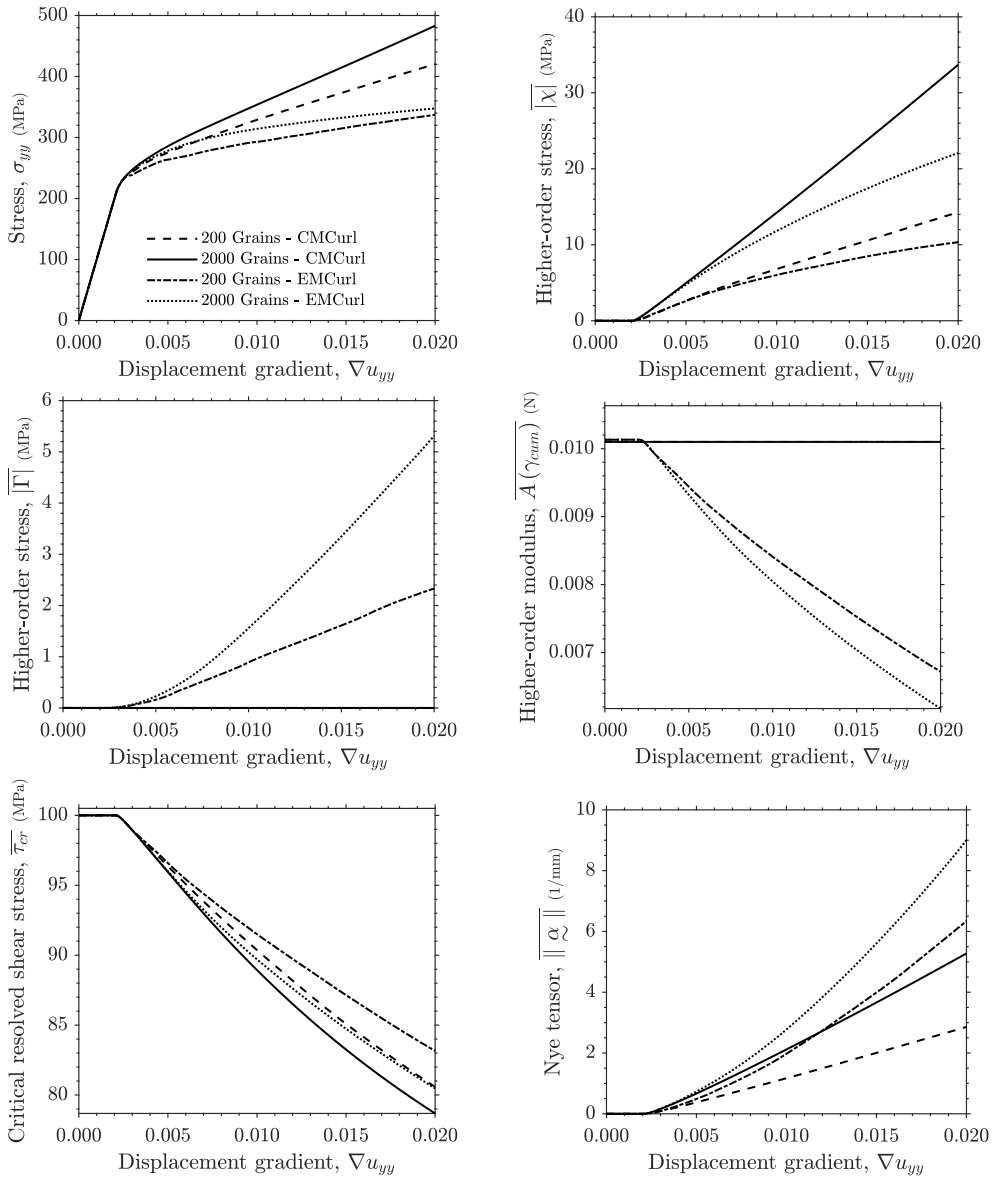

Fig. 7. Evolution of the spatially averaged state variables for the microstructures shown in Fig. 2 during applied loading. Results are obtained from the CMCurl model with the length scale $A = 0.0101$ N, and the EMCurl model with the length scale $\Lambda_0 = 0.02$ mm.

In all simulations presented in this section, the proposed QFT-method introduced in Section 2.5 is employed. To construct the QFT3D circuit corresponding to the discretized geometry, a quantum register with $N^{qb\text{-}qft} = 24$ qubits is used. For the solution of the classical balance equation and for the amplitude encoding (state preparation) of the polarization tensor field, a quantum register with $N^{qb\text{-}Pol} = 28$ qubits is assigned. For the EMCurl-Star model, the higher-order modulus associated with each slip system, A^{α}, is encoded independently for each slip system using a quantum register of $N^{qb\text{-}H1} = 24$ qubits, while the plastic distortion tensor is encoded using a register of $N^{qb\text{-}H2} = 28$ qubits. Similarly, for the EMSlip model, the higher-order modulus A^{α} is encoded independently for each slip system on a register with $N^{qb\text{-}H1} = 24$ qubits, and the cumulative shear strain associated with each slip system is encoded independently on a register with $N^{qb\text{-}H2} = 24$ qubits.

Fig. 10 presents the evolution of selected state variables during deformation for the CCP framework and for the EMSlip and EMCurl-Star models. The macroscopic stress–strain responses coincide in the elastic regime; however, clear differences emerge after the macroscopic yield stress and the onset of plastic flow. In particular, macroscopic softening is observed in the CCP framework and in the EMCurl-Star model, whereas the EMSlip model exhibits the macroscopic hardening behavior. Consistent with the model definitions, the higher-order stresses vanish in the CCP framework ($\chi^{\alpha} = 0$ MPa and $\Gamma^{\alpha} = 0$ MPa), while they increase after the onset of plasticity in both the EMSlip and EMCurl-Star models. As the critical resolved shear stress decreases during deformation,

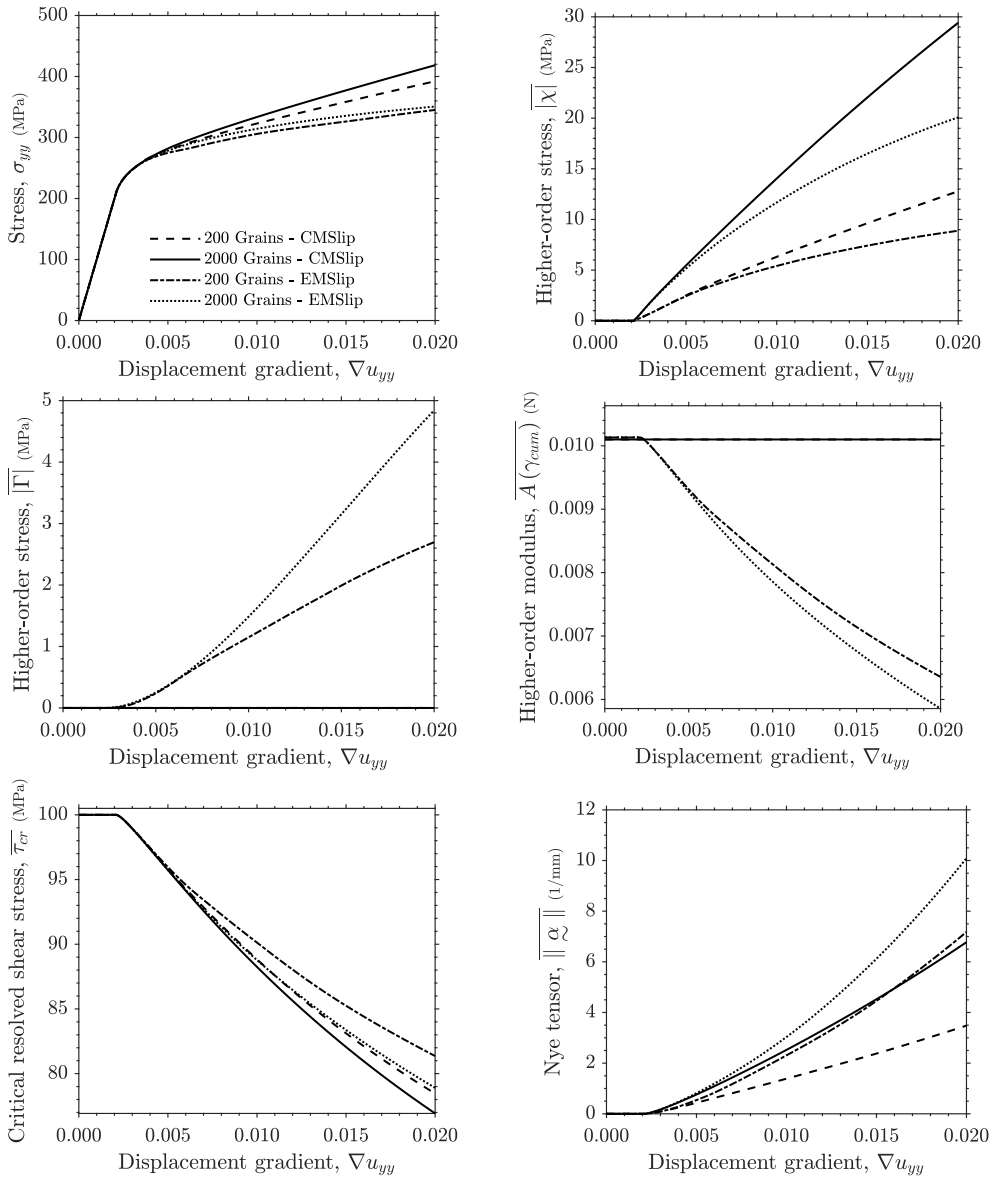

Fig. 8. Evolution of the spatially averaged state variables for the microstructures shown in Fig. 2 during applied loading. Results are obtained from the CMSlip model with the length scale $A = 0.0101$ N, and the EMSlip model with the length scale $\Lambda_0 = 0.02$ mm.

the higher-order modulus likewise decreases in these enhanced formulations, reflecting the coupling between softening behavior, microstructural sate and the higher-order modulus. The evolution of the Nye tensor further highlights the stabilizing role of the enhanced models. In the CCP framework, the Nye tensor increases sharply after plasticity initiates, which is consistent with the development of strong localization and the associated accumulation of lattice incompatibility. In contrast, the EMSlip and EMCurl-Star models exhibit a more moderate evolution of the Nye tensor, indicating reduced accumulation of GNDs, which is attributed to the presence and evolution of higher-order stresses.

Fig. 11 shows the spatial distributions of the norm of the plastic distortion tensor for the CCP framework and for the EMSlip and EMCurl-Star models. In the CCP framework, plastic deformation localizes into extremely narrow slip and kink bands with a width of only one to two voxels, and these bands can propagate across grain boundaries. In the EMSlip model, both slip and kink bands are regularized, while strong localization persists in regions where bands interact and intersect. By contrast, in the EMCurl-Star model the slip bands remain essentially unregularized and retain a one- to two-voxel width, similar to the CCP response, indicating that the corresponding back-stress and generalized back-stress contributions are negligible within these bands. Nevertheless, the original kink band from CCP framework are transformed into bundles of slip bands, demonstrating the ability of the proposed QFT-method to resolve detailed local-field features in large-scale three-dimensional simulations. It is worth noting that, in this three-dimensional

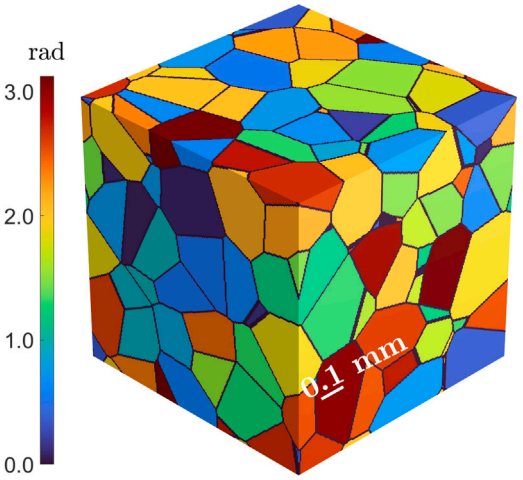

Fig. 9. Microstructure of the three-dimensional polycrystalline aggregate composed of 125 grains. The colors represent the orientation of the grains with respect to the loading direction and black lines correspond to the grain boundary voxels.

analysis with a microstructure resolution of approximately 17 million voxels, the proposed QFT method achieves significantly better overall simulation runtime compared to the FFT method due to less computational complexity given in Fig. C.3.

4. Conclusions

In this study, a new branch of the Enhanced Strain Gradient Crystal Plasticity (ESGCP) theory is introduced in the form of the EMSlip model, which incorporates a quadratic energetic contribution associated with the gradient of the cumulative shear strain on each slip system. Similar to the Nye tensor-based ESGCP formulation, the EMSlip model introduces a physically motivated length scale that is defined as a function of the evolving microstructural state of irradiated crystals. As a result, the model introduces first- and second-order higher-order stresses associated with each slip system in a thermodynamically consistent manner, derived directly from the gradient of the cumulative shear strain. It is further demonstrated that the EMSlip model regularizes both slip and kink bands to the prescribed length scale, thereby controlling the characteristic band width during deformation. In addition, it is shown that the EMCurl model only weakly influences slip band development under tensile loading due to the use of Laplacian and gradient–divergence operators in Fourier space. To address this limitation, a new EMCurl-Star SGCP model is proposed, in which the nonlocal field equation is solved using the frequency representation of the curl operator in Fourier space. This modification leaves slip bands essentially unaffected while promoting the transformation of kink bands into bundles of parallel (transferred) slip bands within the irradiated microstructure.

A major contribution of this work is the development of a quantum Fourier transform (QFT)-method as the computational framework within classical crystal plasticity, CSGCP, and ESGCP theories. The proposed QFT-method consists of four principal steps: (i) state preparation via amplitude encoding on an assigned quantum register, (ii) construction of the QFT circuit associated with that register, (iii) application of the relevant differential operators in Fourier space, and (iv) transformation back to real space using the inverse QFT (IQFT). This algorithm is first employed to solve the classical linear momentum balance equation within the CCP framework and is subsequently extended to solve the nonlocal field equations associated with the various SGCP models using a quantum finite difference approach. Notably, the QFT-method formulation achieves a computational complexity of $\mathcal{O}((\log(\mathrm{N}))^2)$, providing a polynomial speedup compared with respect to the classical FFT-methods, which scale as $\mathcal{O}(\mathrm{N}\log(\mathrm{N}))$.

High-resolution simulations of two-dimensional and three-dimensional polycrystalline aggregates are conducted using the proposed QFT-method. The two-dimensional simulations enable a systematic comparison between CSGCP and ESGCP formulations. In the CSGCP models, higher-order stresses increase monotonically during deformation, leading to progressive delocalization and suppression of geometrically necessary dislocation (GND) accumulation. In contrast, in the ESGCP models the coupling between the higher-order modulus and local softening within slip and kink bands reduces the influence of higher-order stresses as deformation proceeds, thereby maintaining localization and allowing sustained GND accumulation. Both CSGCP and ESGCP frameworks are further employed to analyze the *Hall–Petch* (mean-grain size) effect using microstructures with different average grain sizes. The results show that, in CSGCP models, strain gradient effects continuously intensify with increasing deformation, whereas in ESGCP models these effects are pronounced at lower level of loading but progressively reduce at higher loading, consistent with the original motivation of the ESGCP theory (Lame Jouybari et al., 2025). Finally, three-dimensional high-resolution simulations of irradiated polycrystalline aggregates demonstrate that the EMSlip model regularizes both slip and kink bands to the prescribed length scale, while the EMCurl-Star model breaks the equivalent ratio between slip and kink bands, transforming original kink bands from CCP

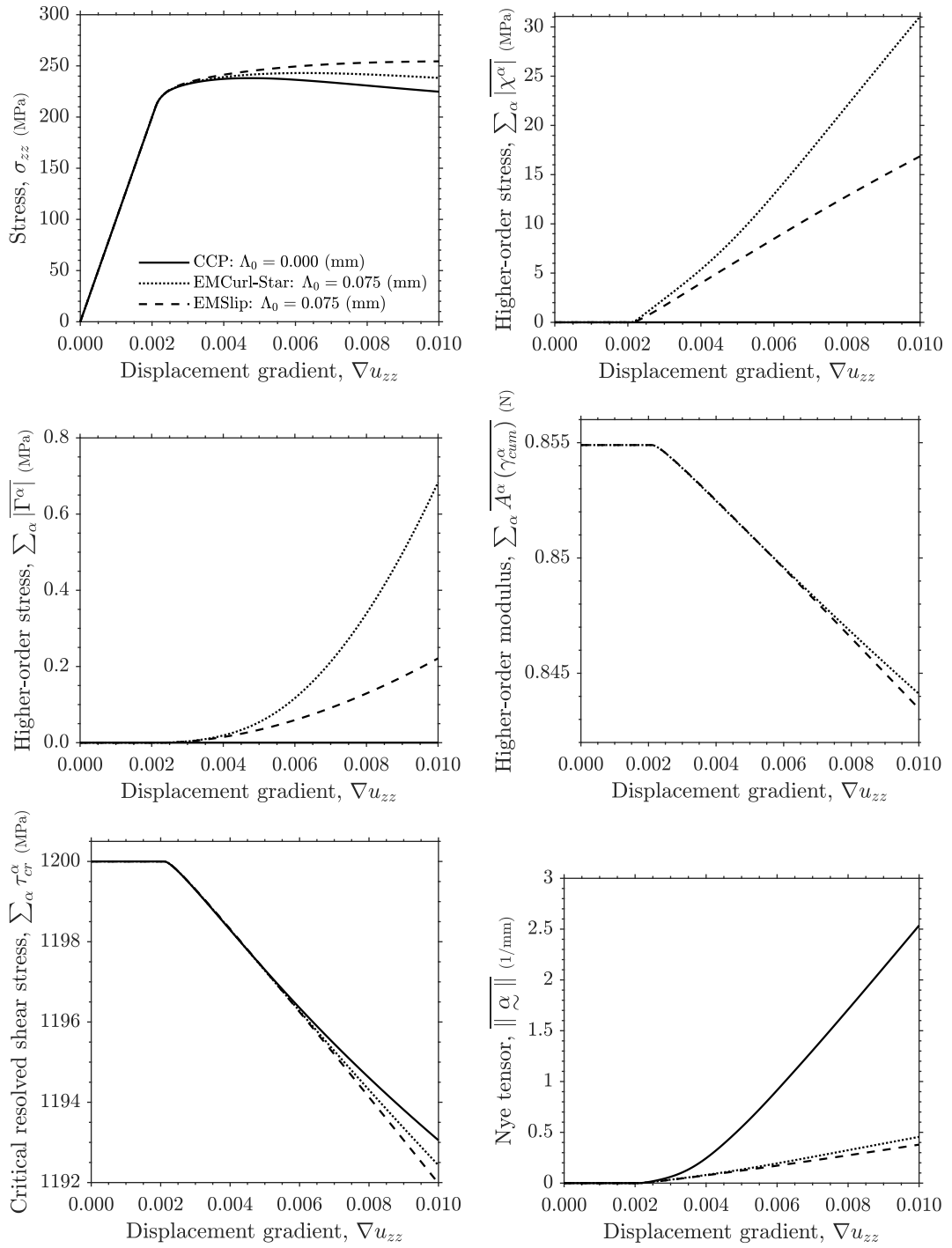

Fig. 10. Evolution of the spatially averaged state variables for the microstructure shown in Fig. 9 during applied loading. Results are obtained from the CCP framework ($\Lambda_0 = 0$ mm) and EMSlip and EMCurl-Star models with the length scale $\Lambda_0 = 0.075$ mm.

framework into bundles of parallel slip bands whose characteristic length is set by the internal length scale within the higher-order modulus.

Future work will focus on implementing the complete QFT-method algorithm within quantum software frameworks such as Qiskit and deploying it on real quantum hardware (e.g., IBM quantum processors). Additional developments will address the impact of noise and decoherence and will explore quantum error-mitigation strategies to enable reliable simulations on noisy intermediate-scale quantum (NISQ) devices.

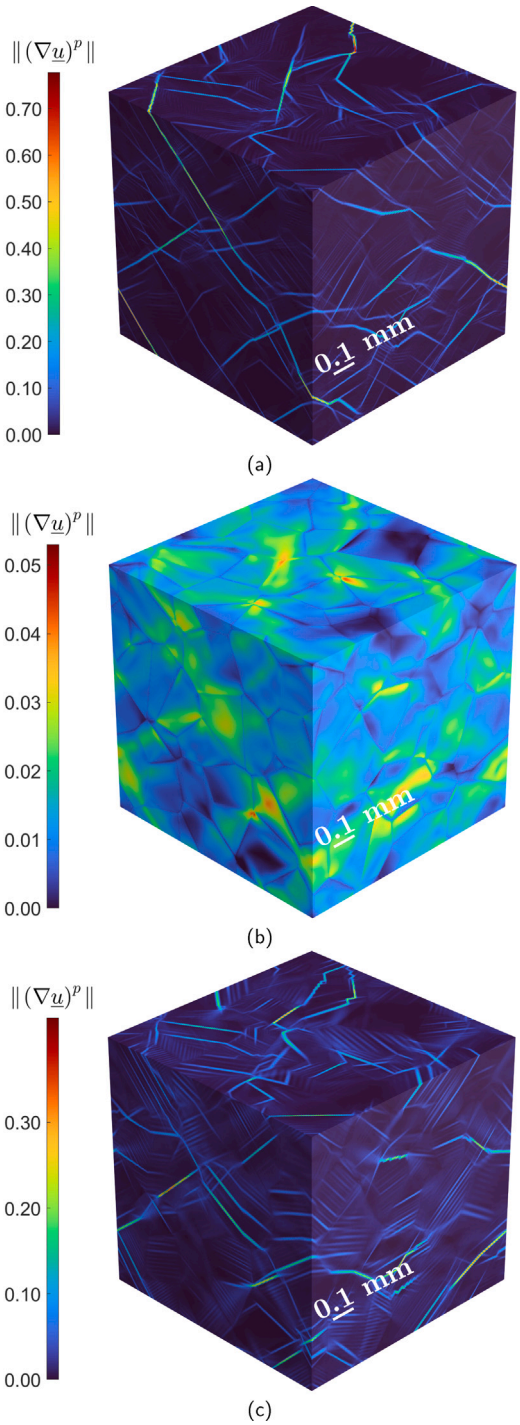

Fig. 11. Distribution of the norm of the plastic distortion tensor, $\| (\nabla \underline{u})^p \|$, in the three-dimensional microstructure shown in Fig. 9, at final stage of the deformation $\nabla u_{yy} = 0.01$, obtained from (a) the CCP framework ($\Lambda_0 = 0$ mm) and (b) EMSlip and (c) EMCurl-Star models with the length scale $\Lambda_0 = 0.075$ mm.

CRediT authorship contribution statement

Amirhossein Lame Jouybari: Writing – review & editing, Writing – original draft, Visualization, Validation, Software, Resources, Project administration, Methodology, Investigation, Formal analysis, Data curation, Conceptualization. **Leon Cizelj:** Supervision, Project administration, Funding acquisition.

Declaration of competing interest

The authors declare that they have no known competing financial interests or personal relationships that could have appeared to influence the work reported in this paper.

Acknowledgments

The authors gratefully acknowledge the financial support provided by Slovenian Research and Innovation Agency (grants P2-0026 and young researcher Amirhossein Lame Jouybari). The authors also thank Samir El Shawish for constructive discussions.

Appendix A. Fundamentals of quantum computing

In this study, quantum bits (qubits) and operations acting on qubits are expressed using the *Dirac* (bra–ket) notation. All quantum-state manipulations are assumed to satisfy the standard postulates of quantum mechanics, including the state-space, unitary evolution (operator), measurement, and tensor product postulates. According to the state-space postulate, the set of all admissible states of a quantum register forms a complex vector space endowed with an inner product, i.e., a *Hilbert* space, denoted here by $\mathbb{H}$. For a register of N qubits, the associated state space is finite dimensional and is isomorphic to $\mathbb{C}^{2^N}$, such that $\mathbb{H} \cong \mathbb{C}^{2^N}$.

The unitary evolution postulate states that the time evolution of an isolated (closed) quantum system is governed by a unitary operator, i.e., a linear operator whose inverse equals its Hermitian conjugate. The measurement postulate distinguishes this closed-system evolution from the measurement process: when an experiment is performed, or when the system interacts with an external environment, the system can no longer be considered closed, and its evolution is no longer purely unitary. Finally, the tensor product postulate specifies the construction of composite quantum systems. For a quantum state composed of m subsystems with state spaces $\mathbb{H}_i$, the total state space is given by the tensor product of the subsystem spaces, $\mathbb{H}^{\text{tot}} = \bigotimes_{i=0}^{m-1} \mathbb{H}_i$.

A.1. Quantum bit

A bit is the fundamental unit of information in classical computing and can assume one of two discrete states, **0** or **1**. Analogously, the quantum bit, or *qubit*, is the fundamental unit of quantum information in quantum computing. The classical binary states are generalized to the quantum computational basis states $|0\rangle = \begin{pmatrix} 1 \\ 0 \end{pmatrix}$ and $|1\rangle = \begin{pmatrix} 0 \\ 1 \end{pmatrix}$, which form an orthonormal basis of the single qubit state space. The key distinction between a qubit and a classical bit is that, whereas a classical bit must be either **0** or **1** at any time, a qubit can exist in the basis state $|0\rangle$, the basis state $|1\rangle$, or in any normalized linear combination (superposition) of these states. Accordingly, a single-qubit state $|\psi\rangle \in \mathbb{C}^2$ can be expressed as follows.

$$|\psi\rangle = \sum_{q=0}^{1} \psi_q |q\rangle = \psi_0 |0\rangle + \psi_1 |1\rangle; \qquad \psi_0^2 + \psi_1^2 = 1 \tag{A.1}$$

Here $\psi_q \in \mathbb{C}$ denotes the complex amplitude associated with each basis state. Upon measurement in the computational basis, the qubit collapses irreversibly to one of the basis states, and the probability of obtaining outcome q is given by $|\psi_q|^2$. Consequently, the state must be normalized such that the total probability equals unity, i.e., $\| \psi \| = \langle \psi | \psi \rangle = \sum_{q=0}^{1} |\psi_q|^2 = 1$. More generally, an n-qubit system is represented in the composite state space obtained from the tensor product of n single-qubit spaces.

$$\begin{aligned} |\psi\rangle &= |\psi_0\rangle \otimes |\psi_1\rangle \otimes \cdots \otimes |\psi_{n-2}\rangle \otimes |\psi_{n-1}\rangle \\ &= \sum_{q_0=0}^{1} \sum_{q_1=0}^{1} \cdots \sum_{q_{n-2}=0}^{1} \sum_{q_{n-1}=0}^{1} \psi_{q_0 q_1 \ldots q_{n-2} q_{n-1}} |q_0 q_1 \cdots q_{n-2} q_{n-1}\rangle \\ &= \sum_{q=0}^{2^n-1} \psi_q |q\rangle \end{aligned} \tag{A.2}$$

Here $\psi_q \in \mathbb{C}$ and $q = q_0 2^{n-1} + q_1 2^{n-2} + \cdots + q_{n-2} 2^1 + q_{n-1} 2^0 \equiv q_0 q_1 \cdots q_{n-2} q_{n-1}$, and $\sum_{q=0}^{2^n-1} \psi_q^2 = 1$.

Table 2
Quantum gate representation.

Name	symbol	Matrix representation
Identity gate	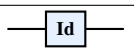	$[\mathbf{Id}] = \begin{bmatrix} 1 & 0 \\ 0 & 1 \end{bmatrix}$
Hadamard gate	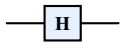	$[\mathbf{H}] = \begin{bmatrix} \frac{\sqrt{2}}{2} & \frac{\sqrt{2}}{2} \\ \frac{\sqrt{2}}{2} & -\frac{\sqrt{2}}{2} \end{bmatrix}$
Y-axis rotation gate		$[\mathbf{RY}_\theta] = \begin{bmatrix} \cos\left(\frac{\theta}{2}\right) & -\sin\left(\frac{\theta}{2}\right) \\ \sin\left(\frac{\theta}{2}\right) & \cos\left(\frac{\theta}{2}\right) \end{bmatrix}$
Z-axis rotation gate with global phase	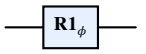	$[\mathbf{R1}_\phi] = \begin{bmatrix} 1 & 0 \\ 0 & \exp(j\phi) \end{bmatrix}$
Swap gate		$[\mathbf{Swap}] = \begin{bmatrix} 1 & 0 & 0 & 0 \\ 0 & 0 & 1 & 0 \\ 0 & 1 & 0 & 0 \\ 0 & 0 & 0 & 1 \end{bmatrix}$
Controlled not Gate	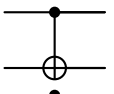	$[\mathbf{CNot}] = \begin{bmatrix} 1 & 0 & 0 & 0 \\ 0 & 1 & 0 & 0 \\ 0 & 0 & 0 & 1 \\ 0 & 0 & 1 & 0 \end{bmatrix}$
Controlled Z-axis rotation gate with global phase Gate	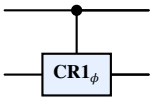	$[\mathbf{CR1}_\phi] = \begin{bmatrix} 1 & 0 & 0 & 0 \\ 0 & 1 & 0 & 0 \\ 0 & 0 & 1 & 0 \\ 0 & 0 & 0 & \exp(j\phi) \end{bmatrix}$

A.2. Quantum gate and circuit

In quantum computing, the evolution of a quantum state $|\psi\rangle$ to another quantum state $|\psi'\rangle \in \mathbb{C}^{2^n}$ is described by a unitary transformation, commonly referred to as a quantum gate. The corresponding operator is represented by a unitary matrix $U \in \mathbb{C}^{2^n \times 2^n}$ such that $|\psi'\rangle = U|\psi\rangle$. The unitarity requirement ensures that inner products, and hence amplitudes, are preserved during evolution, which in turn guarantees conservation of total probability.

$$|\psi'\rangle = U|\psi\rangle; \qquad U^\dagger = U^{-1} \tag{A.3}$$

Typically, quantum gates are visualized using circuit diagrams. These diagrams are read from left to right, where each horizontal wire represents a qubit (or, more generally, a quantum register line). For clarity, identity operations are often omitted from circuit drawings unless they are needed to emphasize synchronization between qubits or to indicate the timing of operations. The principal quantum gates employed in this study include the identity gate, Hadamard gate, controlled gate, rotation gate, swap gate, and controlled-rotation gate, as summarized in Table 2. Owing to their matrix representations, the role of each gate is briefly outlined here. The identity gate leaves the quantum state unchanged and is primarily used to denote that no operation is applied on a given qubit during the circuit. The Hadamard gate is a key single-qubit operation that creates superposition by mapping a computational basis state into an equal linear combination of basis states. The z-axis rotation gate (including a global phase) modifies the phase of the qubit by an angle ϕ. The swap gate acts on a two-qubit state and exchanges the corresponding amplitudes associated with the two qubits, thereby permuting the computational basis components. Finally, the controlled z-axis rotation gate (with global phase) applies the phase rotation to the target qubit conditioned on the control qubit being in the state $|1\rangle$.

Appendix B. State preparation

The first step in any quantum algorithm is the preparation of an appropriate initial quantum state. This task is commonly referred to as the state preparation problem. In general, classical data can be encoded into quantum states using a variety of strategies, including basis encoding, angle encoding, phase encoding, dense encoding, Hamiltonian encoding, and amplitude encoding. In this study, amplitude encoding is adopted, and its essential formulation is summarized in this appendix. More details can be obtained in Mottonen et al. (2004).

Consider a vector $\underline{v} \in \mathbb{R}^{\mathrm{n}}$ with n components in real space. To perform amplitude encoding (state preparation), the vector $\underline{v}$ is first normalized as in the following equation.

$$\vec{v} = \frac{\underline{v}}{\| \underline{v} \|} \tag{B.1}$$

A multi qubit register with $\mathrm{N^{qb}} = \lceil \log_2(\mathrm{n}) \rceil$ qubits is then introduced and initialized in the all-zero state, $|0\rangle^{\otimes \mathrm{N^{qb}}}$. Following the binary-tree construction, a sequence of recursive **IUCRY** gates — composed of $\mathbf{RY}_\theta$ and **CNot** operations — is applied to encode the normalized components of the vector into the amplitudes of the quantum state. Since all state-preparation procedures used in the

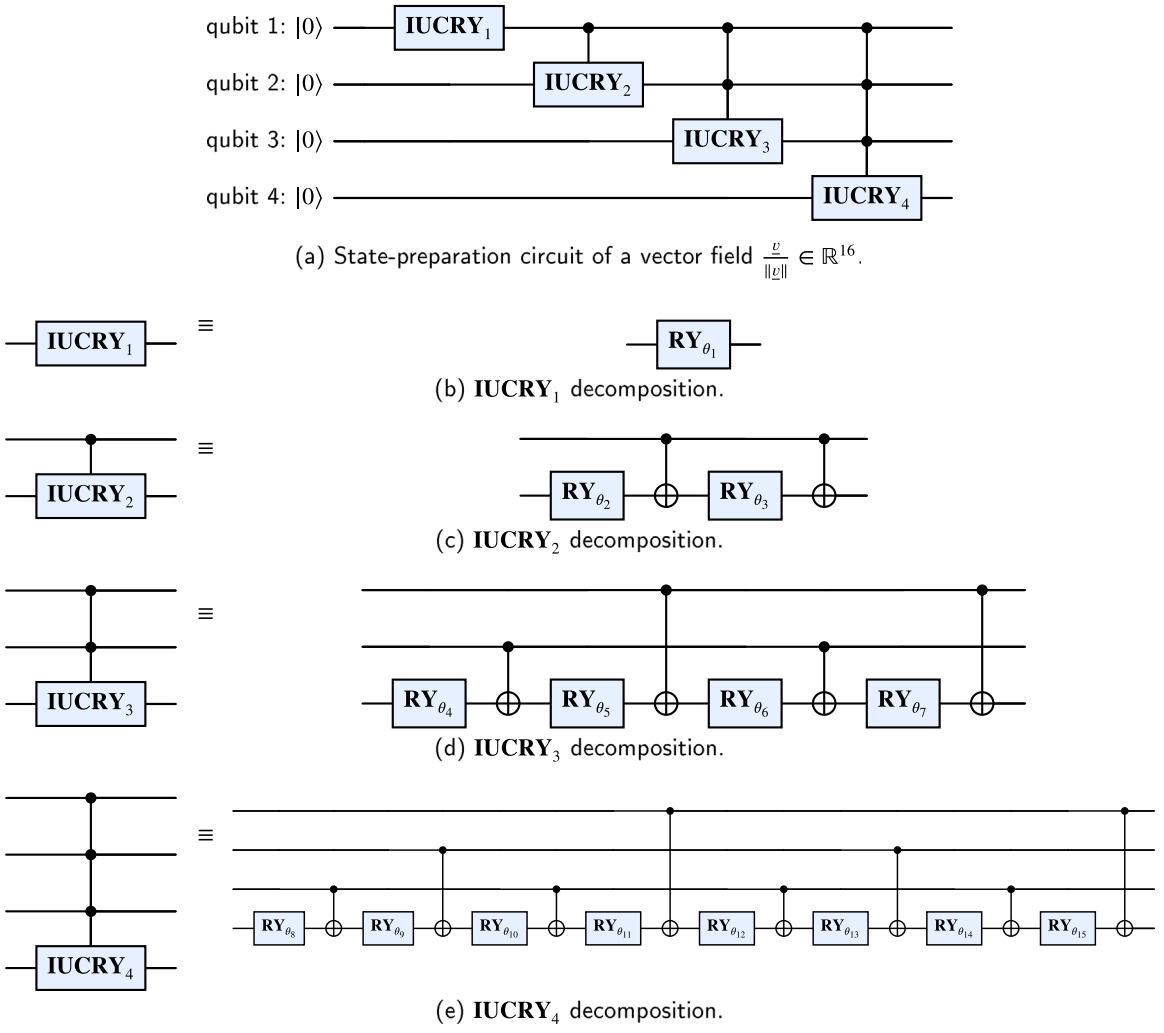

(a) State-preparation circuit of a vector field $\frac{\underline{v}}{\|\underline{v}\|} \in \mathbb{R}^{16}$.

(b) $\mathbf{IUCRY}_1$ decomposition.

(c) $\mathbf{IUCRY}_2$ decomposition.

(d) $\mathbf{IUCRY}_3$ decomposition.

(e) $\mathbf{IUCRY}_4$ decomposition.

Fig. B.1. State preparation circuit and decompositions of the inverse uniformly controlled $\mathbf{RY}_\theta$ rotations.

algorithm of Section 2.5 are performed in real space, the encoded data are purely real-valued; therefore, no additional phase-setting operations are required and the recursive $\mathbf{UCR_z}$ gates need not be applied.

$$|0\rangle^{\otimes \mathrm{N^{qb}}} \xrightarrow{\text{State preparation}} \sum_{q=0}^{2^{\mathrm{n}}-1} \psi_q |q\rangle; \qquad \psi_q = \frac{v_q}{\| \underline{v} \|} \tag{B.2}$$

Fig. B.1 illustrates the circuit used for state preparation (amplitude encoding) of a vector $\underline{v} \in \mathbb{R}^{16}$. In this example, four qubits are initialized in the computational basis state $|0000\rangle$. A single-qubit $\mathbf{RY}_\theta$ gate is first applied to the first qubit. Subsequently, a sequence of **IUCRY** gates is applied in a hierarchical manner, consistent with the binary-tree construction: the first **IUCRY** acts on the second qubit as the target, controlled by the first qubit; the second **IUCRY** acts on the third qubit as the target, controlled by the first and second qubits; and the third **IUCRY** acts on the fourth qubit as the target, controlled by the first, second, and third qubits.

Appendix C. Quantum Fourier transform

The discrete Fourier transform, $\mathcal{DFT}(f)$, of a scalar function $f \in \mathbb{R}$ defined on a discretized one-dimensional domain with N grid points, $[f] = [f_0, f_1, \ldots, f_{N-1}]$, maps the samples to their Fourier-space representation, $[\hat{f}] = [\hat{f}_0, \hat{f}_1, \ldots, \hat{f}_{N-1}]$, according to the following relation.

$$\hat{f}_k = \mathcal{DFT}(f) = \frac{1}{N} \sum_{l=0}^{N-1} f_l \exp\left(\frac{2\pi \mathrm{j} l k}{N}\right) \tag{C.1}$$

$$\left[\hat{f}\right] = \left[\mathcal{DFT}\right][f] \tag{C.2}$$

$$\left[\mathcal{DFT}\right] = \frac{1}{N}\begin{bmatrix} 1 & 1 & 1 & 1 & \cdots & 1 \\ 1 & \omega & \omega^2 & \omega^3 & \cdots & \omega^{N-1} \\ 1 & \omega^2 & \omega^4 & \omega^6 & \cdots & \omega^{2(N-1)} \\ 1 & \omega^3 & \omega^6 & \omega^9 & \cdots & \omega^{3(N-1)} \\ \vdots & \vdots & \vdots & \vdots & \ddots & \vdots \\ 1 & \omega^{N-1} & \omega^{2(N-1)} & \omega^{3(N-1)} & \cdots & \omega^{(N-1)(N-1)} \end{bmatrix} \tag{C.3}$$

$$f_k = \mathcal{IDFT}\left(\hat{f}\right) = \sum_{l=0}^{N-1} \hat{f}_l \exp\left(-\frac{2\pi \mathrm{j} l k}{N}\right) \tag{C.4}$$

Here $\omega = \exp\left(\frac{2\pi \mathrm{j}}{\mathrm{N}}\right)$ and $\mathcal{IDFT}$ denote, respectively, the Nth root of unity and the inverse discrete Fourier transform. Furthermore, it can be shown that the discrete Fourier transform is a unitary transformation, i.e., $\left[\mathcal{DFT}\right]^{\dagger} = \left[\mathcal{DFT}\right]^{-1}$. Consequently, the discrete Fourier transform can be implemented as a unitary operation and, therefore, admits realization by an appropriate quantum circuit.

Consider a normalized discretized scalar function, $\overrightarrow{f} = \frac{f}{\|f\|}$, encoded into the amplitudes of a quantum register with $\mathrm{N}^{\mathrm{qb}} = \left\lceil \log_2(\mathrm{N}) \right\rceil$ qubits, such that $|\overrightarrow{f}\rangle = \sum_{q=0}^{2^{\mathrm{N}^{\mathrm{qb}}}-1} f_q |q\rangle$. Applying the quantum Fourier transform to this register then yields:

$$\mathbf{QFT}: \sum_{q=0}^{2^{\mathrm{N}^{\mathrm{qb}}}-1} f_q|q\rangle \longmapsto \sum_{p=0}^{2^{\mathrm{N}^{\mathrm{qb}}}-1} \hat{f}_p|p\rangle \tag{C.5}$$

As an example, consider a scalar function with 16 components. In this case, a quantum register of four qubits is required, and the corresponding quantum Fourier transform can be implemented by the circuit shown in Fig. C.1. The matrix representation of this circuit is provided in Eq. (C.6).

$$\begin{aligned}
[\mathbf{QFT}] = {} & \left(\left[\mathbf{H}^{q1}\right] \otimes \left[\mathbf{Id}^{q2}\right] \otimes \left[\mathbf{Id}^{q3}\right] \otimes \left[\mathbf{Id}^{q4}\right]\right)\left(\left[\mathbf{Cr1}_{\frac{\pi}{2}}^{q1-q2}\right] \otimes \left[\mathbf{Id}^{q3}\right] \otimes \left[\mathbf{Id}^{q4}\right]\right) \\
& \left(\left[\mathbf{Cr1}_{\frac{\pi}{4}}^{q1-q3}\right] \otimes \left[\mathbf{Id}^{q2}\right] \otimes \left[\mathbf{Id}^{q4}\right]\right)\left(\left[\mathbf{Cr1}_{\frac{\pi}{8}}^{q1-q4}\right] \otimes \left[\mathbf{Id}^{q2}\right] \otimes \left[\mathbf{Id}^{q3}\right]\right) \\
& \left(\left[\mathbf{Id}^{q1}\right] \otimes \left[\mathbf{H}^{q2}\right] \otimes \left[\mathbf{Id}^{q3}\right] \otimes \left[\mathbf{Id}^{q4}\right]\right)\left(\left[\mathbf{Id}^{q1}\right] \otimes \left[\mathbf{Cr1}_{\frac{\pi}{2}}^{q2-q3}\right] \otimes \left[\mathbf{Id}^{q4}\right]\right) \\
& \left(\left[\mathbf{Id}^{q1}\right] \otimes \left[\mathbf{Cr1}_{\frac{\pi}{4}}^{q2-q4}\right] \otimes \left[\mathbf{Id}^{q3}\right]\right)\left(\left[\mathbf{Id}^{q1}\right] \otimes \left[\mathbf{Id}^{q2}\right] \otimes \left[\mathbf{H}^{q3}\right] \otimes \left[\mathbf{Id}^{q4}\right]\right) \\
& \left(\left[\mathbf{Id}^{q1}\right] \otimes \left[\mathbf{Id}^{q2}\right] \otimes \left[\mathbf{Cr1}_{\frac{\pi}{2}}^{q3-q4}\right]\right)\left(\left[\mathbf{Id}^{q1}\right] \otimes \left[\mathbf{Id}^{q2}\right] \otimes \left[\mathbf{Id}^{q3}\right] \otimes \left[\mathbf{H}^{q4}\right]\right) \\
& \left(\left[\mathbf{Swap}^{q1-q4}\right] \otimes \left[\mathbf{Id}^{q2}\right] \otimes \left[\mathbf{Id}^{q3}\right]\right)\left(\left[\mathbf{Id}^{q1}\right] \otimes \left[\mathbf{Swap}^{q2-q3}\right] \otimes \left[\mathbf{Id}^{q4}\right]\right) \\
= {} & \frac{1}{\sqrt{2^4}}\begin{bmatrix}
1 & 1 & 1 & 1 & 1 & 1 & 1 & 1 & 1 & 1 & 1 & 1 & 1 & 1 & 1 & 1 \\
1 & \omega & \omega^2 & \omega^3 & \omega^4 & \omega^5 & \omega^6 & \omega^7 & \omega^8 & \omega^9 & \omega^{10} & \omega^{11} & \omega^{12} & \omega^{13} & \omega^{14} & \omega^{15} \\
1 & \omega^2 & \omega^4 & \omega^6 & \omega^8 & \omega^{10} & \omega^{12} & \omega^{14} & \omega^{16} & \omega^{18} & \omega^{20} & \omega^{22} & \omega^{24} & \omega^{26} & \omega^{28} & \omega^{30} \\
1 & \omega^3 & \omega^6 & \omega^9 & \omega^{12} & \omega^{15} & \omega^{18} & \omega^{21} & \omega^{24} & \omega^{27} & \omega^{30} & \omega^{33} & \omega^{36} & \omega^{39} & \omega^{42} & \omega^{45} \\
1 & \omega^4 & \omega^8 & \omega^{12} & \omega^{16} & \omega^{20} & \omega^{24} & \omega^{28} & \omega^{32} & \omega^{36} & \omega^{40} & \omega^{44} & \omega^{48} & \omega^{52} & \omega^{56} & \omega^{60} \\
1 & \omega^5 & \omega^{10} & \omega^{15} & \omega^{20} & \omega^{25} & \omega^{30} & \omega^{35} & \omega^{40} & \omega^{45} & \omega^{50} & \omega^{55} & \omega^{60} & \omega^{65} & \omega^{70} & \omega^{75} \\
1 & \omega^6 & \omega^{12} & \omega^{18} & \omega^{24} & \omega^{30} & \omega^{36} & \omega^{42} & \omega^{48} & \omega^{54} & \omega^{60} & \omega^{66} & \omega^{72} & \omega^{78} & \omega^{84} & \omega^{90} \\
1 & \omega^7 & \omega^{14} & \omega^{21} & \omega^{28} & \omega^{35} & \omega^{42} & \omega^{49} & \omega^{56} & \omega^{63} & \omega^{70} & \omega^{77} & \omega^{84} & \omega^{91} & \omega^{98} & \omega^{105} \\
1 & \omega^8 & \omega^{16} & \omega^{24} & \omega^{32} & \omega^{40} & \omega^{48} & \omega^{56} & \omega^{64} & \omega^{72} & \omega^{80} & \omega^{88} & \omega^{96} & \omega^{104} & \omega^{112} & \omega^{120} \\
1 & \omega^9 & \omega^{18} & \omega^{27} & \omega^{36} & \omega^{45} & \omega^{54} & \omega^{63} & \omega^{72} & \omega^{81} & \omega^{90} & \omega^{99} & \omega^{108} & \omega^{117} & \omega^{126} & \omega^{135} \\
1 & \omega^{10} & \omega^{20} & \omega^{30} & \omega^{40} & \omega^{50} & \omega^{60} & \omega^{70} & \omega^{80} & \omega^{90} & \omega^{100} & \omega^{110} & \omega^{120} & \omega^{130} & \omega^{140} & \omega^{150} \\
1 & \omega^{11} & \omega^{22} & \omega^{33} & \omega^{44} & \omega^{55} & \omega^{66} & \omega^{77} & \omega^{88} & \omega^{99} & \omega^{110} & \omega^{121} & \omega^{132} & \omega^{143} & \omega^{154} & \omega^{165} \\
1 & \omega^{12} & \omega^{24} & \omega^{36} & \omega^{48} & \omega^{60} & \omega^{72} & \omega^{84} & \omega^{96} & \omega^{108} & \omega^{120} & \omega^{132} & \omega^{144} & \omega^{156} & \omega^{168} & \omega^{180} \\
1 & \omega^{13} & \omega^{26} & \omega^{39} & \omega^{52} & \omega^{65} & \omega^{78} & \omega^{91} & \omega^{104} & \omega^{117} & \omega^{130} & \omega^{143} & \omega^{156} & \omega^{169} & \omega^{182} & \omega^{195} \\
1 & \omega^{14} & \omega^{28} & \omega^{42} & \omega^{56} & \omega^{70} & \omega^{84} & \omega^{98} & \omega^{112} & \omega^{126} & \omega^{140} & \omega^{154} & \omega^{168} & \omega^{182} & \omega^{196} & \omega^{210} \\
1 & \omega^{15} & \omega^{30} & \omega^{45} & \omega^{60} & \omega^{75} & \omega^{90} & \omega^{105} & \omega^{120} & \omega^{135} & \omega^{150} & \omega^{165} & \omega^{180} & \omega^{195} & \omega^{210} & \omega^{225}
\end{bmatrix}
\end{aligned} \tag{C.6}$$

which is exactly equal to the normalized matrix form of the discrete Fourier transform given in Eq. (C.3) for the $N = 16$. Following the pioneering work of Cooley and Tukey (1965), the classical Cooley–Tukey FFT algorithm achieves the computational cost of evaluating Fourier coefficients to $\mathcal{O}(\mathrm{N}\log N)$. Furthermore, the quantum Fourier transform (QFT) can be implemented with a circuit complexity on the order of $\mathcal{O}((\log N)^2)$ (Coppersmith, 2002). Fig. C.3 illustrates this comparison, highlighting the explicit poly-logarithmic speed-up of the QFT over the FFT and its resulting advantages as the data size increases. This comparison highlights the asymptotic efficiency of the QFT circuit relative to the classical FFT and motivates its potential benefit for high-resolution microstructure simulations.

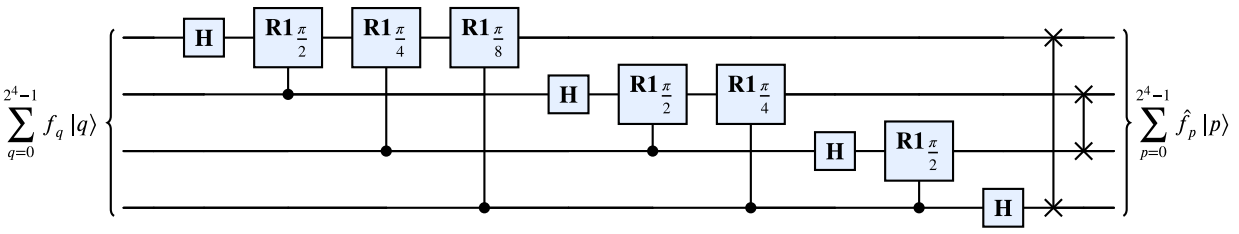

Fig. C.1. Quantum Fourier transform on $N^{\mathrm{qb}} = 4$ qubits: $|f\rangle \mapsto |\hat{f}\rangle$.

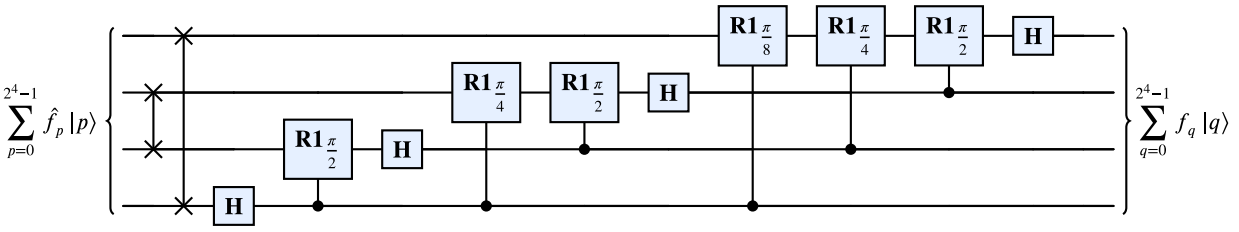

Fig. C.2. Inverse quantum Fourier transform on $N^{\mathrm{qb}} = 4$ qubits: $|\hat{f}\rangle \mapsto |f\rangle$.

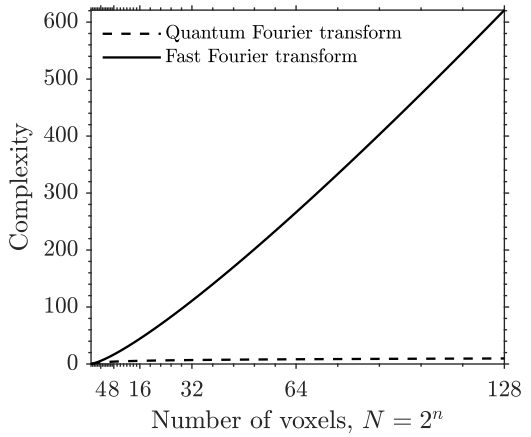

Fig. C.3. Complexity and computational costs of the FFT-algorithm and QFT circuit.

Furthermore, the inverse quantum Fourier transform is implemented by executing the quantum Fourier transform circuit in reverse order, as illustrated in Fig. C.2.

$$\mathbf{IQFT}: \sum_{p=0}^{2^{\mathrm{Nqb}}-1} \hat{f}_p|p\rangle \longmapsto \sum_{q=0}^{2^{\mathrm{Nqb}}-1} f_q|q\rangle \tag{C.7}$$

For example, the quantum circuit implementing the inverse quantum Fourier transform for the scalar function defined in Eq. (C.8) with sixteen components is shown as follows:

$$\begin{aligned}
[\mathbf{IQFT}] = &\left(\left[\mathbf{Id}^{q1}\right] \otimes \left[\mathbf{Swap}^{q2-q3}\right] \otimes \left[\mathbf{Id}^{q4}\right]\right)\left(\left[\mathbf{Swap}^{q1-q4}\right] \otimes \left[\mathbf{Id}^{q2}\right] \otimes \left[\mathbf{Id}^{q3}\right]\right)\\
&\left(\left[\mathbf{Id}^{q1}\right] \otimes \left[\mathbf{Id}^{q2}\right] \otimes \left[\mathbf{Id}^{q3}\right] \otimes \left[\mathbf{H}^{q4}\right]\right)\left(\left[\mathbf{Id}^{q1}\right] \otimes \left[\mathbf{Id}^{q2}\right] \otimes \left[\mathbf{Cr1}_{\frac{\pi}{2}}^{q3-q4}\right]\right)\\
&\left(\left[\mathbf{Id}^{q1}\right] \otimes \left[\mathbf{Id}^{q2}\right] \otimes \left[\mathbf{H}^{q3}\right] \otimes \left[\mathbf{Id}^{q4}\right]\right)\left(\left[\mathbf{Id}^{q1}\right] \otimes \left[\mathbf{Cr1}_{\frac{\pi}{4}}^{q2-q4}\right] \otimes \left[\mathbf{Id}^{q3}\right]\right)\\
&\left(\left[\mathbf{Id}^{q1}\right] \otimes \left[\mathbf{Cr1}_{\frac{\pi}{2}}^{q2-q3}\right] \otimes \left[\mathbf{Id}^{q4}\right]\right)\left(\left[\mathbf{Id}^{q1}\right] \otimes \left[\mathbf{H}^{q2}\right] \otimes \left[\mathbf{Id}^{q3}\right] \otimes \left[\mathbf{Id}^{q4}\right]\right)
\end{aligned}$$

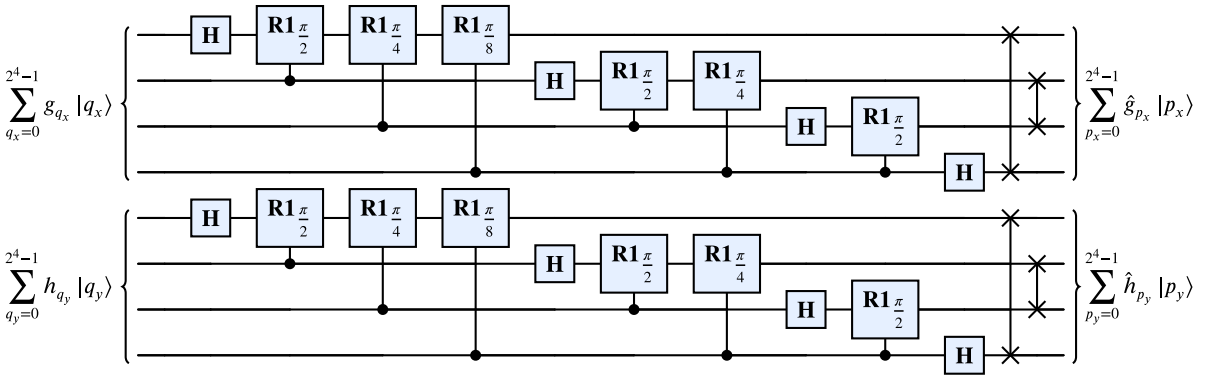

Fig. C.4. Two-dimensional QFT as $\mathbf{QFT}^{2d} = \mathbf{QFT}^{1d} \otimes \mathbf{QFT}^{1d}$: two independent 4-qubit QFT blocks acting on two registers.

$$\begin{aligned}&\left(\left[\mathbf{Cr1}_{\frac{\pi}{8}}^{q1-q4}\right] \otimes \left[\mathbf{Id}^{q2}\right] \otimes \left[\mathbf{Id}^{q3}\right]\right)\left(\left[\mathbf{Cr1}_{\frac{\pi}{4}}^{q1-q3}\right] \otimes \left[\mathbf{Id}^{q2}\right] \otimes \left[\mathbf{Id}^{q4}\right]\right)\\ &\left(\left[\mathbf{Cr1}_{\frac{\pi}{2}}^{q1-q2}\right] \otimes \left[\mathbf{Id}^{q3}\right] \otimes \left[\mathbf{Id}^{q4}\right]\right)\left(\left[\mathbf{H}^{q1}\right] \otimes \left[\mathbf{Id}^{q2}\right] \otimes \left[\mathbf{Id}^{q3}\right] \otimes \left[\mathbf{Id}^{q4}\right]\right)\\ =&[\mathbf{QFT}]^{\dagger}\end{aligned} \tag{C.8}$$

C.1. Two-dimensional quantum Fourier transform

Consider a scalar function f defined on a discrete two-dimensional domain with $\mathrm{N}_x \times \mathrm{N}_y$ grid points, such that:

$$f_{ij} = g_i h_j : \{1, 2, \ldots, \mathrm{N}_x\} \otimes \{1, 2, \ldots, \mathrm{N}_y\} \longmapsto \mathbb{R} \tag{C.9}$$

Initially, the scalar function on a discretized domain is aligned to the vector such that:

$$\overrightarrow{f} = \mathrm{Vec}\left(f_{ij}\right) = \left\{ f_{11}, f_{21}, \ldots, f_{\mathrm{N}_x 1}, f_{12}, f_{22}, \ldots, f_{\mathrm{N}_x 2}, \ldots, f_{1\mathrm{N}_y}, f_{2\mathrm{N}_y}, \ldots, f_{\mathrm{N}_x \mathrm{N}_y} \right\} \tag{C.10}$$

Then, by applying the state-preparation procedure described in Appendix B, the normalized vector $\overrightarrow{f}$ is encoded into a quantum register $|\overrightarrow{f}\rangle$ comprising $\mathrm{N}^{\text{qb-tot}} = \mathrm{N}^{\text{qb-x}} + \mathrm{N}^{\text{qb-y}}$ qubits, where $\mathrm{N}^{\text{qb-x}} = \lceil \log_2(\mathrm{N}_x) \rceil$ and $\mathrm{N}^{\text{qb-y}} = \lceil \log_2(\mathrm{N}_y) \rceil$ are allocated to represent the x- and y-directions, respectively. The circuit corresponding to the two-dimensional quantum Fourier transform is then constructed as the tensor product of two one-dimensional QFT circuits, as illustrated in Fig. C.4.

$$[\mathbf{QFT}^{2d}] = [\mathbf{QFT}^{1d}] \otimes [\mathbf{QFT}^{1d}] : |\overrightarrow{f}\rangle \longmapsto |\widehat{\overrightarrow{f}}\rangle \tag{C.11}$$

Similar to the one-dimensional case, the two-dimensional inverse quantum Fourier transform is implemented by executing the corresponding two-dimensional quantum Fourier transform circuit in reverse order.

C.2. Three-dimensional quantum Fourier transform

Similar to Appendix C.1, consider a scalar function f defined on a discrete three-dimensional domain with resolution $\mathrm{N}_x \times \mathrm{N}_y \times \mathrm{N}_z$ in the Cartesian directions, such that:

$$f_{ijk} = g_i h_j k_l : \{1, 2, \ldots, \mathrm{N}_x\} \otimes \{1, 2, \ldots, \mathrm{N}_y\} \otimes \{1, 2, \ldots, \mathrm{N}_z\} \longmapsto \mathbb{R} \tag{C.12}$$

Then the scalar function is aligned to the vector such that:

$$\overrightarrow{f} = \mathrm{Vec}\left(f_{ijk}\right) = \left\{ f_{111}, f_{211}, \ldots, f_{\mathrm{N}_x 11}, f_{121}, f_{221}, \ldots, f_{\mathrm{N}_x 21}, \ldots, f_{1\mathrm{N}_y \mathrm{N}_z}, f_{2\mathrm{N}_y \mathrm{N}_z}, \ldots, f_{\mathrm{N}_x \mathrm{N}_y \mathrm{N}_z} \right\} \tag{C.13}$$

Then, by applying the state preparation procedure described in Appendix B, the normalized vector $\overrightarrow{f}$ is encoded into a quantum register $|\overrightarrow{f}\rangle$ composing $\mathrm{N}^{\text{qb-tot}} = \mathrm{N}^{\text{qb-x}} + \mathrm{N}^{\text{qb-y}} + \mathrm{N}^{\text{qb-z}}$ qubits, where $\mathrm{N}^{\text{qb-x}} = \lceil \log_2(\mathrm{N}_x) \rceil$, $\mathrm{N}^{\text{qb-y}} = \lceil \log_2(\mathrm{N}_y) \rceil$, and $\mathrm{N}^{\text{qb-z}} = \lceil \log_2(\mathrm{N}_z) \rceil$ are allocated to represent the x-, y-, and z-directions, respectively. The circuit corresponding to the three-dimensional quantum Fourier transform is then constructed as the tensor product of three one-dimensional QFT circuits, as illustrated in Fig. C.5.

$$[\mathbf{QFT}^{3d}] = [\mathbf{QFT}^{2d}] \otimes [\mathbf{QFT}^{1d}] = [\mathbf{QFT}^{1d}] \otimes [\mathbf{QFT}^{1d}] \otimes [\mathbf{QFT}^{1d}] : |\overrightarrow{f}\rangle \longmapsto |\widehat{\overrightarrow{f}}\rangle \tag{C.14}$$

Smiliar to the one-dimensional and two-dimensional cases, the three-dimensional inverse quantum Fourier transform is implemented by executing the corresponding three-dimensional quantum Fourier transform circuit in reverse order.

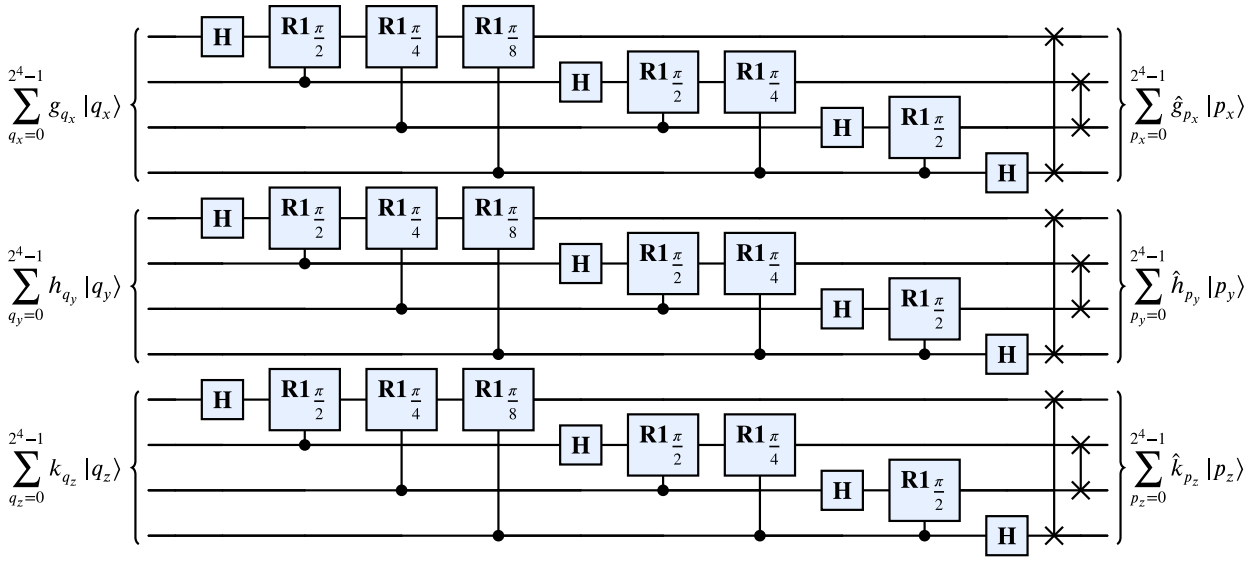

Fig. C.5. Three-dimensional QFT as $\mathbf{QFT}^{3d} = \mathbf{QFT}^{1d} \otimes \mathbf{QFT}^{1d} \otimes \mathbf{QFT}^{1d}$: three independent 4-qubit QFT blocks acting on three registers.

C.3. Application on the finite difference method

Consider a scalar function defined on a discretized one-dimensional domain with N grid points, where $f_p \in \mathbb{R}$ and $p \in \{1, 2, \dots, N-1\}$. Using the finite difference method with the 63-point finite difference scheme (FDS), consistent with the regular voxel discretization used in the FFT/QFT, the first derivative of this function on the discretized domain can be expressed as follows.

$$\frac{\partial f}{\partial x}(p) = \frac{-f(p+2) + 8f(p+1) - 8f(p-1) + f(p-2)}{12\Delta x} \tag{C.15}$$

Initially, a quantum register with $\mathrm{N^{qb}} = \lceil \log_2(\mathrm{N}) \rceil$ qubits is introduced. The scalar function is then normalized as $\overline{f} = \frac{1}{\|f\|} f$ and encoded into the amplitudes of the register such that $|\overline{f}\rangle = \sum_{q=0}^{2^{\mathrm{N^{qb}}}-1} f_q |q\rangle$. The quantum Fourier transform circuit corresponding to this register size is subsequently defined. By applying the quantum Fourier transform to both sides of Eq. (C.15), the finite difference scheme is mapped to Fourier space, yielding the following expression.

$$\begin{aligned}
\mathcal{QFT}\left(\frac{\partial f}{\partial x}\right)(p) = \frac{1}{12\Delta x\sqrt{2^{\mathrm{N^{qb}}}}}[&- \sum_{q=0}^{2^{\mathrm{N^{qb}}}-1} f_{q+2} \exp\left(\frac{2\pi \mathrm{j}}{2^{\mathrm{N^{qb}}}} pq\right) + 8 \sum_{q=0}^{2^{\mathrm{N^{qb}}}-1} f_{q+1} \exp\left(\frac{2\pi \mathrm{j}}{2^{\mathrm{N^{qb}}}} pq\right) \\
&- 8 \sum_{q=0}^{2^{\mathrm{N^{qb}}}-1} f_{q-1} \exp\left(\frac{2\pi \mathrm{j}}{2^{\mathrm{N^{qb}}}} pq\right) + \sum_{q=0}^{2^{\mathrm{N^{qb}}}-1} f_{q-2} \exp\left(\frac{2\pi \mathrm{j}}{2^{\mathrm{N^{qb}}}} pq\right)]
\end{aligned} \tag{C.16}$$

$$\begin{aligned}
= \frac{1}{12\Delta x\sqrt{2^{\mathrm{N^{qb}}}}}[&- \exp\left(\frac{4\pi \mathrm{j} p}{2^{\mathrm{N^{qb}}}}\right) \sum_{q=0}^{2^{\mathrm{N^{qb}}}-1} f_{q+2} \exp\left(\frac{2\pi \mathrm{j}}{2^{\mathrm{N^{qb}}}} p(q+2)\right) \\
&+ 8 \exp\left(\frac{2\pi \mathrm{j} p}{2^{\mathrm{N^{qb}}}}\right) \sum_{q=0}^{2^{\mathrm{N^{qb}}}-1} f_{q+1} \exp\left(\frac{2\pi \mathrm{j}}{2^{\mathrm{N^{qb}}}} p(q+1)\right) \\
&- 8 \exp\left(\frac{-2\pi \mathrm{j} p}{2^{\mathrm{N^{qb}}}}\right) \sum_{q=0}^{2^{\mathrm{N^{qb}}}-1} f_{q-1} \exp\left(\frac{2\pi \mathrm{j}}{2^{\mathrm{N^{qb}}}} p(q-1)\right) \\
&+ \exp\left(\frac{-4\pi \mathrm{j} p}{2^{\mathrm{N^{qb}}}}\right) \sum_{q=0}^{2^{\mathrm{N^{qb}}}-1} f_{q-2} \exp\left(\frac{2\pi \mathrm{j}}{2^{\mathrm{N^{qb}}}} p(q-2)\right)]
\end{aligned} \tag{C.17}$$

By introducing the new indices $q_1 = q+2$, $q_2 = q+1$, $q_3 = q-1$, and $q_4 = q-2$, Eq. (C.17) turns to the following equation:

$$\mathcal{QFT}\left(\frac{\partial f}{\partial x}\right)(p) = -\frac{\exp\left(\frac{4\pi \mathrm{j} p}{2^{\mathrm{N^{qb}}}}\right)}{12\Delta x}\left[\frac{1}{\sqrt{2^{\mathrm{N^{qb}}}}} \sum_{q_1=2}^{2^{\mathrm{N^{qb}}}+1} f_{q_1} \exp\left(\frac{2\pi \mathrm{j}}{2^{\mathrm{N^{qb}}}} pq_1\right)\right]$$

$$+\ 8\frac{\exp\left(\frac{2\pi \mathrm{j} p}{2^{N^{qb}}}\right)}{12\Delta x}\left[\frac{1}{\sqrt{2^{N^{qb}}}}\sum_{q_2=1}^{2^{N^{qb}}} f_{q_2}\exp\left(\frac{2\pi \mathrm{j}}{2^{N^{qb}}}pq_2\right)\right]$$
$$-\ 8\frac{\exp\left(\frac{-2\pi \mathrm{j} p}{2^{N^{qb}}}\right)}{12\Delta x}\left[\frac{1}{\sqrt{2^{N^{qb}}}}\sum_{q_3=-1}^{2^{N^{qb}}-2} f_{q_3}\exp\left(\frac{2\pi \mathrm{j}}{2^{N^{qb}}}pq_3\right)\right]$$
$$+\ \frac{\exp\left(\frac{-4\pi \mathrm{j} p}{2^{N^{qb}}}\right)}{12\Delta x}\left[\frac{1}{\sqrt{2^{N^{qb}}}}\sum_{q_4=-2}^{2^{N^{qb}}-3} f_{q_4}\exp\left(\frac{2\pi \mathrm{j}}{2^{N^{qb}}}pq_4\right)\right] \tag{C.18}$$

$$=\frac{-\exp\left(\frac{4\pi \mathrm{j} p}{2^{N^{qb}}}\right)+8\exp\left(\frac{2\pi \mathrm{j} p}{2^{N^{qb}}}\right)-8\exp\left(\frac{-2\pi \mathrm{j} p}{2^{N^{qb}}}\right)+\exp\left(\frac{-4\pi \mathrm{j} p}{2^{N^{qb}}}\right)}{12\Delta x}\mathcal{QFT}\left(|\vec{f}\rangle\right) \tag{C.19}$$

$$=\mathrm{j}\frac{\sin\left(\frac{4\pi p}{2^{N^{qb}}}\right)+8\sin\left(\frac{2\pi p}{2^{N^{qb}}}\right)}{6\Delta x}\mathcal{QFT}\left(|\vec{f}\rangle\right) \tag{C.20}$$

$$=\mathfrak{f}^{1,m}(p)\mathcal{QFT}\left(|\vec{f}\rangle\right) \tag{C.21}$$

Here, in Eq. (C.21), $\mathfrak{f}^{1,m}$ denotes the modified frequency associated with the first-order derivative in Fourier space, and j denotes the imaginary unit.

A similar procedure can be applied to the second-order derivative of the scalar function to obtain the corresponding modified frequency representation. Accordingly, the 63-point FDS for the second-order derivative of a scalar function defined on the discretized domain can be written as follows.

$$\frac{\partial^2 f}{\partial x^2}(p)=\frac{-f(p+2)+16f(p+1)-30f(p)+16f(p-1)-f(p-2)}{12\Delta x^2} \tag{C.22}$$

By applying the quantum Fourier transform to both sides of Eq. (C.22), the expression for the modified frequency associated with the second-order derivative is obtained.

$$\mathcal{QFT}\left(\frac{\partial^2 f}{\partial x^2}\right)(p)=\frac{\exp\left(\frac{4\pi \mathrm{j} p}{2^{N^{qb}}}\right)+16\exp\left(\frac{2\pi \mathrm{j} p}{2^{N^{qb}}}\right)-30+16\exp\left(\frac{-2\pi \mathrm{j} p}{2^{N^{qb}}}\right)-\exp\left(\frac{-4\pi \mathrm{j} p}{2^{N^{qb}}}\right)}{12\Delta x^2}\mathcal{QFT}\left(|\vec{f}\rangle\right) \tag{C.23}$$

$$=\frac{-\cos\left(\frac{4\pi \mathrm{j} p}{2^{N^{qb}}}\right)+16\cos\left(\frac{2\pi \mathrm{j} p}{2^{N^{qb}}}\right)+15}{6\Delta x^2}\mathcal{QFT}\left(|\vec{f}\rangle\right) \tag{C.24}$$

$$=\mathfrak{f}^{2,m}(p)\mathcal{QFT}\left(|\vec{f}\rangle\right) \tag{C.25}$$

Accordingly, the modified frequencies associated with the first- and second-order derivatives in three-dimensional space are generalized as follows.

$$\mathfrak{f}_i^{1,m}=\frac{1}{6\Delta x_i}\left[-\sin(2\xi_i)+8\sin(\xi_i)\right]+\mathcal{O}(\Delta x_i^4) \tag{C.26}$$

$$\mathfrak{f}_i^{2,m}=\begin{cases}\frac{2}{6\Delta x_i^2}\left[-\cos(2\xi_i)+16\cos(\xi_i)-15\right]+\mathcal{O}(\Delta x_i^2) & \text{if } i=j\\ \frac{1}{2\Delta x_i\,\Delta x_j}\left[-\cos(\xi_i+\xi_j)-\cos(\xi_i+2\xi_j)\right. & \\ \quad +10\cos(\xi_i+\xi_j)-10\cos(-\xi_i+2\xi_j) & \\ \quad \left.+\cos(2\xi_i-\xi_j)+\cos(-\xi_i+2\xi_j)\right]+\mathcal{O}(\Delta x_i^2\Delta x_j^2) & \text{if } i\neq j\end{cases} \tag{C.27}$$

Here $\xi_i=\frac{2\pi \mathrm{j} p_i}{2^{N^{qb}}}$ denotes the classical frequency. Furthermore, the following differential operators in Fourier space are obtained using the modified frequencies derived from the 63-point finite difference scheme. According to Eqs. (C.32) and (C.33), the difference between the C/EMCurl and C/EMCurl-Star models corresponds to different differential operators employed, which lead to different modified frequencies in Fourier space.

$$\widehat{\left(\nabla \underset{\sim}{A}\right)}_{ijl}=A_{ij}\mathfrak{f}_l^{1,m}=\widehat{\mathrm{Grad}}\left(\underset{\sim}{\hat{A}}\right) \tag{C.28}$$

$$\widehat{\left(\nabla\times \underset{\sim}{A}\right)}_{ij}=\epsilon_{jml}\mathfrak{f}_l^{1,m}\hat{A}_{im}=\widehat{\mathrm{Curl}}\left(\underset{\sim}{\hat{A}}\right) \tag{C.29}$$

$$\widehat{\left(\nabla\otimes\nabla\cdot\left(\underset{\sim}{A}\right)\right)}_{ij}=\hat{A}_{im}\mathfrak{f}_{mj}^{2,m}=\widehat{\mathrm{Grad\text{-}Div}}\left(\underset{\sim}{\hat{A}}\right) \tag{C.30}$$

$$\widehat{\left(\Delta\left(\underset{\sim}{A}\right)\right)}_{ii}=\hat{A}_{ii}\mathfrak{f}_{ii}^{2,m}=\widehat{\mathrm{Lap}}\left(\underset{\sim}{\hat{A}}\right) \tag{C.31}$$

$$\widehat{\left(\nabla\times\nabla\times \underset{\sim}{A}\right)}_{ij}=\epsilon_{jms}\mathfrak{f}_s^{1,m}\epsilon_{mlr}\mathfrak{f}_r^{1,m}\hat{A}_{il}=\widehat{\mathrm{DCurl\text{-}S}}\left(\underset{\sim}{\hat{A}}\right) \tag{C.32}$$

$$\widehat{\left(\nabla\times\nabla\times \underset{\sim}{A}\right)}_{ij}=\widehat{\left(\nabla\otimes\nabla\cdot\left(\underset{\sim}{A}\right)\right)}_{ij}-\widehat{\left(\Delta\left(\underset{\sim}{A}\right)\right)}_{ii}=\widehat{\mathrm{Grad\text{-}Div}}\left(\underset{\sim}{\hat{A}}\right)-\widehat{\mathrm{Lap}}\left(\underset{\sim}{\hat{A}}\right)=\widehat{\mathrm{DCurl\text{-}J}}\left(\underset{\sim}{\hat{A}}\right) \tag{C.33}$$

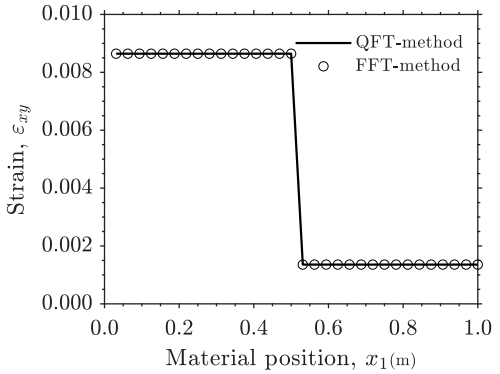

Fig. D.1. Validation of the QFT-method against the FFT-method in a two-phase linear elastic laminate.

Appendix D. Validation

The validation of the proposed QFT-method is presented in this appendix. To this end, several representative material behaviors are considered, including linear elastic behavior, linear plastic behavior, and nonlinear plastic behavior, in order to assess the accuracy and robustness of the method across different constitutive equations.

D.1. Linear elastic behavior

The first benchmark problem originally simulated using the FFT-method in solid mechanics corresponds to the two-phase laminate introduced in Moulinec and Suquet (1998), where the numerical solution was validated against an analytical reference. The laminate consists of two layers with equal volume fractions, each exhibiting linear isotropic elastic behavior characterized by a Young's modulus and Poisson's ratio. Under the imposed shear loading, each layer develops a uniform strain field, which makes this configuration particularly suitable for verification. The elastic properties of the first layer are taken as $E^1 = 68.9$ (GPa) and $\nu^1 = 0.35$, whereas the second layer is defined by $E^2 = 400$ (GPa) and $\nu^2 = 0.23$. The laminate geometry is discretized on a 32×32 pixel grid and subjected to shear loading in the x_1–x_2 plane.

Fig. D.1 presents the results obtained with the proposed QFT-method, which show a one-to-one correspondence with the reference FFT-method results reported in Moulinec and Suquet (1998).

D.2. Linear plastic behavior

In this appendix, the quantum algorithm proposed for the CMSlip model is validated against analytical solutions for several representative constitutive responses, using the linear relation $\tau^{\alpha}_{\mathrm{cr}} = \tau^{\alpha}_{0} + H^{\alpha}\gamma^{\alpha}_{cum}$ as proposed in Lame Jouybari et al. (2024). Accordingly, three material behaviors are considered: linear hardening ($H = 10$ MPa), perfect plasticity ($H = 0$ MPa), and linear softening ($H = -10$ MPa). The benchmark problem consists of a single crystal with dimensions $1\ \mathrm{mm} \times 1\ \mathrm{mm}$, discretized on a 64×64 voxel grid and subjected to shear loading with an imposed macroscopic shear amplitude of $\overline{\gamma} = 0.01$. Additional details of the analytical solution procedure and boundary conditions are provided in Lame Jouybari et al. (2024).

Fig. D.2 compares the results obtained with the QFT-method to the corresponding analytical solutions of the CMSlip model for the different material behaviors. For linear hardening, the shear strain field remains relatively smooth, whereas for perfect plasticity the deformation localizes more sharply. Under linear softening, the shear strain becomes highly localized within a finite-width region, leading to the formation of a shear band. In all cases, an excellent level of agreement is obtained between the QFT-method results and the analytical solutions.

D.3. Nonlinear plastic behavior

In this appendix, the proposed QFT-method for the EMSlip model is examined by comparison with the analytical solution reported in Lame Jouybari et al. (2025). To this end, the nonlinear softening behavior defined by Eq. (8) is considered for a single crystal with dimensions of $1\ \mathrm{mm} \times 1\ \mathrm{mm}$ subjected to simple shear loading with an imposed macroscopic shear amplitude of $\overline{\gamma} = 0.001$. The nonlinear softening response is specified through a maximum softening magnitude of $\triangle\tau^{\alpha} = 15$ MPa and a softening rate parameter of $\gamma_0 = 0.01$. In addition, the intrinsic length scale is prescribed as $\Lambda_0 = 0.25$ mm.

Fig. D.3 compares the shear strain profiles obtained from the QFT-method with the analytical solution at three representative stages during the loading up to $\overline{\gamma} = 0.001$. It is observed that the shear band width remains equal to the prescribed length scale and, throughout deformation, does not propagate toward the crystal boundary, consistent with the behavior reported for enhanced SGCP theory in Lame Jouybari et al. (2025). Overall, an excellent level of agreement is obtained between the analytical and numerical results.

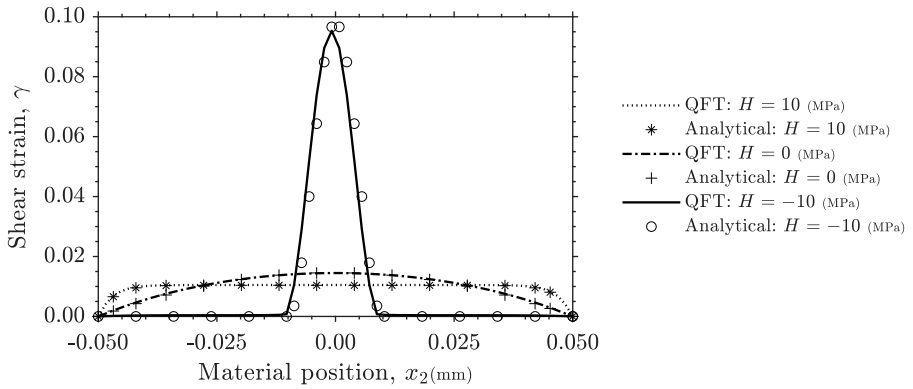

Fig. D.2. Validation of QFT-method against analytical solutions for different material behaviors by the fixed nonlocal parameter $A = 10^{-2}$ (N) within the CMSlip-SGCP model.

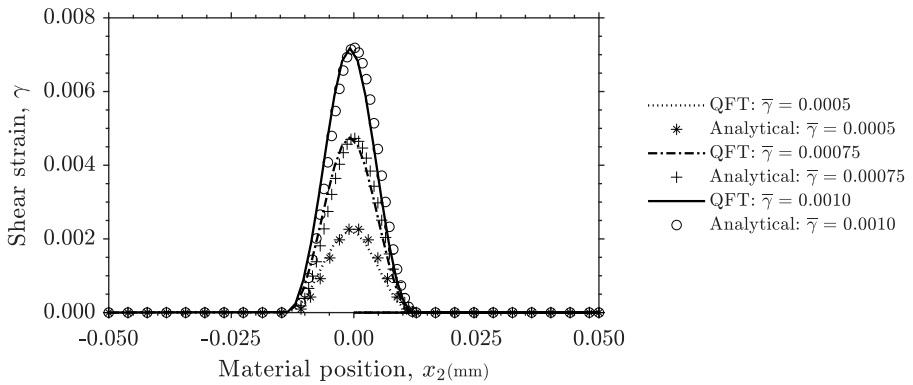

Fig. D.3. Validation of QFT-method against analytical solutions in different steps of loading, $\overline{\gamma}$, by the fixed length scale $\Lambda_0 = 0.25$ (mm) within the EMSlip model.

Appendix E. Two-dimensional single crystal under tensile loading

A periodic single crystal with unit-cell dimensions of $1\,\mathrm{mm} \times 1\,\mathrm{mm}$ is subjected to uniaxial tension in the y-direction. The applied loading corresponds to a macroscopic displacement-gradient component of $\overline{\nabla u}_{yy} = 0.01$, imposed at a constant strain-rate of $10^{-6}\,\mathrm{s}^{-1}$; all other Cauchy-stress components are held at zero. A single slip system ($N_\alpha = 1$) is oriented 45° counter-clockwise from the loading axis. To promote strain localization, an imperfection is introduced at the central voxel $(N_1/2, N_2/2)$ by reducing the initial critical resolved shear stress to $\tau_0^{\mathrm{defect}} = 0.99\,\tau_0$. Both the CCP framework and the SGCP models are considered here.

Material parameters. The crystal is assumed isotropic in elasticity with $E = 100\,\mathrm{GPa}$ and $\nu = 0.3$. Viscoplastic flow, for example in the CCP framework corresponds to the Eq. (7), is described by the Norton flow coefficient $K = 10\,\mathrm{MPa\,s}^{-n}$ and Norton flow exponent $n = 15$, representative of irradiated austenitic SS (Hure et al., 2016). Irradiation-induced softening is captured through an initial critical resolved shear stress $\tau_0 = 100\,\mathrm{MPa}$, a softening magnitude $\Delta\tau = 20\,\mathrm{MPa}$, and a softening rate $\gamma_0 = 0.05$. The spatial resolution — 64 × 64 voxels — is considered. For the ESGCP models the internal length scale is set to $\Lambda_0 = 0.1\,\mathrm{mm}$; the equivalent parameter in the classical SGCP formulations is chosen as $A = 0.101\ N$ (cf. Eq. (29)).

Classical crystal plasticity framework. Fig. E.1 displays, respectively, the shear strain γ and lattice-rotation field θ predicted by the CCP framework. Two perpendicular localized bands emerge (equivalent ratio between slip and kink bands, or one slip band and one kink band in lattice): one exhibits intense shear strain only (slip band) while the other combines shear strain with large rotation (kink band). Both bands collapse to a single voxel width, indicating mesh-dependence and loss of regularization under softening behavior.

Classical MicroSlip SGCP model. Fig. E.2 (a,b) shows that the CMSlip model keeps equivalent ratio between slip and kink bands, regularizes both slip and kink bands, and producing finite-width zones that are insensitive to voxel size.

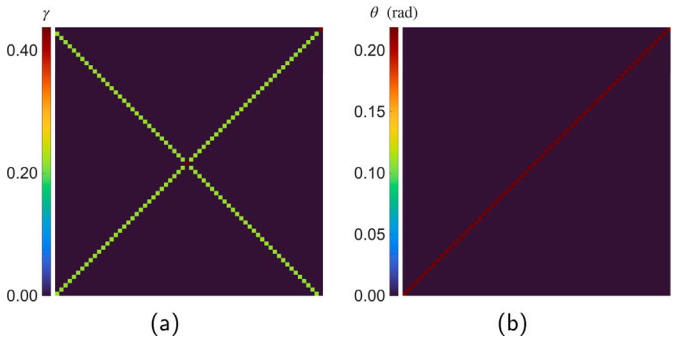

Fig. E.1. Distributions of shear strain and rotation field in a two-dimensional single crystal at final loading, $\nabla \underline{u}_{yy} = 0.01$, by the CCP framework.

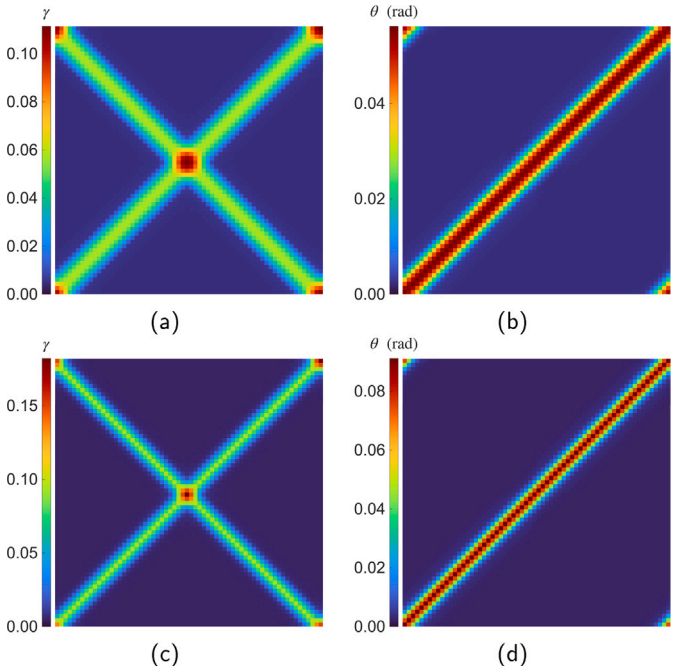

Fig. E.2. Distributions of shear strain and rotation field in a two-dimensional single crystal at final loading, $\nabla \underline{u}_{yy} = 0.01$, by the (a,b) CMSlip model, $A = 0.101$ N, and (c,d) EMSlip model, $\Lambda_0 = 0.1$ mm.

Classical MicroCurl-SGCP model. Results in Fig. E.3 (a,b) reveals that the CMCurl model suppresses the kink band while leaving the slip band slightly influenced, thereby breaking the slip–kink equivalence.

Enhanced MicroSlip-SGCP model. Figs. E.2 (c,d) demonstrates that the EMSlip model keeps equivalent ratio between slip and kink bands, and stabilizes both bands with a fixed width equal to the prescribed length scale $\Lambda_0 = 0.1$ mm. The solutions are mesh-independent and do not exhibit the fictitious band growth observed in the classical model, while the peak amplitudes are higher due to stronger localization.

Enhanced MicroCurl-SGCP model. The cumulative shear strain field predicted by the EMCurl model (Fig. E.3 (c,d)) again shows suppression of kink-band rotation and persistence of unstable and slightly-regularized slip localization. Thus, the enhanced formulation inherits the kink band removing of the CMCurl model, but with higher localization amplitude in slip band.

Classical and enhanced MicroCurl-Star-SGCP models. Results in Fig. E.4 (a,b) reveals that the CMCurl-Star model suppresses the kink band while leaving the slip band completely uninfluenced. Furthermore, Fig. E.4 (c,d) shows the results from the EMCurl-Star model which is similar to the CMCurl-Star model due to the slip system of the crystalline lattice. The differences between the C/EMCurl-Star models with respect to the C/EMCurl models is directly related to proposed finite difference method and different modified frequencies, Eqs. (C.32) and (C.33), in evaluating the micro-stress tensor and accordingly back-stress within the shear flow rule.

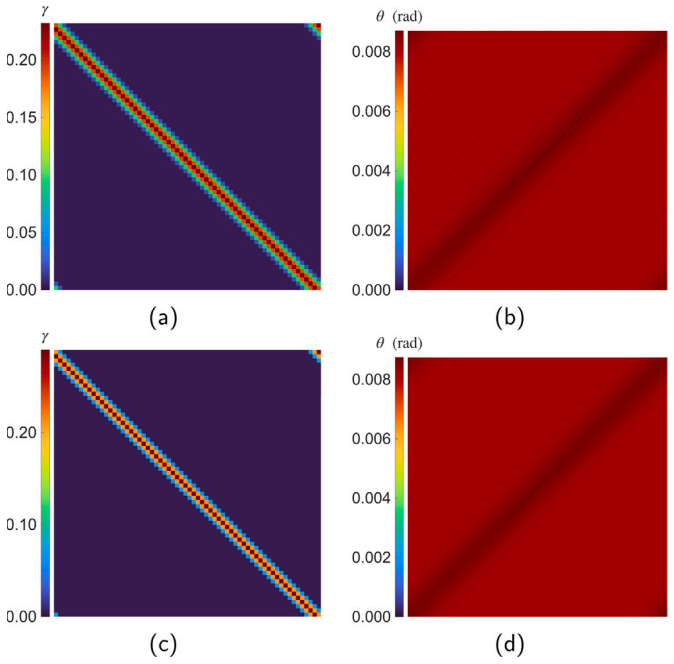

Fig. E.3. Distributions of shear strain and rotation field in a two-dimensional single crystal at final loading, $\nabla \underline{u}_{yy} = 0.01$, by the (a,b) CMCurl model, $A = 0.101$ N, and (c,d) EMCurl model, $\Lambda_0 = 0.1$ mm.

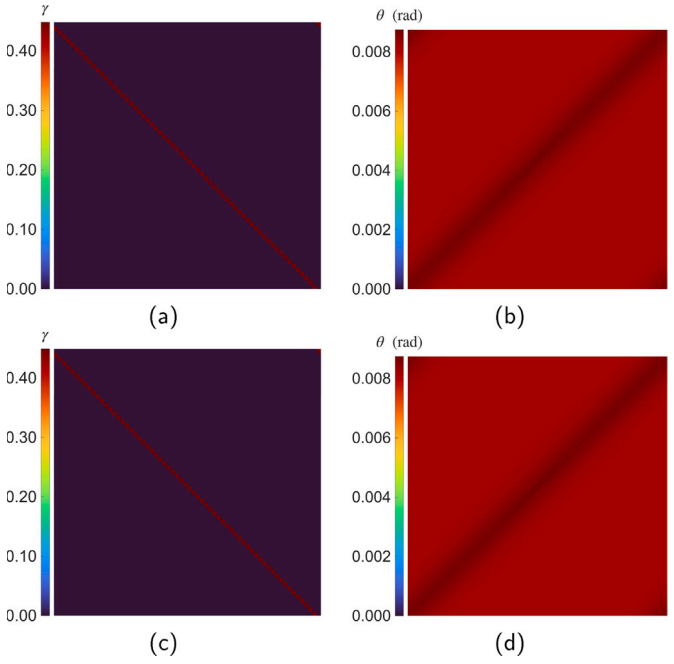

Fig. E.4. Distributions of shear strain and rotation field in a two-dimensional single crystal at final loading, $\nabla \underline{u}_{yy} = 0.01$, by the (a,b) CMCurl-Star model, $A = 0.101$ N, and (c,d) EMCurl-Star model, $\Lambda_0 = 0.1$ mm.

Data availability

Data will be made available on request.

References

Abatour, M., Forest, S., 2024. Strain gradient plasticity based on saturating variables. Eur. J. Mech. A Solids 104, 105016. http://dx.doi.org/10.1016/j.euromechsol.2023.105016.

Agius, D., Kareer, A., Al Mamun, A., Truman, C., Collins, D.M., Mostafavi, M., Knowles, D., 2022. A crystal plasticity model that accounts for grain size effects and slip system interactions on the deformation of austenitic stainless steels. Int. J. Plast. 152, 103249. http://dx.doi.org/10.1016/j.ijplas.2022.103249.

Ahmadikia, B., Kumar, M.A., Beyerlein, I.J., 2021. Effect of neighboring grain orientation on strain localization in slip bands in HCP materials. Int. J. Plast. 144, 103026. http://dx.doi.org/10.1016/j.ijplas.2021.103026.

Arora, A., Ward, B.M., Oskay, C., 2025. An implementation of the finite element method in hybrid classical/quantum computers. Finite Elem. Anal. Des. 248, 104354. http://dx.doi.org/10.1016/j.finel.2025.104354.

Brepols, T., Wulfinghoff, S., Reese, S., 2020. A gradient-extended two-surface damage-plasticity model for large deformations. Int. J. Plast. 129, 102635. http://dx.doi.org/10.1016/j.ijplas.2019.11.014.

Brisard, S., Dormieux, L., 2010. FFT-based methods for the mechanics of composites: A general variational framework. Comput. Mater. Sci. 49 (3), 663–671. http://dx.doi.org/10.1016/j.commatsci.2010.06.009.

Cao, L., Lu, R., Dou, Z., Zheng, M., Han, X., Hao, Y., Zhang, L., Zhang, J., Liu, B., Li, X., 2025. Understanding the influence of high-strength submicron precipitate on the fracture performance of additively-manufactured aluminum alloy. Int. J. Plast. 188, 104306. http://dx.doi.org/10.1016/j.ijplas.2025.104306.

Cao, Y., Papageorgiou, A., Petras, I., Traub, J., Kais, S., 2013. Quantum algorithm and circuit design solving the Poisson equation. New J. Phys. 15 (1), 013021. http://dx.doi.org/10.1088/1367-2630/15/1/013021.

Clayton, J.D., 2024. Analysis of shear localization in viscoplastic solids with pressure-sensitive structural transformations. J. Mech. Phys. Solids 193, 105880. http://dx.doi.org/10.1016/j.jmps.2024.105880.

Clayton, J., Lloyd, J., Casem, D., 2023. Simulation and dimensional analysis of instrumented dynamic spherical indentation of ductile metals. Int. J. Mech. Sci. 251, 108333. http://dx.doi.org/10.1016/j.ijmecsci.2023.108333.

Cooley, J.W., Tukey, J.W., 1965. An algorithm for the machine calculation of complex Fourier series. Math. Comp. 19 (90), 297–301. http://dx.doi.org/10.2307/2003354.

Coppersmith, D., 2002. An approximate Fourier transform useful in quantum factoring. 0201067. http://dx.doi.org/10.48550/arXiv.quant-ph/0201067, ArXiv Preprint Quant-Ph.

Dadhich, R., Alankar, A., 2022. A modular spectral solver for crystal plasticity. Int. J. Plast. 156, 103328. http://dx.doi.org/10.1016/j.ijplas.2022.103328.

Dahlberg, C., Boasen, M., 2019. Evolution of the length scale in strain gradient plasticity. Int. J. Plast. 112, 220–241. http://dx.doi.org/10.1016/j.ijplas.2018.08.016.

Ding, Y., Zhu, C., Ortiz, M., Matsunaga, H., Olden, V., Yu, H., He, J., Zhang, Z., 2024. Data-driven micromorphic mechanics for materials with strain localization. Int. J. Mech. Sci. 110816. http://dx.doi.org/10.1016/j.cma.2024.117180.

El Shawish, S., Cizelj, L., Tanguy, B., Han, X., Hure, J., 2016. Macroscopic validation of the micromechanical model for neutron-irradiated stainless steel. In: Proceedings of the 25th International Conference Nuclear Energy for New Europe PortoroŽ, Slovenia.

Feynman, R., 1982. Simulating physics with computers. Internat. J. Theoret. Phys. 21, 467–488.

Grover, L.K., 1997. Super classical search algorithm to find an element in unsorted array. Phys. Rev. Lett. 78, 325–328.

Gurtin, M.E., 2002. A gradient theory of single-crystal viscoplasticity that accounts for geometrically necessary dislocations. J. Mech. Phys. Solids 50 (1), 5–32. http://dx.doi.org/10.1016/S0022-5096(01)00104-1.

Harrow, A.W., Hassidim, A., Lloyd, S., 2009. Quantum algorithm for linear systems of equations. Phys. Rev. Lett. 103 (15), 150502. http://dx.doi.org/10.48550/arXiv.0811.3171.

Hesterberg, J., Jiao, Z., Was, G.S., 2019. Effects of post-irradiation annealing on the IASCC susceptibility of neutron-irradiated 304l stainless steel. J. Nucl. Mater. 526, 151755. http://dx.doi.org/10.1016/j.jnucmat.2019.151755.

Hure, J., El Shawish, S., Cizelj, L., Tanguy, B., 2016. Intergranular stress distributions in polycrystalline aggregates of irradiated stainless steel. J. Nucl. Mater. 476, 231–242. http://dx.doi.org/10.1016/j.jnucmat.2016.04.017.

Lame Jouybari, A., 2026. Computational Evolution of Strain Localization through Grain Boundaries in Irradiated Polycrystals. Doctoral dissertation, Univerza v Ljubljani, Fakulteta za matematiko in fiziko.

Lame Jouybari, A., El Shawish, S., Cizelj, L., 2023. Crystal plasticity model of austenitic stainless steels subjected to hydrogen concentration and neutron irradiation. In: Proc. Int. Conf. Nucl. Eng.. ICONE, 30, p. 1729. http://dx.doi.org/10.1299/jsmeicone.2023.30.1729.

Lame Jouybari, A., El Shawish, S., Cizelj, L., 2024. Fast Fourier transform approach to strain gradient crystal plasticity: Regularization of strain localization and size effect. Int. J. Plast. 183, 104153. http://dx.doi.org/10.1016/j.ijplas.2024.104153.

Lame Jouybari, A., El Shawish, S., Cizelj, L., 2025. Enhanced strain gradient crystal plasticity theory: Evolution of the length scale during deformation. Int. J. Plast. 104351. http://dx.doi.org/10.1016/j.ijplas.2025.104351.

Li, C., Xu, Z., Wang, J., Peng, L., 2025. Multiscale analysis and modeling of nano-coating fracture induced by inhomogeneous plastic deformation of polycrystalline metallic substrate. Int. J. Plast. 104396. http://dx.doi.org/10.1016/j.ijplas.2025.104396.

Lindroos, M., Pinomaa, T., Ammar, K., Laukkanen, A., Provatas, N., Forest, S., 2022a. Dislocation density in cellular rapid solidification using phase field modeling and crystal plasticity. Int. J. Plast. 148, 103139. http://dx.doi.org/10.1016/j.ijplas.2021.103139.

Lindroos, M., Scherer, J., Forest, S., Laukkanen, A., Andersson, T., Vaara, J., Mäntylä, A., Frondelius, T., 2022b. Micromorphic crystal plasticity approach to damage regularization and size effects in martensitic steels. Int. J. Plast. 151, 103187. http://dx.doi.org/10.1016/j.ijplas.2021.103187.

Lippmann, B.A., Schwinger, J., 1950. Variational principles for scattering processes. Phys. Rev. 79 (3), 469. http://dx.doi.org/10.1103/PhysRev.79.469.

Liu, B., Ortiz, M., Cirak, F., 2024. Towards quantum computational mechanics. Comput. Methods Appl. Mech. Engrg. 432, 117403. http://dx.doi.org/10.1016/j.cma.2024.117403.

Low, G.H., Chuang, I.L., 2019. Hamiltonian simulation by qubitization. Quantum 3, 163. http://dx.doi.org/10.48550/arXiv.1610.06546.

Lubasch, M., Kikuchi, Y., Wright, L., Keever, C.M., 2025. Quantum circuits for partial differential equations in Fourier space, ArXiv Preprint ArXiv:2505, 16895, http://dx.doi.org/10.48550/arXiv.2505.16895.

Lucarini, S., Segurado, J., 2019. DBFFT: A displacement based FFT approach for non-linear homogenization of the mechanical behavior. Internat. J. Engrg. Sci. 144, 103131. http://dx.doi.org/10.1016/j.ijengsci.2019.103131.

Manin, Y., 1980. Computable and Uncomputable, 128 Moscow.

Marano, A., Gélébart, L., Forest, S., 2021. FFT-based simulations of slip and kink bands formation in 3D polycrystals: Influence of strain gradient crystal plasticity. J. Mech. Phys. Solids 149, 104295. http://dx.doi.org/10.1016/j.jmps.2021.104295.

Matlab, R., 2025. The MathWorks, inc., natick, massachusetts, United States, release, s. t. 2025b. https://www.mathworks.com/products/new_products/latest_features.html.

McClean, J.R., Romero, J., Babbush, R., Aspuru-Guzik, A., 2016. The theory of variational hybrid quantum-classical algorithms. New J. Phys. 18 (2), 023023. http://dx.doi.org/10.48550/arXiv.1509.04279.

Miyamoto, K., Kubo, K., 2021. Pricing multi-asset derivatives by finite-difference method on a quantum computer. IEEE Trans. Quantum Eng. 3, 1–25. http://dx.doi.org/10.48550/arXiv.2109.12896.

Montanaro, A., Pallister, S., 2016. Quantum algorithms and the finite element method. Phys. Rev. A 93 (3), 032324. http://dx.doi.org/10.48550/arXiv.1512.05903.
Mottonen, M., Vartiainen, J.J., Bergholm, V., Salomaa, M.M., 2004. Transformation of quantum states using uniformly controlled rotations. 0407010. http://dx.doi.org/10.48550/arXiv.quant-ph/0407010, ArXiv Preprint Quant-Ph.
Moulinec, H., Suquet, P., 1998. A numerical method for computing the overall response of nonlinear composites with complex microstructure. Comput. Methods Appl. Mech. Engrg. 157 (1-2), 69–94. http://dx.doi.org/10.1016/S0045-7825(97)00218-1.
Nielsen, M.A., Chuang, I.L., 2010. Quantum Computation and Quantum Information, 128 ed. Cambridge University Press.
Nye, J.F., 1953. Some geometrical relations in dislocated crystals. Acta Metall. 1 (2), 153–162. http://dx.doi.org/10.1016/0001-6160(53)90054-6.
Pai, N., Prakash, A., Samajdar, I., Patra, A., 2022. Study of grain boundary orientation gradients through combined experiments and strain gradient crystal plasticity modeling. Int. J. Plast. 156, 103360. http://dx.doi.org/10.1016/j.ijplas.2022.103360.
Pai, N., Samajdar, I., Patra, A., 2025. Study of orientation-dependent residual strains during tensile and cyclic deformation of an austenitic stainless steel. Int. J. Plast. 185, 104228. http://dx.doi.org/10.1016/j.ijplas.2024.104228.
Petryk, H., Stupkiewicz, S., 2016. A minimal gradient-enhancement of the classical continuum theory of crystal plasticity. Part I: the hardening law. Arch. Mech. 68, 459–485. http://dx.doi.org/10.24423/aom.2539, https://am.ippt.pan.pl/index.php/am/article/view/v68p459.
Quey, R., Dawson, P.R., Barbe, F., 2011. Large-scale 3D random polycrystals for the finite element method: Generation, meshing and remeshing. Comput. Methods Appl. Mech. Engrg. 200 (17-20), 1729–1745. http://dx.doi.org/10.1016/j.cma.2011.01.002.
Raisuddin, O.M., De, S., 2024. qRLS: quantum relaxation for linear systems in finite element analysis. Eng. Comput. 40 (5), 3273–3293. http://dx.doi.org/10.48550/arXiv.2308.01377.
Ren, S.C., Morgeneyer, T.F., Mazière, M., Forest, S., Rousselier, G., 2021. Effect of lüders and portevin–le chatelier localization bands on plasticity and fracture of notched steel specimens studied by DIC and fe simulations. Int. J. Plast. 136, 102880. http://dx.doi.org/10.1016/j.ijplas.2020.102880.
Roy, V., Khan, I.A., Patra, A., 2025. Crystal plasticity modeling of hardening and creep in ferritic-martensitic alloys under thermal and irradiation environments. Int. J. Plast. 104513. http://dx.doi.org/10.1016/j.ijplas.2025.104513.
Ryś, M., Stupkiewicz, S., Petryk, H., 2022. Micropolar regularization of crystal plasticity with the gradient-enhanced incremental hardening law. Int. J. Plast. 156, 103355. http://dx.doi.org/10.1016/j.ijplas.2022.103355.
Scherer, J.M., Besson, J., Forest, S., Hure, J., Tanguy, B., 2019. Strain gradient crystal plasticity with evolving length scale: Application to voided irradiated materials. Eur. J. Mech. A Solids 77, 103768. http://dx.doi.org/10.1016/j.euromechsol.2019.04.003.
Shor, P.W., 1997. Polynomial-time algorithms for prime factorization and discrete logarithms on a quantum computer. SIAM J. Comput. 26 (5), 1484–1509. http://dx.doi.org/10.1137/S0097539795293172.
Sudhalkar, B.R., Barik, R.K., Patra, A., Kapoor, K., Kapoor, R., Agrawal, A., Samajdar, I., 2025. Growth selection of deformation twins in hexagonal titanium. Int. J. Plast. 104574. http://dx.doi.org/10.1016/j.ijplas.2025.104574.
Sukulthanasorn, N., Xiao, J., Wagatsuma, K., Nomura, R., Moriguchi, S., Terada, K., 2025. A novel design update framework for topology optimization with quantum annealing: Application to truss and continuum structures. Comput. Methods Appl. Mech. Engrg. 437, 117746. http://dx.doi.org/10.1016/j.cma.2025.117746.
Sumigawa, T., Kawakatsu, N., Tobise, A., Sugisaka, K., Takahashi, Y., Arai, S., Abe, M., Shima, H., Umeno, Y., 2024. Dislocation structures in micron-sized Ni single crystals produced via tension–compression cyclic loading. Acta Mater. 277, 120208. http://dx.doi.org/10.1016/j.actamat.2024.120208.
Sutor, R.S., 2024. Dancing with Qubits: From Qubits to Algorithms, Embark on the Quantum Computing Journey Shaping Our Future. Packt Publishing Ltd.
Tang, X., Wang, Z., Wang, X., Deng, L., Zhang, M., Gong, P., Jin, J., Fu, M.W., 2023. Unraveling size-affected plastic heterogeneity and asymmetry during micro-scaled deformation of CP-Ti by non-local crystal plasticity modeling. Int. J. Plast. 170, 103733. http://dx.doi.org/10.1016/j.ijplas.2023.103733.
Thomas, R., Lunt, D., Atkinson, M., da Fonseca, J., Preuss, M., Barton, F., O'Hanlon, J., Frankel, P., 2019. Characterisation of irradiation enhanced strain localisation in a zirconium alloy. Materialia 5, 100248. http://dx.doi.org/10.1016/j.mtla.2019.100248.
Tosti Balducci, G., Chen, B., Möller, M., Gerritsma, M., De Breuker, R., 2022. Review and perspectives in quantum computing for partial differential equations in structural mechanics. Front. Mech. Eng. 8, 914241. http://dx.doi.org/10.3389/fmech.2022.914241.
Toursangsaraki, M., Tang, R., Du, D., Zhang, X., Dong, A., Leen, S.B., Sun, B., 2025. Non local crystal plasticity and in-situ EBSD of deformation anisotropy in LPBF-ed inconel 718. Int. J. Mech. Sci. 111136. http://dx.doi.org/10.1016/j.ijmecsci.2025.111136.
Ulloa, J., Stainier, L., Ortiz, M., Andrade, J.E., 2024. Data-driven micromorphic mechanics for materials with strain localization. Comput. Methods Appl. Mech. Engrg. 429, 117180. http://dx.doi.org/10.1016/j.cma.2024.117180.
Wang, J., Peter, N.J., Heilmaier, M., Schwaiger, R., 2025. A micromechanical investigation of plasticity in ordered NbMoCrTiAl and disordered TaNbHfZrTi refractory compositionally complex alloys at room temperature. Int. J. Plast. 104593. http://dx.doi.org/10.1016/j.ijplas.2025.104593.
White, R.D., Ahmadikia, B., Beyerlein, I.J., 2025. Grain size effects on slip band development. Int. J. Solids Struct. 113589. http://dx.doi.org/10.1016/j.ijsolstr.2025.113589.
Wicht, D., Schneider, M., Böhlke, T., 2021. Anderson-accelerated polarization schemes for fast Fourier transform-based computational homogenization. Internat. J. Numer. Methods Engrg. 122 (9), 2287–2311. http://dx.doi.org/10.1002/nme.6622.
Williams, C.L., Hornbuckle, B.C., Mallick, D.D., Parker, T.C., Clayton, J.D., Wilkerson, J.W., 2025. Strength-ductility synergy of a high chromium martensitic steel with a unique microstructure under dynamic extremes. Acta Mater. 121368. http://dx.doi.org/10.1016/j.actamat.2025.121368.
Wulfinghoff, S., 2025. Homogenization in hyperelasticity using empirically corrected cluster Cubature (E3C) hyper-reduction. Comput. Methods Appl. Mech. Engrg. 444, 118137. http://dx.doi.org/10.1016/j.cma.2025.118137.
Wulfinghoff, S., 2026. Computational crystal plasticity homogenization using empirically corrected cluster cubature (E3C) hyper-reduction. Comput. Methods Appl. Mech. Engrg. 452, 118681. http://dx.doi.org/10.1016/j.cma.2025.118681.
Wulfinghoff, S., Böhlke, T., 2012. Equivalent plastic strain gradient enhancement of single crystal plasticity: theory and numerics. Proc. R. Soc. A Math. Phys. Eng. Sci. 468 (2145), 2682–2703. http://dx.doi.org/10.1098/rspa.2012.0073.
Yan, Y., Sumigawa, T., Wang, X., Chen, W., Xuan, F., Kitamura, T., 2020. Fatigue curve of microscale single-crystal copper: An in situ sem tension-compression study. Int. J. Mech. Sci. 171, 105361. http://dx.doi.org/10.1016/j.ijmecsci.2019.105361.
You, X., Yang, J., Dan, C., Shi, Q., Zhong, S., Wang, H., Chen, Z., 2023. Statistical analysis of slip transfer in al alloy based on in-situ tensile test and high-throughput computing method. Int. J. Plast. 166, 103649. http://dx.doi.org/10.1016/j.ijplas.2023.103649.
Zbib, H., Aifantis, E., 1998. On the structure and width of shear bands. Scr. Met. 22, 703–708. http://dx.doi.org/10.1016/S0036-9748(88)80186-8.
Zeman, J., Vondřejc, J., Novák, J., Marek, I., 2010. Accelerating a FFT-based solver for numerical homogenization of periodic media by conjugate gradients. J. Comput. Phys. 229 (21), 8065–8071. http://dx.doi.org/10.1016/j.jcp.2010.07.010.
Zhang, X., Sumigawa, T., 2025. A cross-scale stress gradient plasticity theory for length-scale effects on hardening behaviors of microbeam bending. Int. J. Plast. 104494. http://dx.doi.org/10.1016/j.ijplas.2025.104494.